Spring 2012

Design of *In Vivo* Assays for Study of Transport, Biocompatibility and Toxicity of Nanoparticles

Kerry Jean Lee
Old Dominion University

DESIGN OF *IN VIVO* ASSAYS FOR STUDY OF TRANSPORT, BIOCOMPATIBILITY AND TOXICITY OF NANOPARTICLES

by

Kerry Jean Lee
M.S. May 2005, Old Dominion University – Norfolk, VA

A Dissertation Submitted to the Faculty of
Old Dominion University in Partial Fulfillment of the
Requirements for the Degree of

DOCTOR OF PHILOSOPHY

BIOMEDICAL SCIENCES

OLD DOMINION UNIVERSITY
May 2012

Approved by:

Xiao-Hong Nancy Xu (Director)

Christopher Osgood (Member)

Kenneth Brown (Member)

Lesley H. Greene (Member)

ABSTRACT

DESIGN OF *IN VIVO* ASSAYS FOR STUDY OF TRANSPORT, BIOCOMPATIBLITY AND TOXICITY OF NANOPARTICLES

Kerry Jean Lee
Old Dominion University, 2012
Director: Dr. Xiao-Hong Nancy Xu

This dissertation focuses on the design of new *in vivo* assays for study of transport, biocompatibility and toxicity of nanoparticles (NPs) in zebrafish embryos. We synthesized and purified spherical silver (Ag) NPs with diameters, ranging from 12 to 95 nm, that are stable (non-aggregated) in egg-water media. We developed new imaging approaches to characterize the sizes of single Ag NPs in zebrafish embryos at nanometer resolution by measuring their size-dependent plasmonic spectra and scattering intensity using dark-field optical microscopy and spectroscopy (DFOMS). We used single Ag NPs because they exhibit the high quantum yield (QY) of Rayleigh scattering and resist photobleaching and blinking, allowing to be continuously monitored *in vivo* for any desired amount of time. These unique optical properties make them better than traditional imaging probes, such as fluorescence probes (e.g., fluorophores and semiconductor quantum dots), that are currently used for *in vivo* imaging and widely used in life science. With no need of fluorescence excitation, Ag NPs can be used to monitor transport in a living *in vivo* system and effectively avoids auto-fluorescence of the living organism, allowing us to monitor it in real-time in the developing embryo.

Using different properties of Ag NPs, size-dependent optical properties and charge-dependent surface properties, we studied transport and toxicity in living embryos in real-time for better understanding of biocompatibility of NPs in a living *in vivo* model system. Using Ag NPs, we continuously imaged nano-environments of developing zebrafish embryos for hours and discovered their transport patterns through the chorion and into the chorion space of the different stages of embryos. We demonstrated that the different types of Ag NPs caused a wide variety of deformities and caused an increase in death, and both in a concentration dependent manner in living zebrafish embryos. This determined that zebrafish embryos are a powerful *in vivo* assay to use to study the transport, biocompatibility and toxicity of nanomaterials.

This dissertation is dedicated to my parents, Mr. Gregory Wayne White and Mrs. Alaine Marie White for their unrelenting love, support, and financial assistance, which made all of this possible and to my grandmother, Dolores Jean Riegle, who is proud of all my achievements.

ACKNOWLEDGMENTS

Most importantly, I would like to thank my advisor and mentor, Dr. X. Nancy Xu for her continuous assistance and support throughout my Ph.D. study at Old Dominion University. Without her dedication to me, this dissertation would not be possible. I appreciate her for allowing me to learn a variety of scientific techniques and multiple disciplines of the sciences. I have learned from her to love scientific research. I am grateful for her inspiration and perseverance for me to present our work at national and international meetings and conferences. I have built my confidence in speaking with my colleagues and further appreciated my research work because of these experiences.

I would like to extend thanks to the members of my dissertation committee, Drs. Christopher J. Osgood, Kenneth Brown, and Lesley H. Greene for their helpful knowledge and support. I thank my fellow lab group members, especially Lauren M. Browning, Prakash D. Nallathamby, and Tao Huang, for their valuable assistance and support. Without their collaboration, I would not be able to accomplish such an immense volume of work.

I thank the National Science Foundation, especially (NSF/NIRT/GRAS: CCBET 0541661), (NIRT: BES 0507036) and NIH (R01 GM076440) for their financial support of this work and my graduate education.

The work was carried out at the Department of Chemistry and Biochemistry, Old Dominion University, Norfolk, VA, and supported by National Science Foundation (NIRT: BES 0507036) and NIH (R01 GM076440).

NOMENCLATURE

ε	Extinction coefficient
µg/mL	Microgram per milliliter
µm	Micrometer
η	Viscosity
ζ	Zeta potential in mV
Ag	Silver
$AgClO_4$	Silver perchlorate
Ag-CALNNE	Silver nanoparticles functionalized with CALNNE peptide yielding a negative charge
Ag-CALNNK	Silver nanoparticles functionalized with CALNNK peptide yielding a positive charge
Ag-CALNNS	Silver nanoparticles functionalized with CALNNS peptide yielding a near neutral charge
$AgNO_3$	Silver nitrate
cm	centimeter
C	Concentration
CASI	Color as a size index
CCD	Charge coupled device used for imaging nanoparticles with high sensitivity, temporal resolution and spatial resolution
Cd^{2+}	Cadmium
CL	Chorion Layer
CPCs	Chorion Pore Channels
CS	Chorion space

D	Diffusion coefficient
DCA	Dichloroacetic acid
DFOM	Dark field optical microscopy
DFOMS	Dark field optical microscopy and spectroscopy
DI	De-ionized
DLS	Dynamic light scattering
DNA	Deoxyribonucleic acid
EM	Electron microscopy
EMCCD	Electron multiplying charge coupled device
FWHM	Full width at half maxima
h	Hour
H_2O_2	Hydrogen peroxide
hpf	Hours post fertilization
HRTEM	High resolution transmission electron microscopy
IME	Inner mass of embryo
K	Boltzman Constant
LSPR	Localized surface plasmon resonance
mm	Millimeter
MSD	mean-squared-displacement
MSI	Multi-spectral imaging
mV	Millivolt
nM	Nanomolar
nm	Nanometer
$NaBH_4$	Sodium tetrahydroBoride

NaCl	Sodium chloride
NPs	Nanoparticles
OC	Outside chorion
pM	Picomolar
QDs	Quantum dots
QY	Quantum yield
RTSD	Real-time-squared-displacement
SEM	Scanning electron microscopy
SMD	Single molecule detection
SPR	Surface plasmon resonance
T	Temperature in kelvin
TCDD	2, 3, 7, 8 – tetrachlorodibenzo-p-dioxin
TEM	Transmission electron microscopy
UV-vis	Ultraviolet- visible
W	Watt
WT	Wild type
YS	Yolk sac

TABLE OF CONTENTS

Page

Page

LIST OF FIGURES

CHAPTER I

OVERVIEW

Nanomaterials possess unique physical and surface properties, which have inspired plans for a wide spectrum of applications, such as target-specific vehicles for *in vivo* sensing, diagnosis, and therapy (e.g., nanomedicine, drug delivery).[1-5] These unique properties may also incite toxicity, damaging *in vivo* systems of interest and posing risks to human health and the environment.[6] Therefore, our primary focus was to probe the transport in real-time and concentration-dependent biocompatibility and toxicity of NPs in an *in vivo* model system and demonstrate the possibility of creating an *in vivo* assay using zebrafish embryos as a standard to study the biocompatibility and toxicity of nanomaterials. Establishing an *in vivo* assay enables the screening of NPs and determines their prospective use in a living system and the side effects caused by their exposure. Studying the transport and biocompatibility of NPs in real-time during early embryonic development will provide new information into the transport mechanisms and the interactions of NPs with the developing embryos. Different types of NPs have not yet been assessed for their biocompatibility and toxicity in an *in vivo* model system, so it is important to investigate the effects of their exposure. Hence, it is important to develop an *in vivo* assay to efficiently screen the biocompatibility and toxicity of NPs in real-time while investigating the transport mechanism.

We used silver (Ag) NPs as our model nanomaterials to study transport and biocompatibility in a developing embryo model system. The reason we choose to use Ag NPs is because noble metal NPs possess unique optical properties, such as, localized-surface-plasmon resonance (LSPR), which dependent upon their size and shape. This allows them to be directly imaged in the living system without any fluorescence excitation[3, 7-9]. Fluorescent dyes are a preference as probes for *in vivo* imaging, but these are obsolete because most fluorescence dyes suffer from photodecomposition and cannot be followed for a

---

The journal for this dissertation is *ACS Nano*

long period of time during development[10]. Noble metal NPs, such as Ag NPs, have been shown to be photostable and do not demonstrate photobleaching or photoblinking enabling them to be used as important and powerful imaging tool[11-15]. Silver NPs are extremely bright and can be directly observed and imaged using dark field optical microscopy and spectroscopy (DFOMS). Unlike fluorescent probes and quantum dots, noble metal NPs do not suffer photodecomposition or photoblinking and can be used as a probe to continuously monitor dynamic events for an extended period of time. Moreover, the LSPR spectra of nanoparticles shows size dependence, thus one can use the color (LSPR spectra) index of these multicolor nanoparticles as a nanometer size index to directly measure membrane transports of nanoparticles and determine the size of membrane pores at the nanometer scale in real-time[14, 15]. Size is important because it influences every aspect of nanoparticle function, including uptake mechanisms and nanoparticle clearance.

Zebrafish embryos were the *in vivo* model system of choice because they have characteristic beneficial features over other vertebrate model systems, such as the mouse, rat, and human. For example, zebrafish development is completed within 120 h and the stages are well documented.[16-20] Additionally, zebrafish embryos develop outside of their mothers and are transparent, which makes them easy to see and observe allowing for direct observation of normal, dead, deformed embryos. Zebrafish also share similarities to human genes and diseases, and the protein sequences of drug-binding receptors in zebrafish and humans show a high degree of affinity.[16, 20] Thus, zebrafish are an important *in vivo* model system for screening drugs for use against human diseases. Lastly, zebrafish are ideal because they generate many embryos fast and at minimal cost, which is an important factor for establishing an efficient and affordable *in vivo* assay for the screening of biocompatibility of different types of NPs.

The zebrafish as an *in vivo* model system has become commonplace for screening chemical toxicity[17] and drug biocompatibility[20], but it has not been used for the screening of biocompatibility and toxicity of NPs. Furthermore, in all

reported nanotoxicity studies, conventional toxicological assays were primarily used, which cannot characterize dose of nanoparticles *in vivo* and in real time. Typically, nanoparticles were injected into *in vivo* systems[6, 21], which is highly invasive. Many of these studies used unpurified nanoparticles or functionalized nanoparticles and did not consider effects of residual chemicals produced during nanoparticle synthesis persisting in nanoparticle solutions, leading to inconclusive results.[6]

It is important to utilize this valuable *in vivo* model system and establish an assay to look at the transport, biocompatibility and toxicity of NPs. Currently, the biocompatibility of NPs, used as labeling agents for imaging cells and organisms, are not well known. The primary challenges of establishing an *in vivo* assay for screening the effects of NPs are (i) to accurately monitor the transport and the death, deformity and normal phenotypes produced from exposure to the NPs, (ii) to develop an *in vivo* assay that would share similarities to humans to establish realistic biocompatibility and toxicity goals for human treatments and (iii) to establish a standard *in vivo* assay that is efficient, easy to use, and affordable for screening NPs. In the following dissertation, we accomplished all of these objectives, achieving a major advance in the *in vivo* screening of NPs.

In this dissertation, we developed new imaging and *in vivo* assay approaches to characterize the transport, biocompatibility and toxicity of different types of single silver (Ag) NPs, ranging from 12 to 95 nm. We imaged at nanometer resolution by measuring their size-dependent localized surface plasmon resonance (LSPR) spectra and scattering intensity in living embryos using dark-field optical microscopy and spectroscopy (DFOMS). These new approaches allowed us to characterize different types of single Ag NPs for simultaneous imaging of multiple single NPs in living embryos. We also were able to measure their sizes at nanometer resolution, with millisecond temporal resolution, using optical microscopy in real-time. This study offers powerful new tools to study multiple dynamic and molecular events of interest *in vivo* using

multiple single NP optical probes and a valuable *in vivo* model assay *via* optical microscopy.

This dissertation includes seven chapters. In Chapter I, we provide a brief overview of the research background and significance of this dissertation research, and outline the contents of each chapter.

In Chapter II, we describe the design of a standard *in vivo* assay that is efficient, easy to use, and affordable to screen the transport, biocompatibility and toxicity of 12 nm Ag NPs. These new approaches allowed us to create an *in vivo* assay to screen single Ag NPs for biocompatibility while simultaneously imaging and measuring sizes of multiple single NPs in real-time using DFOMS, as illustrated in Figure 1. We were able to synthesize, characterize and purify Ag NPs, 12 nm in size and incubated them with our living *in vivo* model system. We determined that the Ag NPs (12 nm) were stable in the egg-water media and were able to transport into the embryos *via* random diffusion causing various deformities in a dose-dependent manner. This study offers powerful new tools to study the dynamics of *in vivo* transport of NPs and the biocompatibility and toxicity of NPs, as described in Chapter III-VI.

In Chapter III, we utilize the Ag NP optical probes and imaging approaches developed in Chapter II to probe the transport kinetics of Ag NPs used in Chapter II in our *in vivo* model system at different stages of development in real-time at nanometer resolution, as illustrated in Figure 2. We found that NPs transport into the embryos in a stage-dependent manner causing stage specific related deformity. This experiment demonstrates that plasmonic Ag NP probes can be used to study the stage dependent effects during embryonic development in single living embryos, offering the possibility of better understanding the questions of development.

In Chapter IV, we used the zebrafish embryos as our *in vivo* model system and imaging methods described in Chapter II to screen the transport, as well as

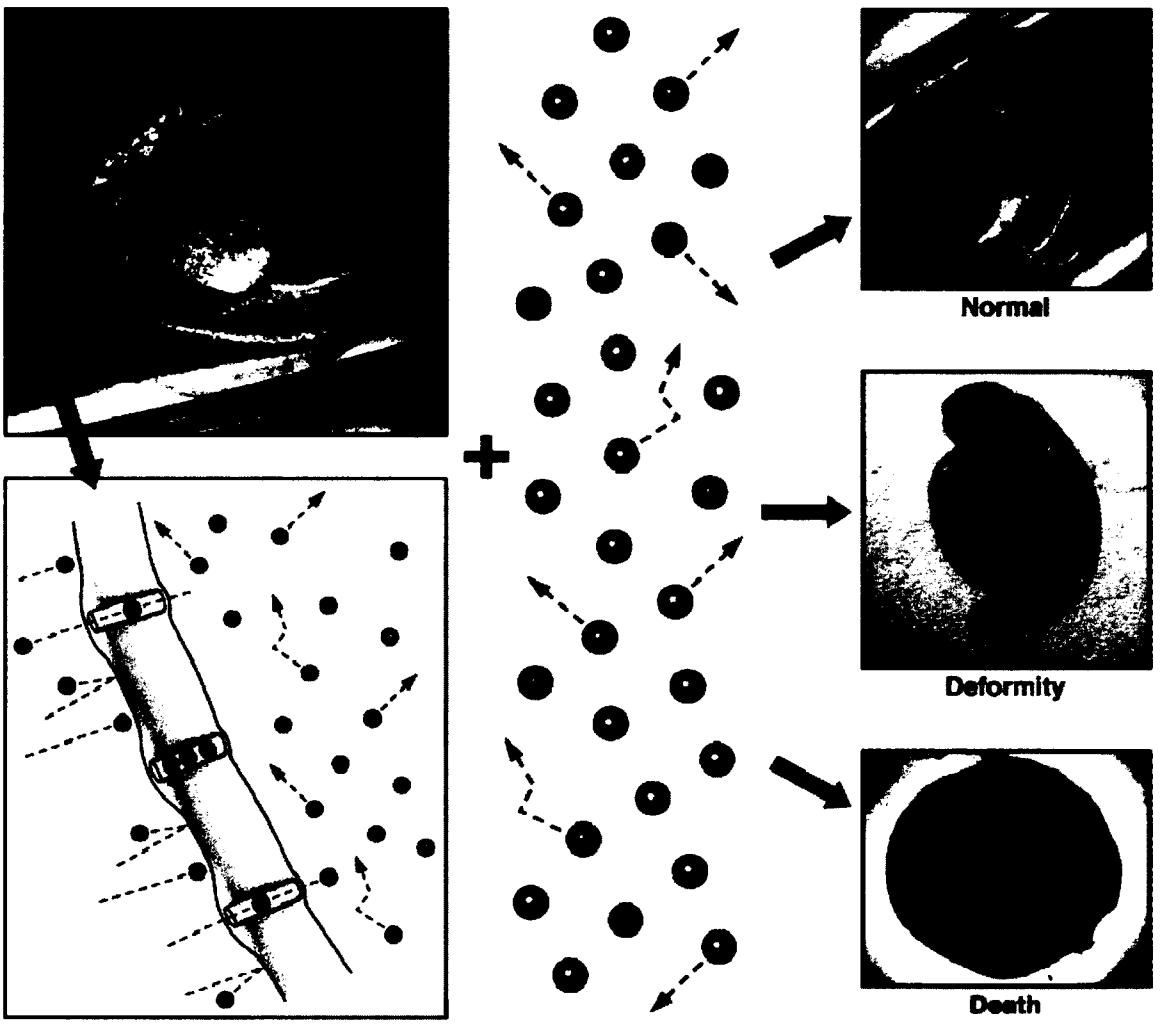

Figure 1. Illustration of transport, biocompatibility and toxicity of single Ag NPs in zebrafish embryos as an *in vivo* model system via DFOMS.

biocompatibility and toxicity of Ag NPs with different surface charges, as illustrated in Figure 3. Unlike other NP biocompatibility experiments, we utilized the purified single Ag NPs (12 nm) from Chapter II and conjugated them with different peptides to create different surface charges to determine NPs surface

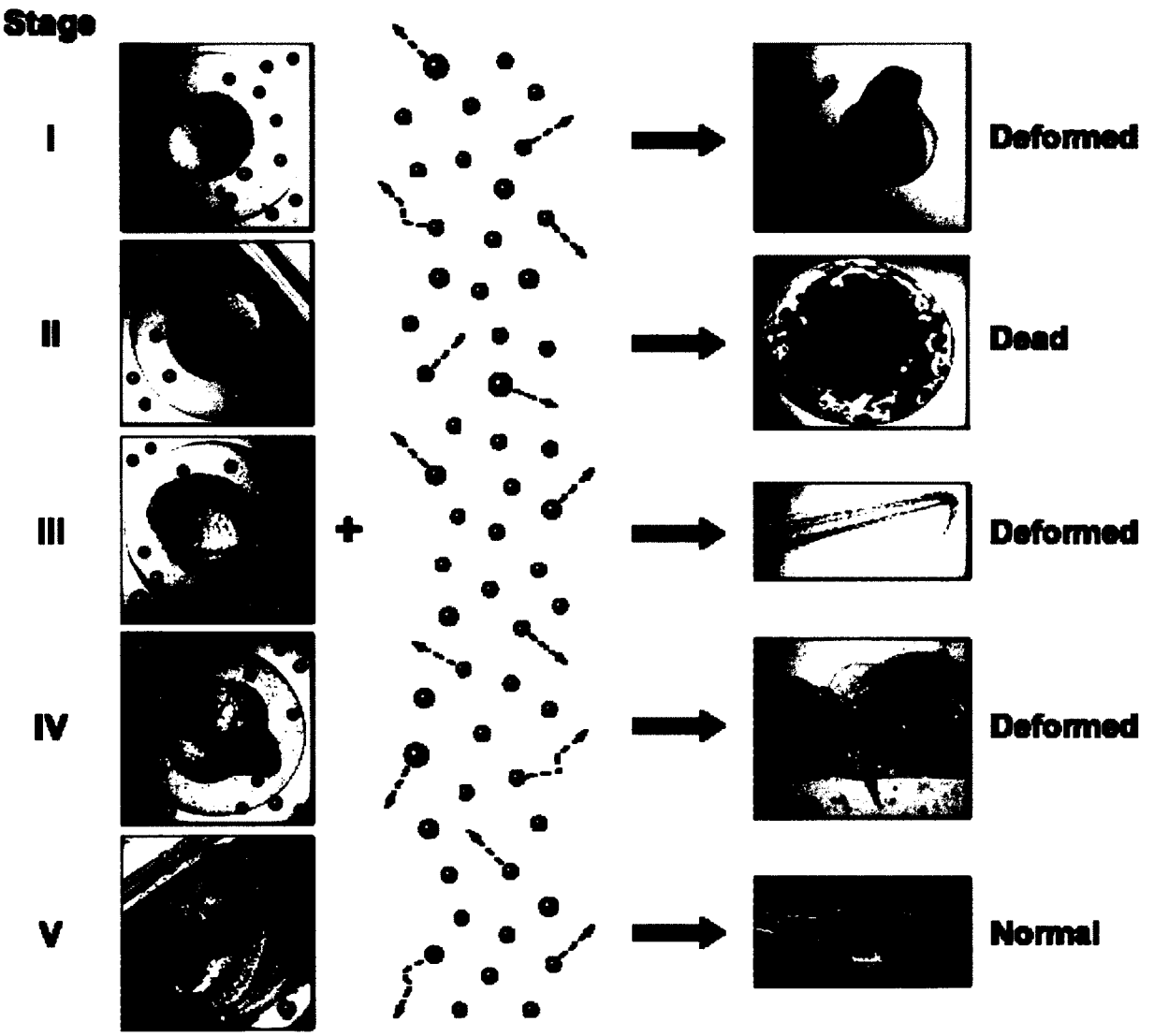

Figure 2. Illustration of probing of stage-dependent transport, biocompatibility and toxicity of single Ag NP probes using zebrafish embryos.

Charge affects on developing zebrafish embryos in real-time. We determined that these Ag-peptide NPs were also stable in the egg-water media prior to incubation with the embryos. Interestingly, we found that our *in vivo* model system displayed charge-dependent biocompatibility and toxicity. This illustrates

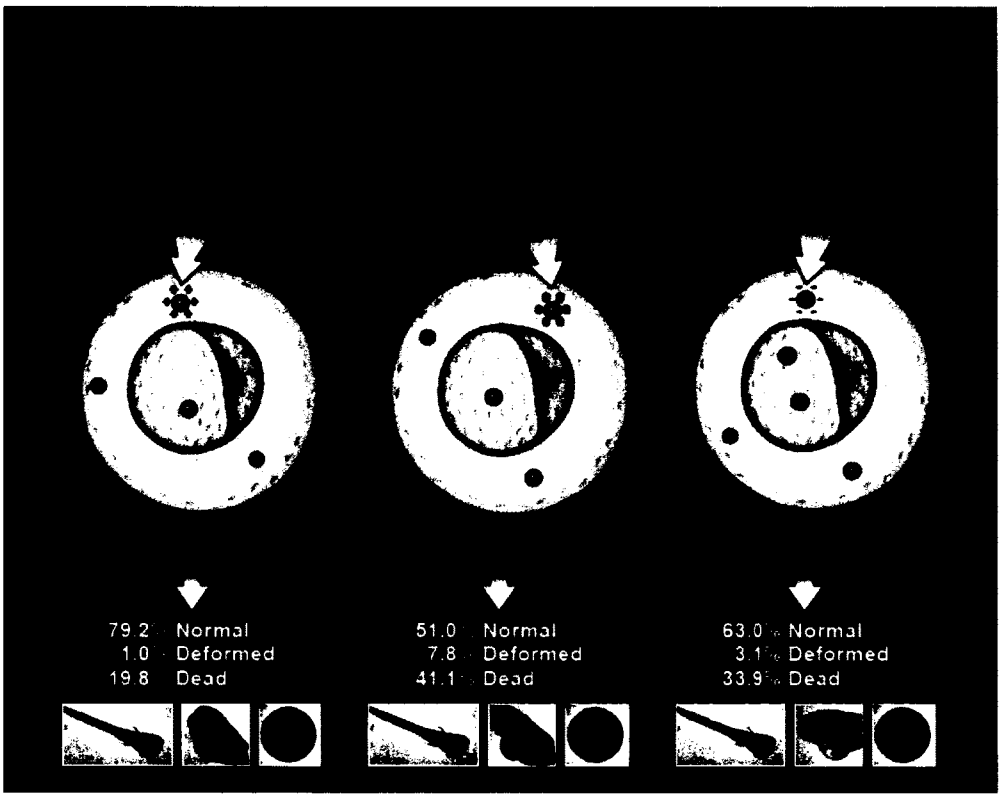

Figure 3. Illustration of using Ag-peptide NPs as optical probes with varying surface charges for transport, biocompatibility and toxicity in living zebrafish embryos in real-time.

the possibility of using different surface charged NPs, that are more biocompatible, to probe the dynamics of embryonic development.

In Chapter V, we describe the synthesis and characterization of purified larger Ag NPs (42.3 ± 6.3 nm) that are stable in egg-water medium. We studied their biocompatibility and toxicity *in vivo*, as illustrated in Figure 4. Using imaging approaches described in Chapter II, we observed the effects of larger Ag NPs on the morphology, viability and transport of embryos at single NP and single live embryo resolution. We found that the larger Ag NPs were more toxic, showing dose-dependency, highly dependent upon the concentration of the nanoparticles,

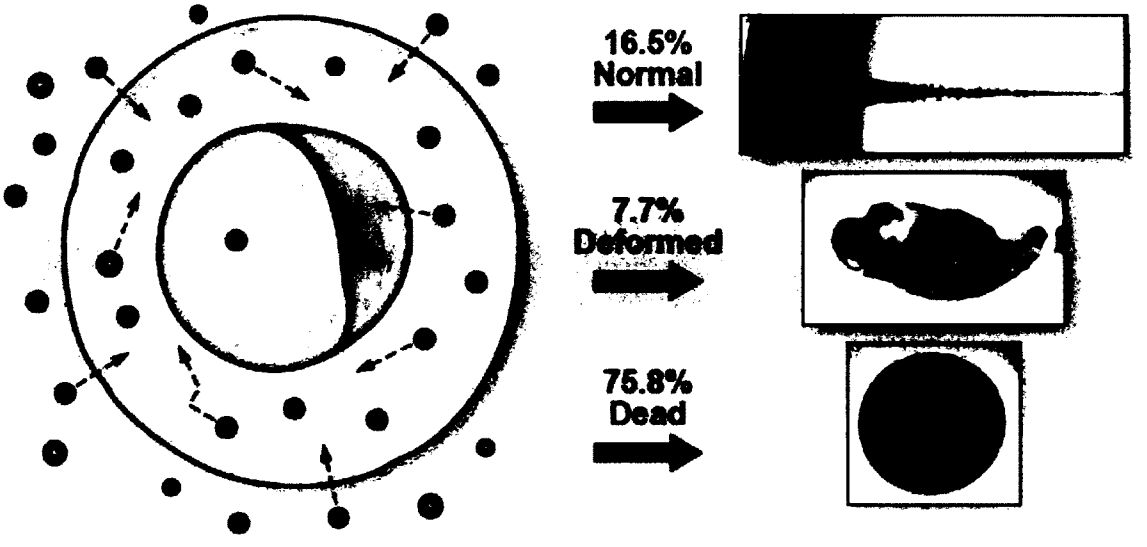

Figure 4. Illustration of using larger sized 42 nm single NP optical probes for transport, biocompatibility and toxicity in living zebrafish embryos in real-time.

demonstrating drastic changes in embryo morphology and an increase in the amount of dead embryos. This work demonstrates the possibility of using smaller Ag NPs (12 nm) as a more biocompatible embryonic probe for potential therapeutic drug carriers.

In Chapter VI, we synthesized and characterized larger (95 nm) single molecule Ag NP optical probes, making sure that they were stable in egg-water media. We then used these single NP probes to map the transport and biocompatibility and toxicity of large NPs on single living embryos in real-time, as illustrated in Figure 5. We found that the larger NPs were more toxic and were

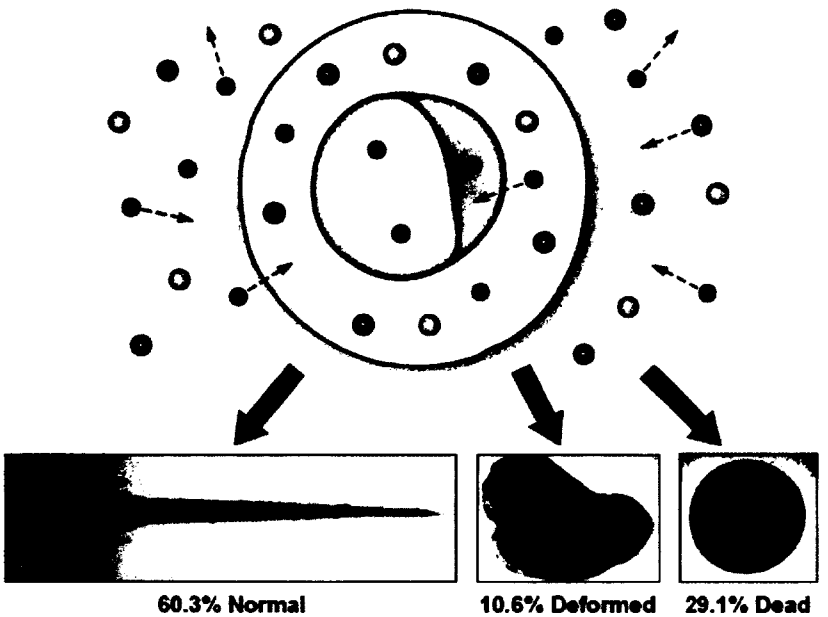

Figure 5. Illustration of transport of 95 nm Ag NPs in single living embryos and their biocompatibility and toxicity.

The results demonstrate that size does matter when related to NPs and that smaller NPs are more suitable for quantitative imaging and probing of single living embryos for any desired period of time. This offers new possibilities for monitoring the dynamics of embryonic development in single living embryos in real-time, emphasizing the importance of the study of NP transport, biocompatibility and toxicity on single living embryos.

In Chapter VII, we summarized our research findings described in the preceding chapters, pointed out the primary contributions of these original research activities, and emphasized the possible future research directions.

CHAPTER II

REAL-TIME IMAGING OF TRANSPORT, BIOCOMPATIBILITY AND TOXICITY OF SINGLE 12 NM SILVER NANOPARTICLES IN EARLY DEVELOPMENT OF ZEBRAFISH EMBRYOS

INTRODUCTION

We select an effective *in vivo* model system (zebrafish embryos) and one type of model nanomaterial (12 nm Ag nanoparticles) and focus on probing the transport mechanism and dose-dependent biocompatibility of the nanomaterials *in vivo,* targeting the initial entry step of nanomaterials into embryos. The aim is to demonstrate the Ag NPs potential applications and address its potential adverse effects. Real-time study of transport and biocompatibility of single nanoparticles in early development of embryos will provide new insights into molecular transport mechanism and structure of developing embryos at nanometer (nm) spatial resolution *in vivo.* As well as, assess the biocompatibility of single nanoparticle probes *in vivo*.

RESULTS AND DISCUSSION

Synthesis and Characterization of Ag NPs

We synthesized spherical Ag NPs with average diameter of (11.6 ± 3.5) nm by reducing $AgClO_4$ with reducing agents (sodium citrate and sodium borohydride) using well-tuned synthesis conditions as described in Methods. We then carefully washed nanoparticles to remove trace chemicals from their synthesis using centrifugation, generating highly purified nanoparticles. We characterized the stability, size and optical properties of these purified Ag nanoparticles incubated in egg-water (1.2 mM NaCl) for 120 h using UV-vis absorption spectroscopy, DFOMS, dynamic light scattering (DLS), and high-resolution transmission electron microscopy (HR-TEM) (Fig. 6).

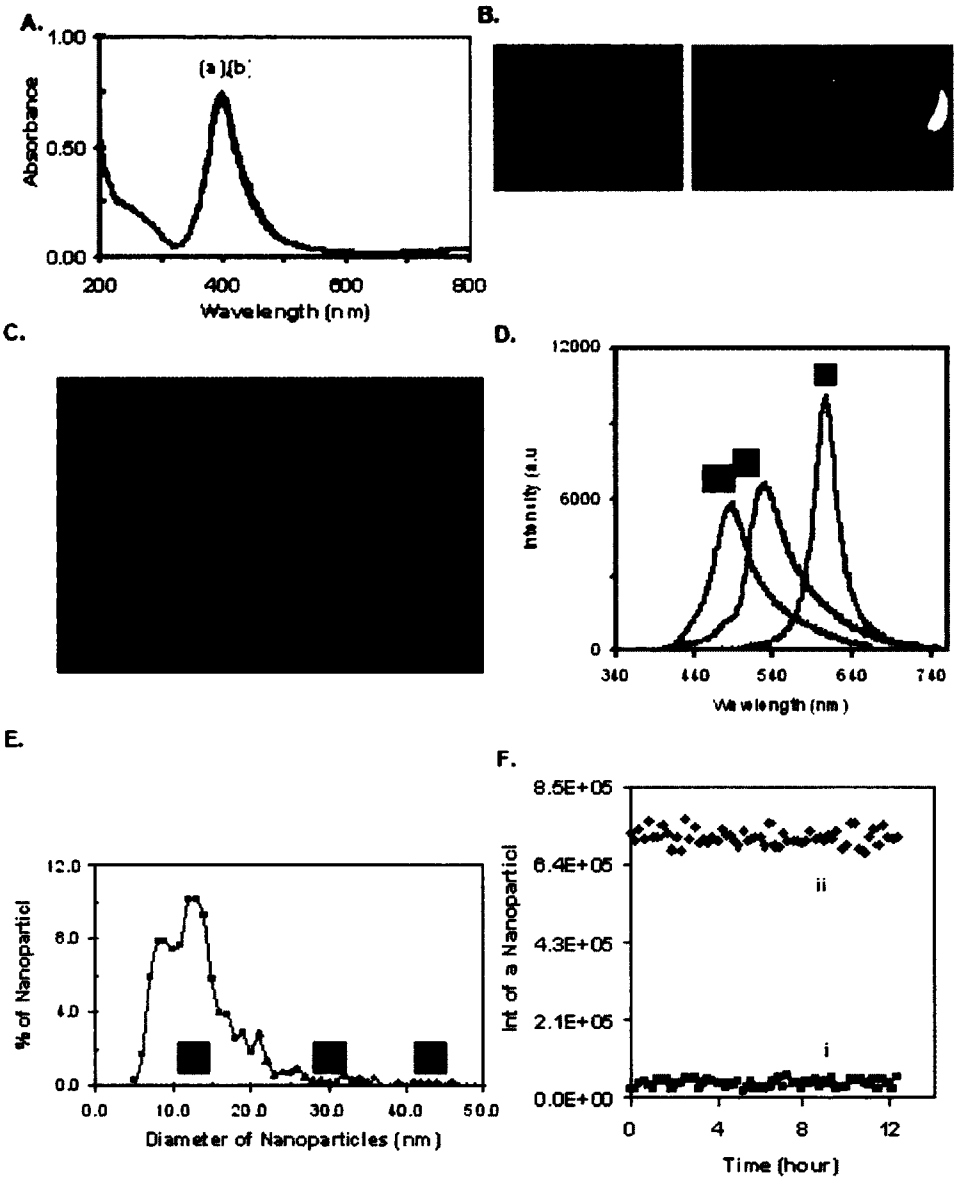

Figure 6. Characterization of optical properties and stability of Ag nanoparticles.

(A) Representative UV-vis absorption spectra of 0.71 nM Ag NPs for (i) 0 and (ii) 120 hours (B) Representative HR-TEM images Ag NPs. Scale bar = 5 nm. (C) Representative dark-field optical image of single Ag NPs shows the majority are blue. (D) Representative LSPR spectra of single Ag NPs exhibit peak wavelength at 452, 531, and 601 nm, respectively. (E) Histogram of size and color distribution of nNPs to be 11.6 ± 3.5 nm, with 74% of 5-15 nm (blue), 23% of 16-30 nm (green), and 1% of 31-46 nm (red) Ag nanoparticles. (F) Representative plots of scattering intensity of single NPs (i) and background (ii).

The absorption spectra of freshly prepared and washed nanoparticles before and after incubating with egg-water for 120 h (Figs. 6A: a & b) show an absorbance of 0.736 at a peak wavelength of 396-400 nm, indicating that Ag nanoparticles are very stable (not aggregated) in egg-water (1.2 mM NaCl). We determined the effect of salt concentration (the positive control experiment) by increasing NaCl concentration and found that nanoparticles are stable in the presence of NaCl up to 10 mM, but begin to aggregate in 100 mM NaCl, showing a red shift of peak absorbance wavelength (~2-3 nm) and a decrease in absorbance. The size of nanoparticles measured by DLS increased from (10.1 ± 2.0) nm to (24.4 ± 2.7) nm in the presence of 100 mM NaCl. The presence of sufficiently high concentration of NaCl (100 mM) appears to reduce the thickness of electric double-layer on the surface of nanoparticles and decrease the zeta potential below its critical point, leading to aggregation of nanoparticles.

We characterized the size of Ag NPs using HR-TEM and DLS before and after incubating with egg-water for 120 h, showing that the size of nanoparticles remained unchanged with an average diameter of 11.6 ± 3.5 nm. Furthermore, we characterized the optical properties of individual nanoparticles using DFOMS (Fig. 6: C-F). A representative optical image of single nanoparticles in Fig. 5C illustrates that the majority of nanoparticles are blue with some being green and few are red. The representative LSPR spectra of single blue, green and red nanoparticles show peak wavelengths of 488, 532 and 607 nm (Fig. 6D), respectively. The correlation of the color distribution of individual nanoparticles with their size measured by HR-TEM, shows the majority (74%) of single nanoparticles with diameters of 5-15 nm are blue, 23% of single nanoparticles with diameters of 16-30 nm are green, and a very small fraction (1%) of nanoparticles (31-46 nm) are red (Fig. 6E). Thus, the color-index of single nanoparticles can be used as a size-index to directly distinguish and determine the size of nanoparticles (5-46 nm) using DFOMS, even though the size of nanoparticles cannot be directly measured due to the optical diffraction limit. We also found that the distribution of color and size of nanoparticles remained

unchanged as nanoparticles were incubated in egg-water for 120 hr, suggesting that nanoparticles are stable (not aggregated) in egg-water at single-nanoparticle resolution.

To determine the photostability of Ag nanoparticles, we acquired sequence images of single Ag nanoparticles while these nanoparticles were constantly radiated under a dark-field microscope illuminator (100 W halogen) for 12 hr. The illumination power at the sample stage (focal plane of dark field) was 0.070 ± 0.001 Watt. Representative plots of scattering intensity of single nanoparticles and background (in the absence of nanoparticles) versus illumination time in Fig. 6F indicate that the scattering intensity of individual single nanoparticles remains unchanged over 12 h, showing that single Ag nanoparticles resist photodecomposition and blinking. Note that the small fluctuations of intensity of single nanoparticles (Fig. 6F: i) are similar to those observed from the background (Fig. 6F: ii), suggesting that the intensity fluctuations are attributable to the illuminator and the noise level of the CCD camera.

Probing Diffusion and Transport of Single Nanoparticles in Cleavage Stage Embryos

Representative developmental stages of the zebrafish embryos in 120 hour-post-fertilization (hpf) in Fig. 7 show the cleavage stage (8-64 cell stages), segmentation stage, hatching stage, and pharyngula stage embryos, and a fully developed zebrafish in the absence of nanoparticles. At the cleavage-stage (8-64 cell stage; 0.75-2.25 hpf) (Fig. 7A-B), embryos undergo dramatic changes (e.g., rapid cellular division and distinct fate establishment) to lay down the foundation for developing the different parts of organs and a variety of interesting but not yet well-understood biochemical and biophysical events (e.g., cell migration signaling and embryonic pattern formation) occur. This stage is crucial in development as the foundation and organization of the embryos are being assembled.[22, 23] Thus, it is important to understand the diffusion and transport

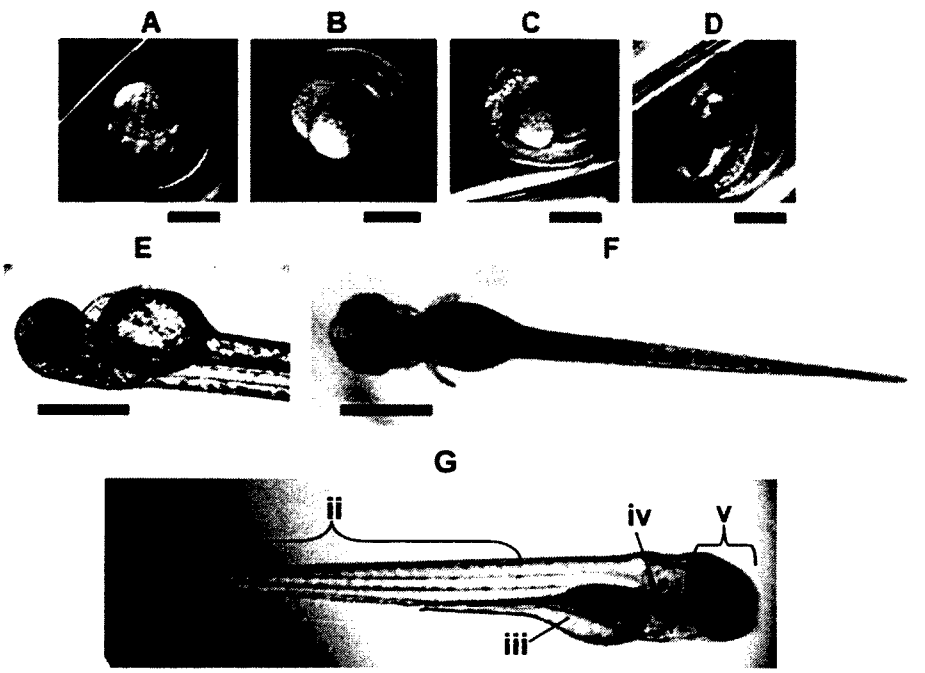

Figure 7. Optical images of the representative developmental stages of normally developed zebrafish in egg-water (in the absence of nanoparticles) and representative anatomical structures.

(A) 1.25-1.50 hpf (8-cell stage); (B) 2-2.25 hpf (64-cell stage); (C) 24 hpf (segmentation stage); (D) 48 hpf (hatching stage); (E) 72 hpf (pharyngula stage); (F) a completely developed zebrafish at 120 hpf and (G) representative anatomical structures of the zebrafish: (i) finfold, (ii) tail region, (iii) yolk sac, (iv) heart, and (v) eye. Scale bar = 500 μm. hpf = hour post fertilization.

mechanisms among the various parts of embryos at this particular stage. The cleavage stage embryos may also be most sensitive to foreign substances[24], offering an ultrasensitive *in-vivo* model system to study the biocompatibility and subtle effects of nanoparticles on the embryonic development.

To study diffusion and transport of single nanoparticles into cleavage stage embryos, we incubated Ag nanoparticles with the embryos and directly observed and characterized their transport. We found that Ag nanoparticles (blue, green and red) transport into the chorionic space (cs) via chorion pore canals (CPCs) and enter into the inner mass of embryo (ime) (Fig. 8). We used our optical imaging system to directly measure the diameters of chorion pore canals, showing them to be approximately 0.5-0.7 μm in diameter with distances between the centers of two nearby chorion pore canals are at ~1.5-2.5 μm, which agrees well with those reported using TEM.[25] To our knowledge, this study demonstrates for the first time direct observation of chorionic pore canals of single living embryos using optical microscopy. We show that the sizes of chorion pore canals are much larger than the size of nanoparticles, permitting the passive diffusion of individual nanoparticles into the chorionic space of embryos.

To determine the transport mechanism of Ag nanoparticles, we utilized the concept of 2D mean-square-displacement (MSD) and diffusion models (e.g., directed, simple and stationary Brownian diffusion)[26, 27] to investigate each diffusion trajectory of single nanoparticles in egg-water, entry into embryos, and inside embryos. To follow the diffusion of single nanoparticles inside various parts of embryos in real-time, we used real-time square-displacement (RTSD) (diffusion distance at a given time interval), instead of average (mean) of square-displacement over time, because the diffusion coefficient could vary as single nanoparticles diffuse in embryos. This approach allowed us to probe the diffusion of single nanoparticles and viscosity of the different parts of embryonic fluids (e.g., chorionic space, inner mass of embryo) in real-time. The diffusion coefficient (D) of single nanoparticles in simple Brownian motion is calculated by dividing the slope of a linear plot of real-time square-displacement versus time by 4 (Note: RTSD = $4D\Delta t$).

Representative diffusion trajectories of single Ag nanoparticles trapped inside chorion pore canals, in chorionic space and near the inner mass of embryo, and analysis of these diffusion trajectories using the real-time square-

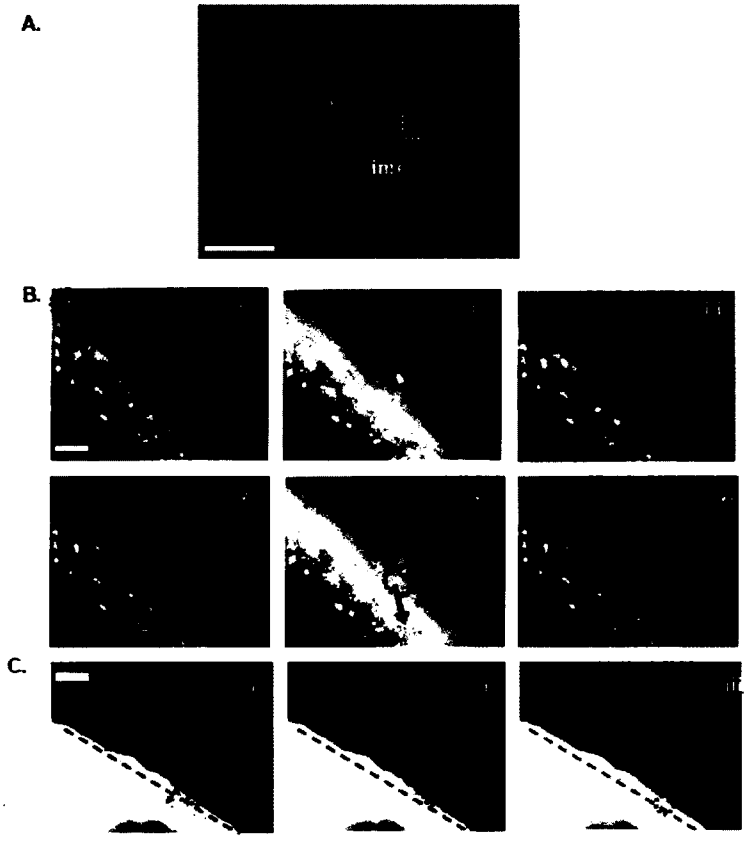

Figure 8. Real-time monitoring and characterization of transport of individual Ag nanoparticles in a cleavage-stage living embryo .

(A) Optical image of a cleavage-stage embryo shows chorionic space (CS), yolk sac (YS), and inner mass of embryo (IME). (B) Sequence dark-field optical images illustrate the transport of single Ag nanoparticles, as indicated by the circle, from the egg-water (extra embryo) into the chorionic space via an array of chorion pore canals (CPCs) highlighted by a rectangle. (C) Sequence dark-field optical images illustrate the transport of single Ag NPs, as indicated by the circle, from chorionic space into inner mass of embryo. The straight and curved dashed-lines illustrate the interface of inner mass of embryo with chorionic space, and chorionic space with egg-water, respectively. The time interval of each sequence image in both (B) and (C) is 25 s. Scale bar = 400 μm in (A) and 15 μm in (B-C).

displacement method are shown in Fig. 9. The results illustrate that single Ag nanoparticles inside the chorionic space (either near the chorion layers or inner mass of the embryo) exhibit simple Brownian diffusion (not active transport) with ~26 times slower diffusion rate ($3x10^{-9}$ cm^2/s) than those in egg-water ($7.7x10^{-8}$ cm^2/s), showing that single Ag nanoparticles diffuse into the chorionic space via passive diffusion and that the viscosity of chorionic space is about 26 times higher than that of egg-water.

As nanoparticles make several attempts to enter the chorion layers and inner mass of the embryo, their diffusion patterns are restricted (Fig. 9B: a-i, steps in a-ii and a-iii), suggesting that the nanoparticles dock into the chorion pore canals, which halts their normal diffusion. By tracking the entry of individual nanoparticles into chorion pore canals, we measured the period of time that individual nanoparticles stay in the pores, which ranges from 0.1 to 15 s.

We characterized the diffusion coefficient of blue, green and red nanoparticles in egg-water (Fig. 9B: b) to determine the possible variation of diffusion coefficients due to the different sizes (radii) of single nanoparticles, showing simple Brownian diffusion with D of 8.4 $x10^{-8}$, 6.0 $x10^{-8}$ and 5.5 $x10^{-8}$ cm^2/s, respectively. The diffusion coefficients are inversely proportional to their radius, as described by the Stoke-Einstein equation, $D = kT/(6\pi\eta a)$, showing that the diffusion coefficient (D) depends on the viscosity of medium (η) and the radius (a) of solute (nanoparticle).[28, 29] The diffusion coefficients of the given color (radius) of nanoparticles in embryos were studied and compared with those in egg-water, showing that the various diffusion coefficients observed in three different parts of embryos (Fig. 9B: a) were indeed attributable to the viscosity gradient inside embryos, but not the different radii of individual nanoparticles.

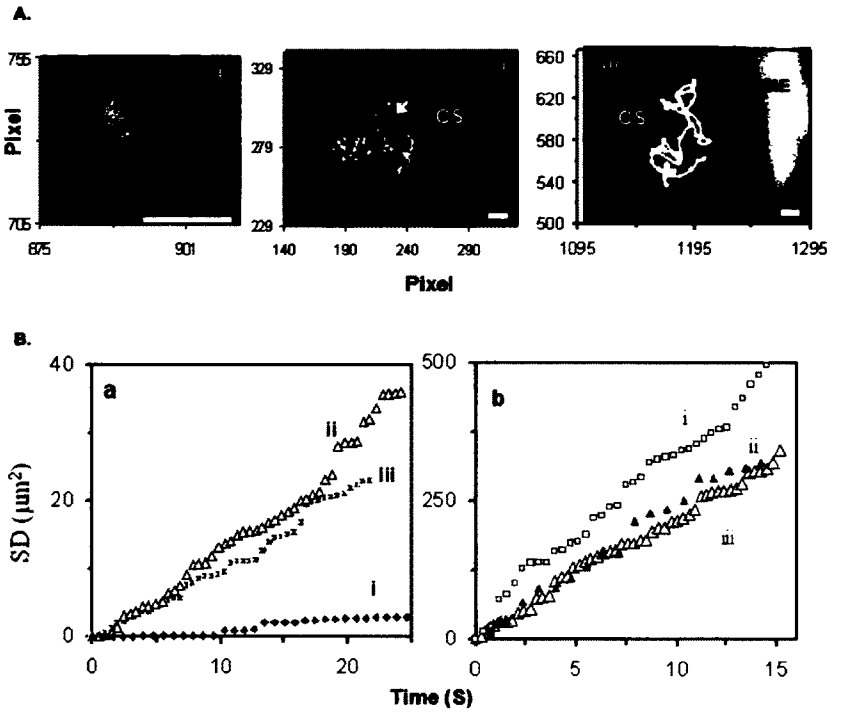

Figure 9. Characterization of transport and diffusion of single Ag NPs in a cleavage (64-cell) stage living embryo.

(A) Diffusion trajectories of single Ag nanoparticles: (i) a red nanoparticle inside the chorion layers, (ii) a blue nanoparticle inside chorionic space, and (iii) a green nanoparticle at the interface of inner mass of embryo and chorionic space. (B) Plots of real-time square-displacement (RTSD) as a function of time: (a) single nanoparticles from the diffusion trajectories shown in A (i-iii) illustrate that (i) a red nanoparticle in a restricted and stationary diffusion mode with a diffusion coefficient (D) < 1.9×10^{-11} cm^2/s, due to entrapment inside chorion pore canals; (ii) a blue nanoparticle in chorionic space away from the inner mass of embryo; and (iii) a green nanoparticle inside chorionic space near the surface of inner mass of embryo, both in a simple Brownian motion with D of 3.4×10^{-9} cm^2/s and 2.6×10^{-9} cm^2/s, respectively; (b) a representative single (i) blue, (ii) green and (iii) red nanoparticle in egg-water. All show simple Brownian diffusion with D of 8.4 $\times 10^{-8}$, 6.0 $\times 10^{-8}$ and 5.5 $\times 10^{-8}$ cm^2/s, respectively.

Imaging and Characterization of Transport and Embedded Nanoparticles

Images of single nanoparticles diffusing into the chorionic space were recorded using DFOMS equipped with a color camera, instead of CCD, showing that nanoparticles of multiple colors transport into the chorionic space (Fig. 10A). Note that single Ag nanoparticles exhibit colors (LSPR), which depends on its size, shape and surrounding environments.[30-33] This feature allowed us to distinguish single Ag nanoparticles from any possible tissue debris or vesicle-like particles in embryos, which do not exhibit surface plasmon and hence appear white under dark-field microscope (Figs. 8 & 9). We found that the majority of NPs transported into the chorionic space and some of them overlapped with chorion pore canals (Fig. 10A: a). The representative LSPR spectra (colors) of individual nanoparticles inside chorionic space (Fig. 10A: b) show similar peak wavelengths as those observed in egg-water in Fig. 6D. The results indicate that the majority of nanoparticles remained non-aggregated inside embryos. Otherwise, we would have observed a significant red shift of LSPR spectra of individual nanoparticles.

Although the majority of single nanoparticles can freely diffuse into embryos and remain non-aggregated, some single nanoparticles stay in chorion pore canals for an extended period of time. These trapped nanoparticles serve as nucleation sites and aggregate with incoming nanoparticles to form larger particles (dark-red nanoparticles) (Fig. 10B), clogging chorion pore canals and affecting the embryo's transport. Note that, embryos at this developmental stage are free of pigmentation.

As the cleavage (8-cell) stage embryos chronically treated with lower concentrations of Ag nanoparticles (< 0.08 nM) completed their embryonic development at 120 hpf, we characterized Ag nanoparticles embedded in fully developed zebrafish using DFOMS and found that these Ag nanoparticles embedded in multiple organs (retina, brain, heart, gill arches, and tail) of normally developed zebrafish (Fig. 11), demonstrating that Ag nanoparticles are biocompatible to embryos at lower concentrations (< 0.08 nM). The LSPR spectra of these embedded nanoparticles are similar to those observed in Figure

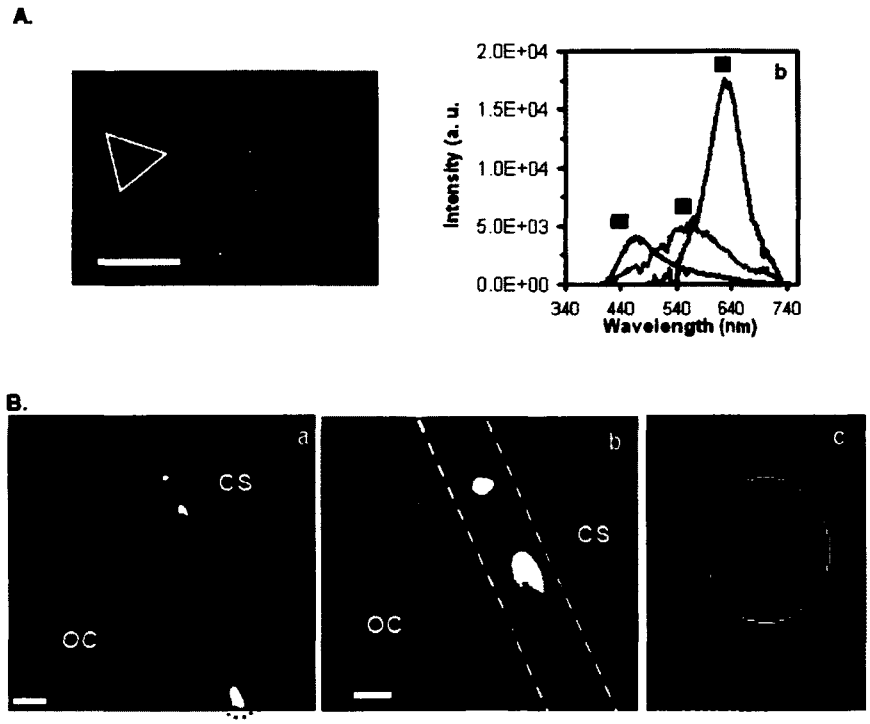

Figure 10. Characterization of Ag nanoparticles embedded in embryos using dark-field DFOMS.

(A) Representative (a) color image and (b) LSPR spectra of single Ag nanoparticles embedded in chorion layers show that single Ag nanoparticles with multiple-colors (blue, green, red) are present inside chorion layers, and some nanoparticles are overlapped with the chorion pore canals (note that an array of chorion pore canals are highlighted by a triangle). Scale bar = 1 μm. (B) Representative images of individual Ag nanoparticles embedded in the chorion layers illustrate those Ag nanoparticles (as indicated by a circle) trapped in the chorion pore canals outlined by ellipses. The CCD image in (a) is enlarged and shown in (b). The zoom-in color image of (b) is shown in (c), indicating that the dark-red nanoparticles clog the chorion pore canals. Scale bar = 10 μm in (a); 2 μm in (b). OC = outside chorion

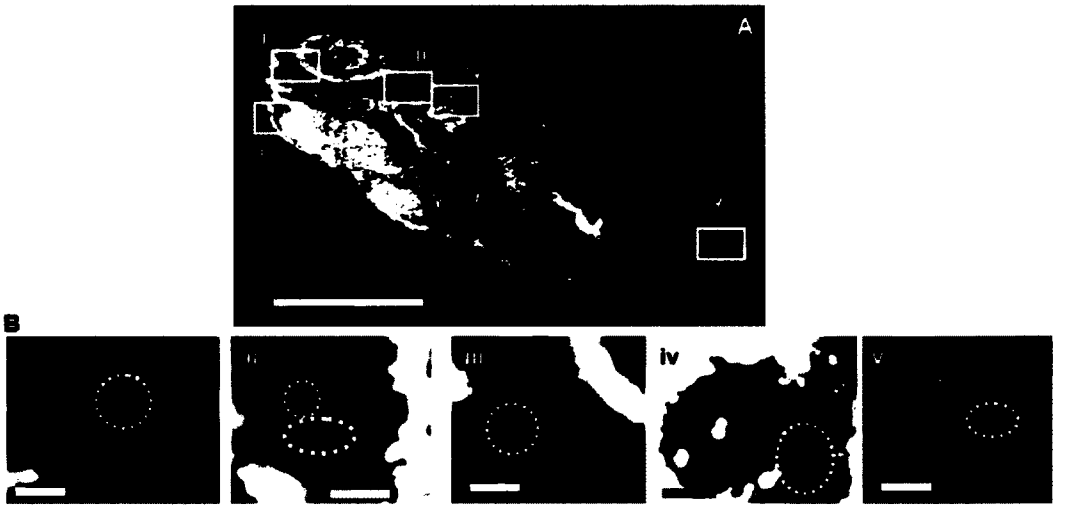

Figure 11. Characterization of individual Ag nanoparticles embedded inside a fully developed (120 hpf) zebrafish using DFOMS:
(A) Optical image of a fixed normally developed zebrafish. The rectangles (i-v) highlight representative areas: (i) retina, (ii) brain (mesencephalon cavity), (iii) heart, (iv) gill arches, and (v) tail. (B) Zoom-in optical images of single Ag nanoparticles embedded in those tissue sections outlined in (A). Dashed circles outline the representative embedded individual Ag nanoparticles. Scale bar = 400 μm in (a); 4 μm in (b).

9A:b. We also performed blank control experiments by imaging 120-hpf zebrafish that developed in the absence of nanoparticles and did not observe the signature LSPR spectra (color) of Ag nanoparticles in these fully developed zebrafish.

Dose-dependent biocompatibility and toxicity

To determine the effect of dose of Ag nanoparticles on embryonic development, we treated the cleavage stage (8-cell stage) embryos chronically with various concentrations of Ag nanoparticles (0 - 0.71 nM) and carefully monitored and characterized their vital developmental stages (24, 48, 72, 96, and

120 hpf). The results in Fig. 12 A & B show that biocompatibility of Ag nanoparticles and the types of abnormalities in treated zebrafish are highly dependent on the dose of Ag NPs. In the presence of lower concentrations (< 0.08 nM) of nanoparticles, a higher percentage of normally developed zebrafish is observed than that of dead and deformed zebrafish. Note that both normal and deformed zebrafish developed from the cleavage (8-cell) stage embryos that had been simultaneously incubated with the same nanoparticle solution. Thus, the results suggest that some embryos might be more tolerant to the nanoparticles than others. The results also suggest that Ag nanoparticles might affect the development of embryos stochastically due to the random diffusion of nanoparticles.

As nanoparticle concentration increases, the number of normally developed zebrafish decreases, while the number of dead or deformed zebrafish increases (Fig. 12: a). As nanoparticle concentration increases beyond 0.19 nM, only dead and deformed zebrafish are observed, showing a critical concentration of Ag nanoparticles on the development of zebrafish embryos (Fig. 12). The blank (negative) control experiments, conducted by replacing nanoparticles with the supernatant resulting from washing Ag nanoparticles, show that the survival rate of zebrafish is independent of the dose of supernatant (Fig. 12: b), demonstrating that residual chemicals from nanoparticle synthesis are not responsible for the deformation and death of zebrafish, but rather the nanoparticles that were used to treat the zebrafish embryos (Fig. 12: a).

The number of deformed zebrafish increased to its maximum as nanoparticle concentration increased to 0.19 nM, and then decreased as nanoparticle concentration increased from 0.19 to 0.71 nM (Fig. 12: c) because the number of dead zebrafish increased. Interestingly, the types of viable deformities exhibit high dependence on the nanoparticle concentration (Fig. 12: d). For example, the finfold abnormality and tail/spinal cord flexure and truncation were observed in zebrafish treated with all tested nanoparticle

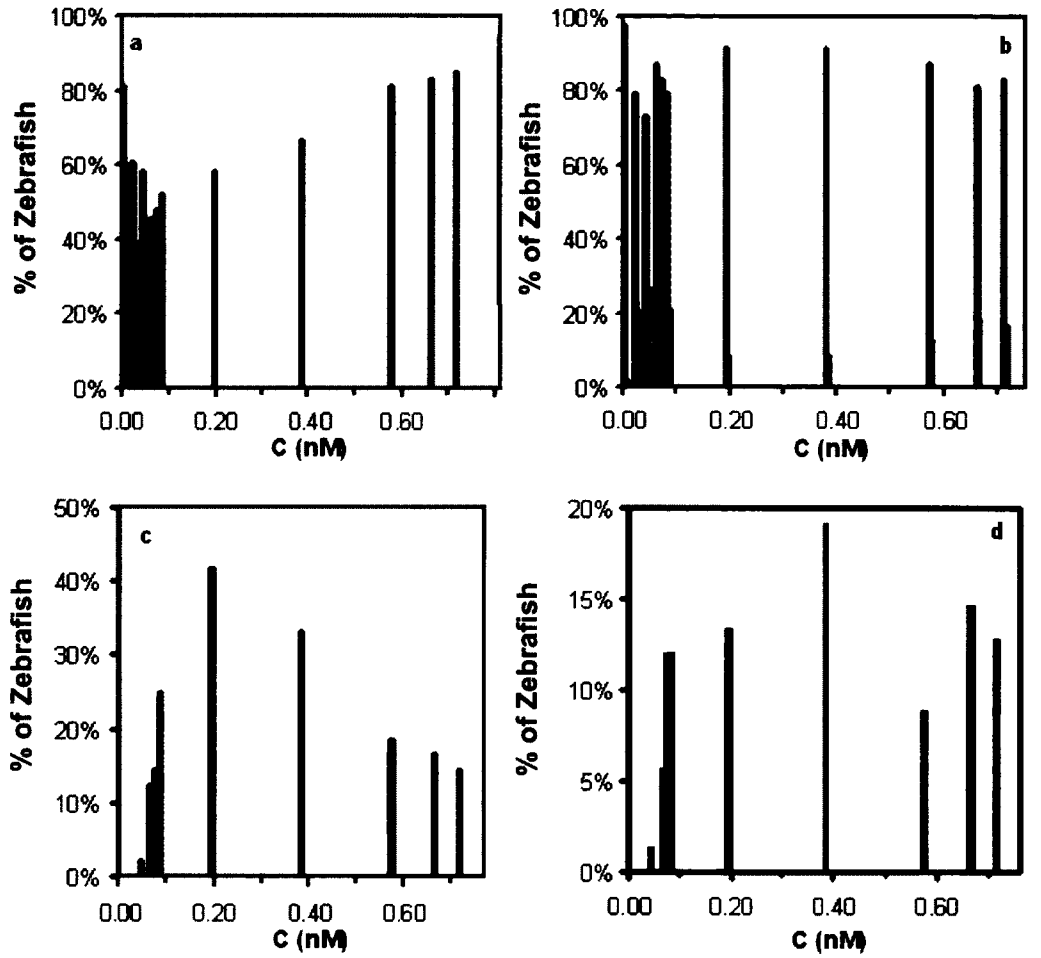

Figure 12. Biocompatibility and toxicity of nanoparticles show high dependence on nanoparticle concentration.

Histogram of distribution of normally developed (■) and dead (■) zebrafish, (a) versus concentration of Ag nanoparticles; (b) versus concentration of supernatants resulting from washing Ag nanoparticles (negative control); (c) histogram of distribution of deformed zebrafish (120 hpf) (■) versus concentration of Ag nanoparticles; (d) histogram of distribution of five representative types of deformities of the zebrafish versus concentration of Ag nanoparticles: finfold abnormality (■), tail and spinal cord flexure and truncation (■), cardiac malformation (■), yolk sac edema (■), head edema (■), and eye abnormality (■).

concentrations (0.04-0.71 nM) with the highest occurrences at 0.19 and 0.38 nM, respectively. Cardiac malformation and yolk sac edema were observed in zebrafish treated with the slightly higher nanoparticle concentrations (0.07-0.71 nM) with the highest occurrences at 0.66 nM. In contrast, head edema and eye deformity were only observed in the higher concentrations of nanoparticles, 0.44-0.71 and 0.66-0.71 nM, respectively. Among all types of observed deformities, finfold abnormality occurred at the highest rate, followed by tail and spinal cord flexure and truncation, then cardiac malformation and yolk sac edema, and finally head edema and eye abnormality, which were rarely observed deformations of zebrafish and quickly led to zebrafish death.

Representative deformed zebrafish induced by nanoparticles are illustrated in Fig. 13:b-g. In comparison with the normally developed zebrafish in Fig. 13-a, we found characteristics of finfold abnormality (Fig. 13-b), tail and spinal cord flexure and truncation (Fig. 13-c), cardiac malformation (Fig. 13-d), yolk sac edema (Fig. 13-e), head edema (Fig. 13-f), and eye abnormality (Fig. 13-g) of zebrafish that developed from the 8-cell embryos treated chronically by Ag nanoparticles. Interestingly, multiple deformities occurred in one zebrafish at the higher nanoparticle concentrations (> 0.38 nM). For example, in yolk sac edema zebrafish, we also observed tail/spinal cord flexure, finfold abnormality, and cardiac malformation (Fig. 13: c-iv & e-ii), head edema (Fig 13: e-ii, e-iv and f-ii), and eye abnormality (Fig 13: g-i). These findings suggest that specific embryonic developmental pathways might be co-regulated, and that some deformities (e.g., finfold, tail, spinal cord) are much more sensitive to the nanoparticles than others (e.g., head edema, eye abnormality).

To determine the possible targets for further genomic and proteomic studies and evaluate the toxicity of Ag nanoparticles against well-studied toxic chemicals, such as cadmium, dichloroacetic acid (DCA), 2,3,7,8-tetrachlorodibenzo-p-dioxin (TCDD), and ethanol, we compare the characteristics of deformation of zebrafish induced by Ag nanoparticles with those generated by well-known toxic chemicals. We found that the observed finfold abnormality and tail/spinal cord flexure and truncation induced by Ag nanoparticles (Fig. 13: b & c)

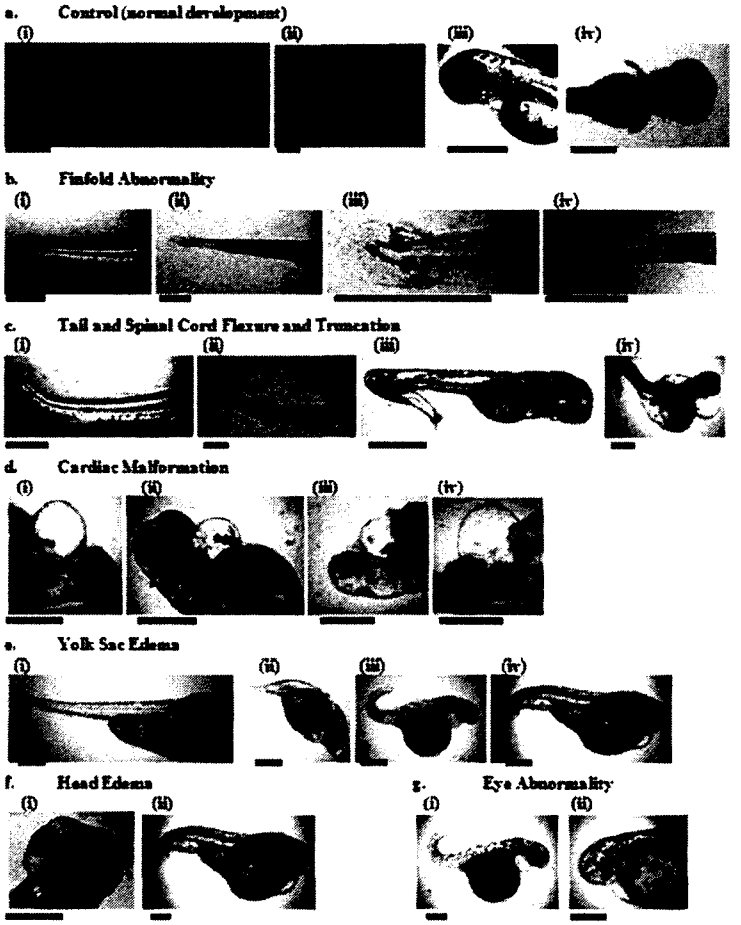

Figure 13. Biocompatibility and toxicity of nanoparticles show high dependence on nanoparticle concentration.

Representative optical images of (a) normally developed and (b-g) deformed zebrafish: (a) the normal development of (i) finfold, (ii) tail/spinal cord, (iii) cardiac, (iii-iv) yolk sac, cardiac, head and eye; and (b-g) deformed zebrafish: (b) finfold abnormality; (c) tail and spinal cord flexure and truncation; (d) cardiac malformation; (e) yolk sac edema; (f) head edema: (i) head edema; (ii) head edema and eye abnormality; (g) eye abnormality: (i) eye abnormality; (ii) eyeless. Scale bar = 500 μm.

are similar to those treated by DCA and cadmium[34, 35], indicating possible common targets of malformation during development. The observed cardiac malformation and yolk sac edema in this study (Fig. 13: d & e) are also similar to those treated with DCA and cadmium.[34, 35] The shrunken ventricular myocardium observed in cardiac malformed zebrafish induced by nanoparticles (Fig. 13: d) is similar to those treated with TCDD.[36] Head edema and eye abnormality in Fig. 13B: f & g-i have also been found in treatment of zebrafish with cadmium.[34]

Although the eye malformation (a cycloptic eye development) had been observed in zebrafish treated by ethanol,[37] the deformation is unlike what we have observed (eyeless, no formation of retina or lens) in Fig. 13B: g-ii. Thus, the eyeless deformation (Fig. 13B: g-ii), an undeveloped set of optic cups with no retina or eye lens, to our knowledge, is a new occurrence of malformation that has not been reported previously. This abnormality may be related to the nanoparticles disrupting the regulators or signaling cascades involved with the normal development of the neural retinal layers and the lens of the zebrafish's eye. Pax-6, a transcription factor, has been studied and shown to affect the development of the eye retinal layers. In Pax-6 mutants, the lens fails to develop.[37, 38] However, another transcription factor, Six-6, regulating neural retinal development in zebrafish has not been studied in detail and it may also play the role in eye deformation as well.[38] Further studies are needed to determine whether Ag nanoparticles inhibit or regulate the expression of transcription factors (e.g., Pax-6 and Six-6), leading to the eyeless deformation.

Plausible explanations for the high dependence of embryonic abnormalities on the dose of nanoparticles include the following: (i) The rate of passive diffusion (permeability) and accumulation of nanoparticles in chorion pore canals and embryos highly depends on the concentration gradient of nanoparticles. Thus, the dose of nanoparticles plays a vital role in determining the rate and amount of nanoparticles that can penetrate into particular compartments of embryos, and the rate and number of chorion pore canals blocked by the aggregation of nanoparticles (Figs. 9 - 11). (ii) The accumulated nanoparticles inside embryos can also alter the charge, diffusion, and

interactions of biomolecules (e.g., nucleic acids, proteins such as transcription factors, signaling molecules) in a dose-dependent manner, leading to interference or malfunctioning of signaling cascades.

Taken together, these results suggest that specific pathways of embryonic development respond to Ag nanoparticles in a dose dependent manner, and demonstrate that the nanoparticles may elicit unique response from embryonic neural development pathways. The study demonstrates the possibility of fine-tuning the dose of nanoparticles to (i) selectively target specific pathways to create particular phenotypes, (ii) selectively generate specific mutations in zebrafish, and (iii) serve as potential therapeutic agents to treat specific disorders in embryonic development. Unlike other chemicals, single nanoparticles can be traced and imaged inside developing embryos and developed zebrafish with nanometer spatial resolution in real-time, offering new opportunities to unravel the related pathways that lead to the abnormalities. Work is in progress to identify the related specific pathways and signaling cascades at the genomic and proteomic levels and to further explore potential therapeutic effects of nanoparticles.

SUMMARY

In summary, we have designed, synthesized and characterized single nanoparticle optical probes (individual Ag nanoparticles) for probing their transport, biocompatibility and toxicity in early development of zebrafish embryos in real-time. We have shown that single Ag nanoparticles resist photodecomposition and blinking and can be directly monitored in embryos for an extended period of time. Furthermore, individual Ag nanoparticles exhibit size-dependent LSPR spectrum (color), which permits us (i) to distinguish them from tissue debris and vesicles in embryos, (ii) to directly image and characterize the sizes of individual nanoparticles in solution and in living embryos in real time, (iii) to probe their diffusion, transport mechanism and biocompatibility in living embryos in real time, and (iv) to investigate the embryonic fluids (e.g., viscosity) at nm spatial resolution in real time. We found that individual Ag nanoparticles

can passively diffuse into developing embryos via chorion pore canals, create specific effects on embryonic development and selectively generate particular phenotypes in a dose-dependent manner. The early embryos are highly sensitive to the nanoparticles, showing the possibility of using zebrafish embryos as an *in vivo* assay to screen the biocompatibility and toxicity of nanomaterials. This study represents the first direct observation of passive diffusion of nanoparticles into an *in vivo* system (an important aquatic species), suggesting that the release of large amounts of Ag nanoparticles into aquatic ecosystems (e.g., rivers) may have drastic environmental consequences, should the sizes of nanomaterials remain unchanged during environmental transport. This study also represents the first most rigorous study and characterization of nano-toxicity and nano-biocompatibility ever performed by investigating the effect of highly purified nanoparticles *in vivo* in real time and considering the effect of possible trace chemicals from nanoparticle synthesis.

METHODS

Reagents and Supplies

Sodium citrate (99%), $AgClO_4$ (99%), $NaBH_4$ (98%), and NaCl were purchased from Sigma-aldrich. All reagents were used as received. The nanopure water (18 MΩ water, Barnstead) was used to prepare all solutions and rinse glassware.

Synthesis and Characterization of Ag NPs

Silver nanoparticles were synthesized by reducing a 0.1 mM silver perchlorate solution with a freshly prepared ice-cold solution of 3 mM sodium citrate and 10 mM sodium borohydride under stirring overnight, and filtered through a 0.22 μm filter.[39, 40] The nanoparticles were washed twice with nanopure water using centrifugation to remove the chemicals involved in nanoparticle synthesis, and the nanoparticle pellets were resuspended in

nanopure water before incubating with embryos. The washed Ag nanoparticles are very stable (non-aggregated) in nanopure water for months and remain stable in egg-water throughout the entire experiments (120 hpf). The supernatants of nanoparticle solutions after the second washing were collected for control experiments to study the effect of trace chemicals involved in nanoparticle synthesis on the development of embryos. The concentration, optical properties, and size of nanoparticles were characterized using UV-vis spectroscopy, dark-field optical microscopy and spectroscopy (DFOMS)[40-42], high-resolution transmission electron microscopy (HR-TEM) (FEI Tecnai G2 F30 FEG), and dynamic light scattering (DLS) (Nicomp 380ZLS particle sizing system), respectively. Our DFOMS has been well described previously for real-time imaging and spectroscopic characterization of single nanoparticles in single living cells and for single molecule detection.[29, 40-44] The detector, EMCCD or LN back-illuminated CCD camera coupled with a SpectraPro-150 (Roper Scientific), was used in this study. All chemicals were purchased from Sigma and used without further purification or treatment.

To determine the photostability of single Ag nanoparticles, we acquired sequence images of single Ag nanoparticles using EMCCD camera with exposure time at 100 ms and readout time of 40.6 ms while these nanoparticles were constantly radiated under dark-field microscope illuminator (100 W halogen) for 12 hr. The illumination power at the sample stage (focal plane of dark field) is 0.070 ± 0.001 Watt. The integrated scattering intensity of single nanoparticles and background (in the absence of nanoparticles) within a 20x20 CCD pixel area was measured. The integrated scattering intensity of background is subtracted from that of same size of detection area in the presence of individual nanoparticles to calculate the scattering intensity of single nanoparticles. The experiments were repeated at least three times. The average subtracted integrated intensity of the single nanoparticles and background was plotted as a function of time. The fluctuations of intensity of single nanoparticles were used to

compare with those of background to determine the photostability (photodecomposition and blinking) of single nanoparticles.

Breeding and Monitoring of Zebrafish Embryos

Wildtype adult zebrafish (Aquatic Ecosystems) were maintained, bred, and collected, as described previously.[45] Embryos were collected and transferred into a petri dish containing egg-water (1.2 mM stock salts in DI water), washed twice with egg-water to remove the surrounding debris, and placed into 24-well plates with each well containing two embryos in egg-water. Each developmental stage of embryos in the wells was directly imaged by bright-field optical microscopy using an inverted microscope equipped with a 4x objective and a digital camera.

***In vivo* Characterization and Analysis of Transport and Dose-dependent Biocompatibility and Toxicity of Nanoparticles**

Cleavage-stage living embryos (8-64 cell stage; 0.75-2.25 hpf) that had been incubated with 0.19 nM nanoparticles for a given time (0-2 hours) were either immediately imaged to investigate the transport of nanoparticles into embryos or carefully rinsed with DI water to remove external nanoparticles, and placed in a self-made microwell containing DI water to image the diffusion and transport of nanoparticles inside the embryos in real-time using our DFOMS.

To study the dose-dependent effects of nanoparticles on embryonic development, a dilution series of washed Ag nanoparticle solutions (0, 0.04, 0.06, 0.07, 0.08, 0.19, 0.38, 0.57, 0.66, and 0.71 nM) were incubated chronically with cleavage (8-cell) stage embryos in egg-water for 120 hpf. Each experiment was carried out at least three times and total number of embryos at 35-40 was studied for each individual concentration to gain representative statistics. Nanoparticle concentrations were calculated as described previously.[46] Embryos in egg-water in the absence of nanoparticles and in the presence of supernatant were placed

in two rows of the 24-well plates as control experiments of untreated embryos and probing the effect of possible trace chemicals from nanoparticle synthesis, respectively. The embryos in the 24-well plates were incubated at 28.5°C, and directly observed at room temperature using an inverted microscope equipped with a digital camera at 24, 48, 72, 96, and 120 hpf.

Characterization of Nanoparticles Embedded Inside Embryos and Fully Developed Zebrafish

To characterize the embedded nanoparticles in the tissues of treated zebrafish, we selected living developed zebrafish that had been chronically incubated with a given concentration (0.04 nM) of nanoparticles for 120 hpf since their cleavage (8-cell) stage, and carefully rinsed the zebrafish with DI water to remove external nanoparticles. The fixed zebrafish were prepared using 10% buffered formalin via a standard histology protocol of tissue sample preparation.[47] The thin-layer microsections (~5 μm thickness) were prepared by carefully dissecting tissues of interest (e.g., eye retina, brain, heart, gill arch, tail and spinal cord) under microscopy using microtome. The embedded nanoparticles in the tissues were directly characterized using DFOMS (Fig. 11).

CHAPTER III

STUDY OF STAGE DEPENDENT TRANSPORT, BIOCOMPATIBILITY AND TOXICITY OF SINGLE 12 NM SILVER NANOPARTICLES USING EARLY DEVELOPMENT OF ZEBRAFISH EMBRYOS

INTRODUCTION

Nanoparticles (NPs), with their small size and unique physical properties, are ideal for use in probing the nano-environments of living organisms enabling the study of the changing environment of a developing living organism at specific developmental stages of embryonic development.[3, 9, 48-50] NP probes can be used in a variety of applications for new insight into developmental processes, such as development screening tools in developmental biology to investigate the embryonic internal environment, to potentially control and regulate certain processes in development, and to target specific system regulators for biomedical biological uses. Nanomaterials could possibly demonstrate developmental stage dependent regulation of deformity type induced, suggesting that the nanomaterials, at higher concentration, may interact with target developmental pathways of interest. In this study, we used our previously described nanomaterials,[11] Ag NPs, and an effective embryo developmental model system, zebrafish embryos, and focused on acute developmental stage-dependent diffusion and biocompatibility targeting important developmental stages for analysis and independent NP entry into each embryonic stage, hoping to identify possible developmental stage applications and the ability for NPs to enter the developing embryo independent of the time of development.

The zebrafish has been used as a model organism for many chemical-screening and drug studies; however the acute biocompatibility on different zebrafish developmental stages is limited.[51, 52] The acute biocompatibility of Ag NPs on specific sensitive stages of embryonic development has, to our knowledge, never been attempted. It is important to explore the transport and

biocompatibility of Ag NPs acutely at specific stages of embryonic development to access the ability of Ag NPs to be used for *in vivo* imaging at any embryonic stage of development as well as probes in real-time to explore the changing embryonic environment during development.

The main challenges of using NP probes for specific developmental stages for *in vivo* imaging and probing the environmental changes of the developing embryo are (i) to ensure that the NPs transport into the embryo environment regardless of the stage of development into the physiological medium without any aid, such as microinjection (ii) to be able to track the transport, diffusion and characterization of individual NPs *in vivo* at different embryonic stages of development to study the differences in the embryonic fluid environment, and (iii) to be able to study the biocompatibility of the NPs at specific stages of embryonic development to assist in determining the NP interactions. In this study, we have accomplished all of these objectives, achieving a major advance in the study of single NPs *in vivo*.

RESULTS AND DISCUSSION

Synthesis and Characterization of Ag nanoparticles (NPs)

We used our previously developed sphere-shaped silver-based nanoparticles that were washed to remove any chemicals that remained from the synthesis to study their interactions and biocompatibility with key stages in developmental biology to determine Ag NPs role in developmental processes, including stage dependent morphological responses and concentration dependent morphological responses, for the potential of use as developmental intermediates for biomedical applications.[11] We characterized the stability, size and optical properties of the purified Ag NPs in egg-water embryo media (1.2 mM NaCl) for 120 hrs using UV-vis absorption spectroscopy, dark field optical microscopy and spectroscopy (DFOMS) and high resolution transmission electron microscopy (HRTEM).

We characterized the size of the Ag NPs using HRTEM and the size was with an average diameter of 13.1 ± 2.5 nm (Fig. 14A and B). A representative optical image of Ag NPs in Fig. 14C illustrates that majority of NPs appear to be blue with some green and a few red. These results suggest that Ag NPs are uniform in size and shape based on their color (LSPR). The representative LSPR spectra of single blue, green and red Ag NPs with peak wavelengths (λ_{max}) at 468 nm (blue) (FWHM = 38 nm), 554 nm (green) (FWHM = 47 nm), and 659 nm (red) (FWHM = 47) nm, respectively (Fig. 14D). Thus color of Ag NPs can be used as size index to directly distinguish and determine the size of NPs using DFOMS, even though size of NPs cannot be directly measured due to the optical diffraction limit. The number of NPs per image, using 20 images, at t_0, t_0 +12h, t_0 +24h, t_0 +48h, t_0 +72h, t_0 + 96h and t_0 +120h were determined to be 65 ± 0, 66 ± 2, 67 ± 3, 67 ± 4, 70 ± 5, 67± 3 and 67± 4 (Fig. 14E). We found that the number of NPs remained relatively unchanged when incubated in egg-water for 120 hrs. The absorbance spectra of freshly prepared and purified Ag NPs before and after the incubation time with egg-water demonstrated a peak wavelength (λ_{max}) at 392 nm (FWHM = 64 nm) and remained unchanged for 120hrs (Fig. 14F). The unchanged number of NPs and stable absorbance spectra indicates that the Ag NPs are very stable in egg-water media and remain non-aggregated.

Characterization of transport of nanoparticles (NPs) in different stage embryos

The normal course of embryonic development in zebrafish in the absence of NPs for each acute treatment stage is depicted in Fig 15. Acute treatment occurred at five different stages of development for a 2 h incubation time with NPs: stage I, cleavage stage (2-4 hpf) (Fig. 15A (a)), stage II, gastrula stage (6- 8 hpf) (Fig. 15A (b)), stage III, early segmentation stage (12 - 14 hpf) (Fig. 15A (c)), stage IV, late segmentation stage (21- 23 hpf) (Fig. 15A (d)) and stage V, during the hatching period (48 - 50 hpf) (Fig. 15A (e)). The stages were determined by

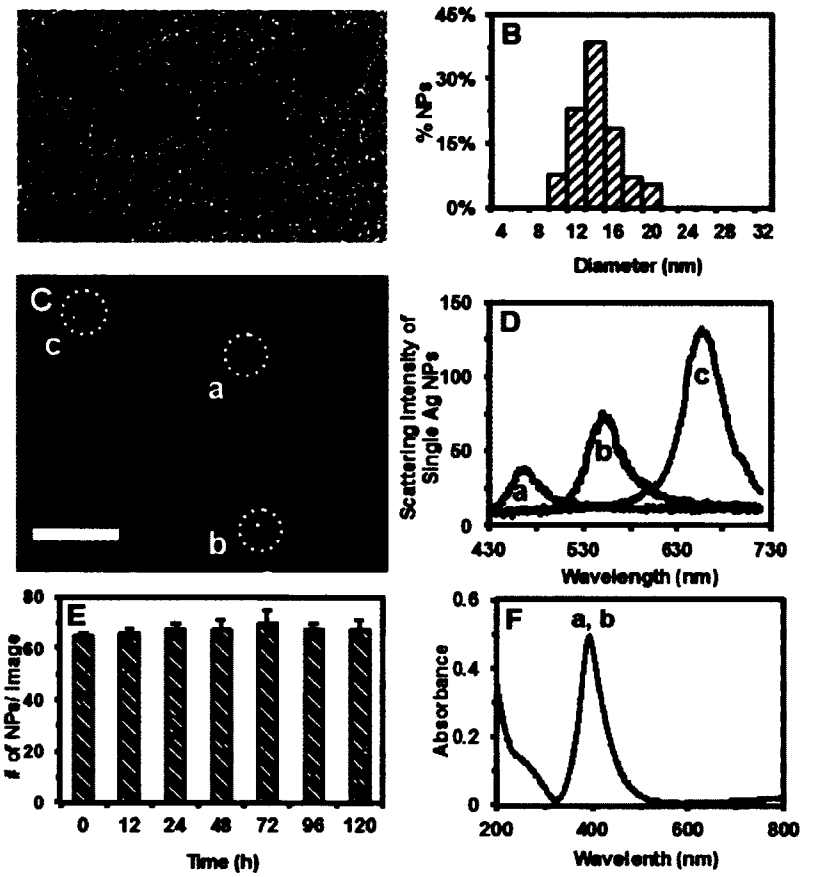

Figure 14. Characterization of optical properties and stability of Ag NPs

(A) Representative HRTEM image demonstrates the size and spherical shape of single Ag NPs. Scale bar = 10 nm. (B) Histogram of size distribution of Ag NPs measured by HRTEM shows the average size to be 13.1 ± 2.5 nm. (C) Representative dark-field optical image of single Ag NPs shows that majority of NPs are blue with some green and red. Scale bar = 2 μm. (D) LSPR spectra of single Ag NPs with multiple colors (blue, green, and red), with peak wavelengths (λ_{max}) at (a) 468 nm (blue) (FWHM = 38 nm), (b) 554 nm (green) (FWHM = 47 nm), and (c) 659 nm (red) (FWHM = 47 nm). (E) The # of NPs/ image (20 images) at t_0, t_0 +12h, t_0 +24h, t_0 +48h, t_0 +72h, t_0 + 96h and t_0 +120h were , 65 ± 0, 66 ± 2, 67 ± 3, 67 ± 4, 70 ± 5, 67± 3 and 67± 4. (F) Representative UV-Vis absorption spectra of 0.70 nM Ag NPs well-dispersed in egg-water at 28^0C for (a) 0 and (b) 120 h shows the peak absorbance at 0.491 and peak wavelength at 392 nm (FWHM = 64 nm) and remains unchanged for 120 h.

choosing critical events in embryonic development for study with NP transport and biocompatibility. During stage I, embryos undergo dramatic changes, such as rapid cellular division and embryonic pattern formation.[22, 23] During stage II, embryos undergo cell movements and migration and establishment of the early organ systems.[53, 54] In stage III, embryos begin somitogenesis and notochord formation, which is important for proper development of the axial skeleton, the vertebrate spinal column, and the skeletal muscle.[53, 55] During stage IV, embryos undergo development of the circulatory system and the heart is being formed.[53] During stage V, the embryo is in the hatching stage and finishing its development. It is important to understand the diffusion and transport mechanisms among the various embryonic stages to investigate the differences in the embryonic environment and determine which developmental process may be most sensitive to the NPs.

Embryos at each stage were observed throughout development after acute treatment with NPs. Stage I – IV embryos were observed after acute treatment at 24 hours post fertilization (hpf) (Fig. 15B (a)), 48 hpf, (Fig. 15B (b)), 72 hpf, (Fig 15B (c)), 96 hpf, (Fig. 15B (d)), and 120 hpf, (Fig. 15B (e)). Stage V embryos were observed after acute treatment at 72 hpf through 120 hpf, (Fig. 15B (c-e)).

Probing transport and diffusion of single Ag NPs in different stage embryos

To study the transport and diffusion of single Ag NPs into different stage embryos, we incubated 0.2 nM Ag NPs at the specific embryonic developmental stages as demonstrated in Figure 16 A-E and directly observed and characterized their transport at important areas of transport into the embryo through the chorion layers (CL) (Fig. 16A-E (a)) into the chorionic space (CS) (Fig. 16A-D (b)) via the chorion pores and into the inner mass of the embryo (IME) (Fig. 16A-D (c)). We were not able to characterize transport of the Ag NPs in the CS and IME of stage V due to the movement of the zebrafish larvae. We used our state of the art optical imaging system to directly measure the transport

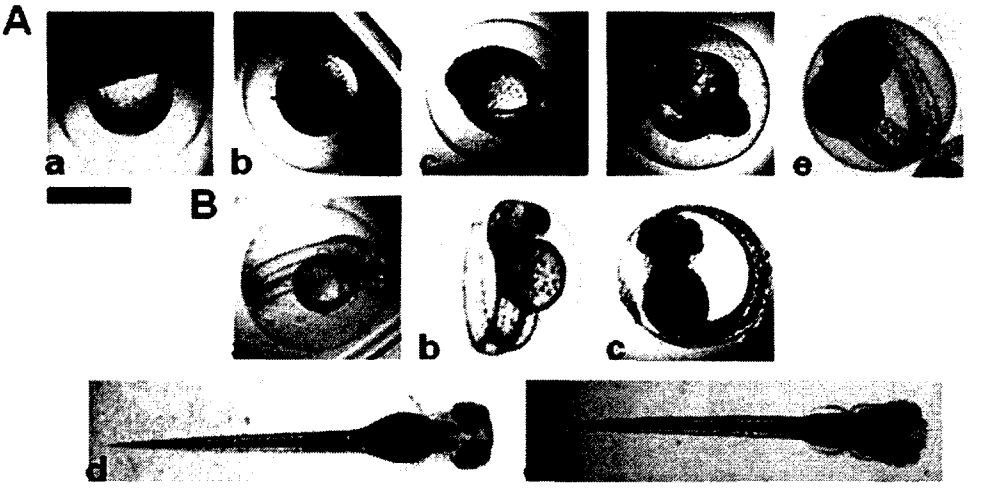

Figure 15. Normally developed zebrafish at stages I – V at the time of acute treatment and observations after acute treatment.

(A) Representative optical images of normally developed zebrafish at the time of acute treatment for stage I – V, (a) 2 hpf (cleavage stage); (b) 6 hpf (early gastrula stage); (c) 12 hpf (early segmentation stage); (d) 21 hpf (late segmentation stage) and (e) 48 hpf (hatching stage). (B) Representative optical images of normally developed zebrafish observations after acute treatment for stages I – IV, (a) 24 hpf (late segmentation stage); (b) 48 hpf (hatching stage); (c) 72 hpf (pharyngula stage); (d) 96 hpf larvae and (e) 120 hpf fully developed larvae. Note that observations for stage V began at (c-e). Scale bar = 500 μm.

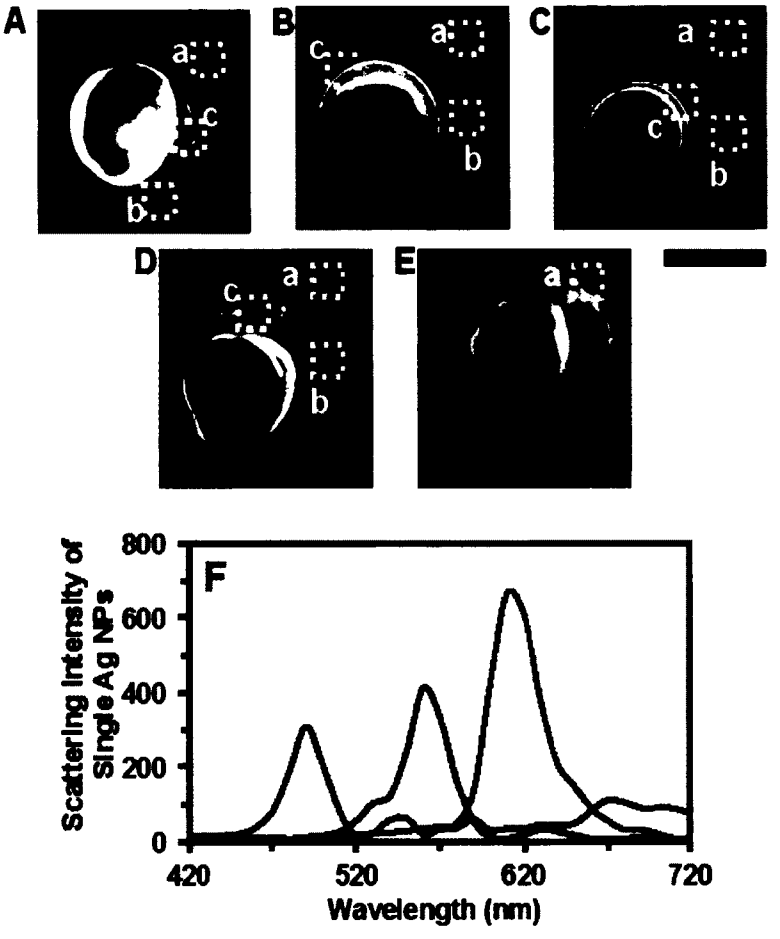

Figure 16. Characterization of Ag NPs in zebrafish embryos using DFOMS. Representative optical images of (A) stage I (cleavage stage) embryo, (B) stage II (early gastrula stage) embryo, (C) stage III (early segmentation stage) embryo, (D) stage IV (late segmentation stage) embryo, and (E) stage V (hatching stage) larvae. Areas where single Ag NPs were characterized, in the (a) extra-surface of the chorion layers (CL); (b) in the chorion space (CS) and (c) in the inner mass of the embryo (IME), as indicated by the squares. Note that only (a) was characterized in stage V due to the movement of the zebrafish larvae at this stage. Scale bar = 500 μm. (F) Representative LSPR spectra of single Ag NPs observed in the CL showing multiple colors (blue, green, and red) are present, with peak wavelengths (λ_{max}) at 490 nm (blue) (FWHM = 33 nm), 560 nm (green) (FWHM = 34 nm), and 610 nm (red) (FWHM = 40 nm).

of Ag NPs at each different stage of embryonic development and determined that NPs entered the chorion at each stage regardless of the stage of development. Single Ag NPs found in the embryonic chorion to be characterized were brought into focus and the LSPR spectra were determined after suitable background subtraction. Spectra of control embryos were measured in an identical manner to ensure that the optical property of the embryonic tissue doesn't overlap with that of the Ag NPs. A representative result of LSPR spectra is shown in Figure 16F.

We employed the concept of 2D mean-square-displacement (MSD) and diffusion models (e.g., directed, simple and stationary Brownian diffusion)[26, 27] to investigate the diffusion trajectory of single NPs in each embryonic stage of development following the entry into embryos and inside embryos. To follow the diffusion of single NPs inside different stage embryos in real-time, we used real-time square-displacement (RTSD) (diffusion distance at a given time interval), instead of average (mean) of square-displacement over time, because the diffusion coefficient could vary as single NPs diffuse in embryos. Doing this allowed the probing of diffusion of single NPs and viscosity of different areas of the embryonic fluid environment, such as the chorionic space or the inner mass of the embryo in each different stage embryo in real-time. The diffusion coefficient (D) of single NPs in simple Brownian motion is calculated by dividing the slope of a linear plot of real-time square-displacement versus time by 4 (Note: $RTSD = 4D\Delta t$).

Representative optical images and diffusion trajectories of single Ag NPs trapped inside the pores of the chorion layers (CL) at the interface with egg-water and analysis of these diffusion trajectories using the real-time square-displacement method for each developmental stage are shown in Figure 17. The results illustrate that as single Ag NPs make several attempts to enter the CL, their trajectory and diffusion patterns are constrained (Fig. 17, A-E, (a-c)), suggesting that the NPs dock into the chorion pores, which halts their normal trajectory and diffusion patterns. The representative D values of the green Ag

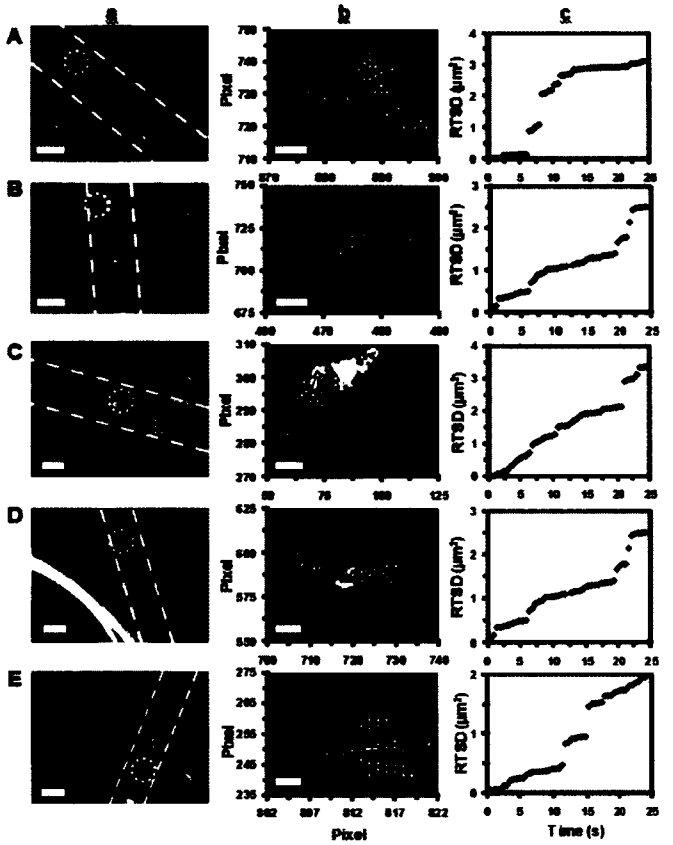

Figure 17. Characterization of transport and diffusion trajectories of single Ag NPs in acute treatment stages I - V at the chorion layers (CL).

Representative (a) optical images of the interface of the chorion with egg-water, where single green Ag NPs (dashed circles) from outside chorion (OC) through the pores (outlined in (C) by the dashed square) of the CL, represented by the dashed lines, were monitored for the (b) diffusion trajectory and (c) real-time square displacement (RTSD) as a function of time for stages I – V. (A) Stage I exhibits constrained motion with $D = 2.65 \times 10^{-10} \pm 2.43 \times 10^{-10} cm^2\ s^{-1}$. Scale bar = 10 μm (a) and 400 nm (b). (B) Stage II shows constrained motion with $D = 2.26 \times 10^{-10} \pm 2.08 \times 10^{-10} cm^2\ s^{-1}$. Scale bar = 10 μm (a) and 400 nm (b). (C) Stage III illustrates constrained motion with $D = 7.54 \times 10^{-10} \pm 9.77 \times 10^{-10} cm^2\ s^{-1}$. Scale bar = 10 μm (a) and 800 nm (b). (D) Stage IV displays constrained motion $D = 8.12 \times 10^{-10} \pm 0.12 \times 10^{-10}\ cm^2\ s^{-1}$. Scale bar = 10 μm (a) and 400 nm (b). (E) Stage V demonstrates constrained motion with $D = 6.04 \times 10^{-10} \pm 8.02 \times 10^{-10} cm^2\ s^{-1}$. Scale bar = 10 μm (a) and 200 nm (b).

NPs for stages I through V were (2.65 ± 2.43) x 10^{-10}, (2.26 ± 2.08) x 10^{-10}, (7.54 ± 9.77) x 10^{-10}, (8.12 ± 0.12) x 10^{-10}, and (6.04 ± 8.02) x 10^{-10} cm^2 s^{-1}, respectively. The data for stages I through V all showed similar findings and this was in accordance with our previous recorded diffusion data.[11] We were able to track the entry of individual nanoparticles into the chorion of each developmental stage.

Once the Ag NPs are inside the chorionic space (in-between the CL or inner mass of the embryo (IME)) we characterized the D values of the NPs (Fig. 18) to determine the possible variation of D values due to the different viscosities of the embryonic environment during that time of development. The D values are inversely proportional to their radius, as described by the Stoke-Einstein equation, $D = kT/(6\pi\eta a)$, showing that the D depends on the viscosity of environment (η) and the radius (a) of solute (NP).[28, 29] In our previous studies, the diffusion coefficients of the given color (radius) of NPs in embryos were studied and compared with those in egg-water, showing that the various diffusion coefficients observed in three different parts of embryos were due to the viscosity of embryonic environment. Simple diffusion (not active transport) with slower diffusion rates than those in egg-water, demonstrate that single Ag NPs diffuse into the chorionic space via passive diffusion and that the viscosity of the chorionic space is higher than that of egg-water.[11, 13]

There was a difference in the characterized trajectories and D values dependent on the stage of development in the chorionic space (Fig. 18, A-D, (a-c)). Stage I through IV, characterization of single NPs in the chorion space, all displayed simple Brownian diffusion with representative D values of green NPs of (3.35 ± 1.15) x 10^{-9}, (7.29 ± 5.36) x 10^{-10}, (3.31 ± 2.05) x 10^{-10} and (9.82 ± 3.96) x $10^{-10}$$cm^2$ s^{-1}, respectively. Stage I D values were higher than the D values of stage II through IV suggesting that the environmental viscosity in stages I is lower. This is consistent with literature in that during this period of development (stage I) gene expression has been found to be lower as compared to stages II -

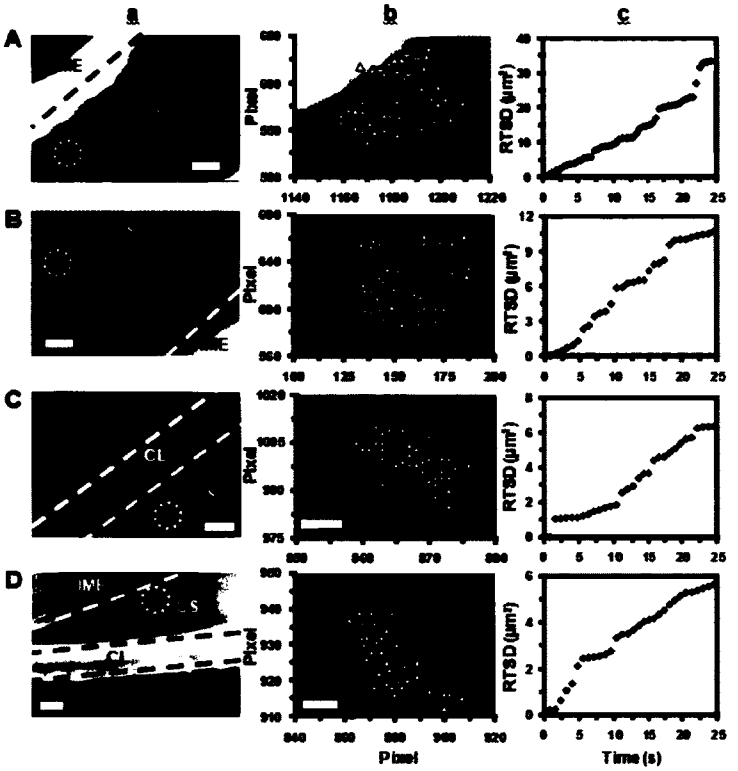

Figure 18. Characterization of transport and diffusion trajectories of single Ag NPs in the chorion space (CS) in acute treatment stages I – V.

Representative (a) optical images of the CS, where single green Ag NPs (dashed circles) in-between the CL and the inner mass of the embryo (IME), represented by the dashed lines were monitored for the (b) diffusion trajectory and (c) real-time square displacement (RTSD) as a function of time for stages I - V. (A) Stage I exhibits simple Brownian motion with $D = 3.35 \times 10^{-9} \pm 1.15 \times 10^{-9} cm^2 s^{-1}$. Scale bar = 10 μm (a) and 1 μm (b). (B) Stage II shows simple Brownian motion with $D = 7.29 \times 10^{-10} \pm 5.36 \times 10^{-10} cm^2 s^{-1}$. Scale bar = 10 μm (a) and 1 μm (b). (C) Stage III illustrates simple Brownian motion with $D = 3.31 \times 10^{-10} \pm 2.05 \times 10^{-10} cm^2 s^{-1}$. Scale bar = 10 μm (a) and 400 nm (b). (D) Stage IV displays simple Brownian motion with $D = 9.82 \times 10^{-10} \pm 3.96 \times 10^{-10} cm^2 s^{-1}$. Scale bar = 10 μm (a) and 1 μm (b).

IV.[56] The lower expression of genes at this time would indicate that there are fewer proteins being translated at this time and the biomolecule content in the chorion space would be less resulting in a less viscous environment, which is consistent with a higher diffusing rate observed in stage I. In stages II and IV the diffusion appears restricted and the D values are lower suggesting that the viscosities of the chorion space of the embryonic environment are more concentrated during these stages of development. The increased viscosity correlates with these periods of development because during stage II many genes are starting to be expressed and in stage III and IV many more genes are being expressed during the segmentation period to aid in the development of the organ systems and require many signaling pathways and biomolecules to complete proper development.[56] The trajectories in the chorionic space (Fig. 18, A-D, (b)) also varied with each stage demonstrating that there are different viscosities and fluid flow dynamics of the changing embryonic environment during development. We were not able to accurately characterize diffusion and trajectories of the NPs in the chorionic space for the stage V embryos due to the movement of the live embryo.

We also characterized the diffusion coefficients of the NPs at the surface of the inner mass of the embryo (IME). Representative diffusion trajectories of single Ag NPs at the surface of the IME and analysis of these diffusion trajectories using the real-time square-displacement method for each developmental stage are shown in Figure 19, A-D (a, b).. The results illustrate that as single Ag NPs make several attempts to enter the embryonic mass their diffusion patterns are confined (Fig. 19, A-D (c)), suggesting that the NPs come in contact with the developing embryonic mass, which arrests their normal diffusion. The representative D values of green NPs for stages I through IV were $(3.07 \pm 0.22) \times 10^{-10}$, $(9.73 \pm 7.19) \times 10^{-10}$, $(9.91 \pm 8.35) \times 10^{-10}$ and $(6.79 \pm 3.27) \times 10^{-10}$ cm^2 s^{-1}, respectively. Again, we were not able to accurately characterize diffusion and trajectories of the NPs in the inner embryonic mass for the stage V embryos due to the movement of the live embryo.

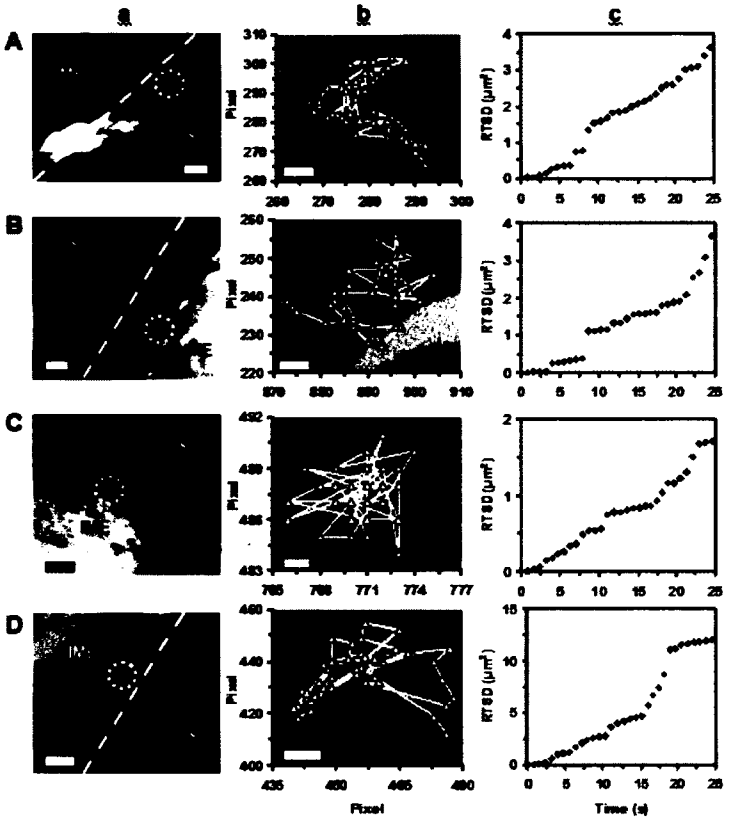

Figure 19. Characterization of transport and diffusion trajectories of single Ag NPs in the inner mass of the embryo (IME) in acute stages I – V.

Representative (a) optical images of the IME, represented by the dashed lines where single green Ag NPs (dashed circles), were monitored for the (b) diffusion trajectory and (c) real-time square displacement (RTSD) as a function of time for stages I - V. (A) Stage I exhibits constrained motion with $D = 3.07 \times 10^{-10} \pm 0.22 \times 10^{-10} cm^2\ s^{-1}$. Scale bar = 10 μm (a) and 400 nm (b). (B) Stage II shows constrained motion with $D = 9.73 \times 10^{-10} \pm 7.19 \times 10^{-10} cm^2\ s^{-1}$. Scale bar = 10 μm (a) and 400 nm (b). (C) Stage III illustrates constrained motion with $D = 9.91 \times 10^{-10} \pm 8.35 \times 10^{-10} cm^2\ s^{-1}$. Scale bar = 10 μm (a) and 100 nm (b). (D) Stage IV displays constrained motion with $D = 6.79 \times 10^{-10} \pm 3.27 \times 10^{-10}\ cm^2\ s^{-1}$. Scale bar = 10 μm (a) and 600 nm (b).

Concentration-dependent developmental stage biocompatibility

D. rerio embryos exposed to sub-lethal concentrations of Ag NPs at select stages revealed that NPs induced death, as well as a variety of morphological defects and the number of different types of defects and the severity of each increased with increasing concentration of NPs. Stage I resulted in an increasing percentage of deformities in Ag NP treated embryos as the concentration was increased (Fig. 20A) with a critical concentration at 0.5 nM. In stage I even exposure to the lowest concentration produced abnormalities. At higher concentrations, an increasing percentage of Ag NP treated embryos died; correspondingly, recovery of viable abnormalities also declined. At the highest tested concentration, a majority of embryonic death was observed (Fig. 20A) with the critical concentration at 0.06 nM.

Embryos treated in stage II had high rate of death but did not show any signs of deformities (Fig. 20B) correlating with increasing NP concentration having a critical concentration at 0.2 nM. This stage appeared sensitive to the treatment with NPs causing death of the embryos. This was specific for this stage of development and most likely due to that during this stage of development the embryos are undergoing vast cellular movements and establishment of the early organ systems.[53, 54] During this period the germ layers of the embryos are also being established, the ectoderm, the mesoderm, and the endoderm, which will become all parts of the developed organism.[53, 54] Stage II of development is a time when the onset of gene expression is starting and combined with our findings of restricted diffusion of the nanoparticles in the chorion space, the nanoparticles are interacting with the increased proteins being expressed in the chorion space.[56] This could affect the pathways during development causing an increase in death at this stage, which is directly related to the increase in the NP concentration.

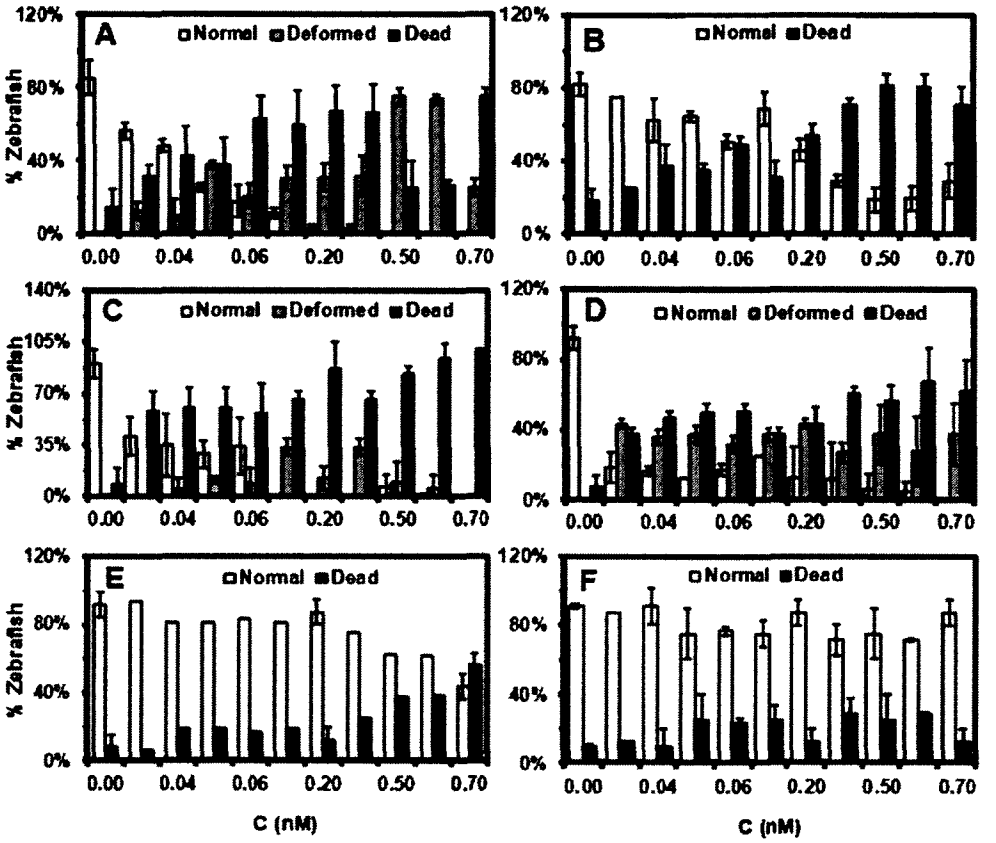

Figure 20. Histograms displaying the distribution of effects resulting from treatment with Ag NPs and the supernatant on zebrafish.

(A) Normally developed, deformed, and dead zebrafish *vs.* concentration of Ag NPs in stage I. (B) Normally developed and dead zebrafish *vs.* concentration of Ag NPs in stage II. Note: no deformities were observed in stage II. (C) Normally developed, deformed, and dead zebrafish *vs.* concentration of Ag NPs in stage III. (D) Normally developed, deformed, and dead zebrafish *vs.* concentration of Ag NPs in stage IV. (E) Normally developed and dead zebrafish *vs.* concentration of Ag NPs for stage V. Note: no deformities were observed in stage V. (F) Normally developed and dead zebrafish *vs.* concentration of supernatant removed from Ag NP washing. Note: no deformities were observed in supernatant treatment.

Stage III treatment resulted in an increasing percentage of deformities as the concentration was increased (Fig. 20C) with a critical concentration at 0.07 nM. The critical concentration is the minimum concentration needed to affect at least 50% of the normal zebrafish population. Exposure to the lowest concentration in stage III produced no abnormalities. At higher concentrations, an increasing percentage of Ag NP treated embryos died and equally the recovery of viable abnormalities for stage III also declined. At the highest tested concentration, a total embryonic death was observed (Fig. 20C) with the critical concentration at 0.02 nM.

Stage IV treated embryos resulted in increased deformities with the lowest concentration and remained consistently constant throughout Ag NP concentration rises (Fig. 20D). The critical concentration was determined to be 0.02 nM. In stage IV even exposure to the lowest concentration produced abnormalities. At higher concentrations, a small increasing percentage of Ag NP treated embryos died. At the higher tested concentrations in stage IV, a majority of embryonic death was observed (Fig. 20D) with the critical concentration at 0.02 nM.

Stage V resulted in no morphological defects and only a slight increase in death rate (Fig. 20E) with a critical concentration at 0.07 nM. This is possibly due to that during stage V, the embryo is in the hatching stage and finishing its development.[53] Untreated control embryos for stages I through V (0.00 nM) produced no abnormal embryos and embryo viability was within normal limits (Fig. 20A-F). Control embryos exposed to (nanoparticle-free) supernatant from the NP washing process showed minimal levels of toxicity at all tested concentrations (Fig. 20F).

The effective dose for our acute studies was determined from our previous chronic studies.[11] We treated stage I through V embryos acutely with various concentrations of Ag NPs (0 – 0.7 nM). Embryos were carefully monitored post treatment at 24, 48, 72, 96, and 120 hpf (Fig. 15B). We examined the defects associated with treatment of developing embryos with Ag NPs at each treated embryo developmental stage. Many morphological defects were observed in the

developing zebrafish, including abnormal finfold and tail development, cardiac malformation, yolk sac edema and acephaly as shown in Figure 21. Stages I, III, and IV all had defects whereas; stage II had high rate of death but did not show any signs of deformities. Stage V did not show any signs of abnormalities and death only slightly increased. The shared abnormality among stages I, III, and IV treated embryos was finfold abnormalities, typically affecting the median finfold region (Fig. 21A - C (a)). In normally developing embryos, the median finfold is a clear, thin membrane around the entire trunk region containing unsegmented fin rays. In treated embryos at stage I, III, and IV, the tissue structure of the finfold was disorganized and in the more severe cases, the shapes of the finfold and the developing fin rays were altered. Treated embryos from stages I, III, and IV also displayed as the second shared defect, an abnormal tail (spinal cord) flexure phenotype (Fig. 21A - C (b)). This defect was often accompanied by tissue abnormalities of the finfold. In normal developing embryos, the notochord and spinal cord develop straight to the posterior-most tip of the tail. In the treated embryos for these stages however, the tail region was flexed to some extent. In the more severely flexed embryos, the flexure was extreme and the overall length of the tail was reduced (Fig. 21A (b)). The tail flexure defect also increased in severity with increasing NP concentration.

The types and majority of defects observed differed according to the developmental stage at treatment. Embryos treated with the higher Ag NP concentrations (0.06 and 0.6 nM) in stage I presented with acephaly, or absence of a developed head (Fig 21A (e, f)). The embryos had a small amount of tissue where the head would normally develop. The tissue was not a fully formed head but rather an irregular formed mass of tissue. The severe cases of acephaly recovered from the treatment were only found to occur in stage I of development and not in stages III and IV. This is most likely due to the specific time of development because in stage I of development, the cells are still in the process of cleaving to lay out the map to form the head and caudal regions of the developing organism. If cells do not divide properly in the head or tail region of the body axis, it will not fully develop. Previous studies have demonstrated that

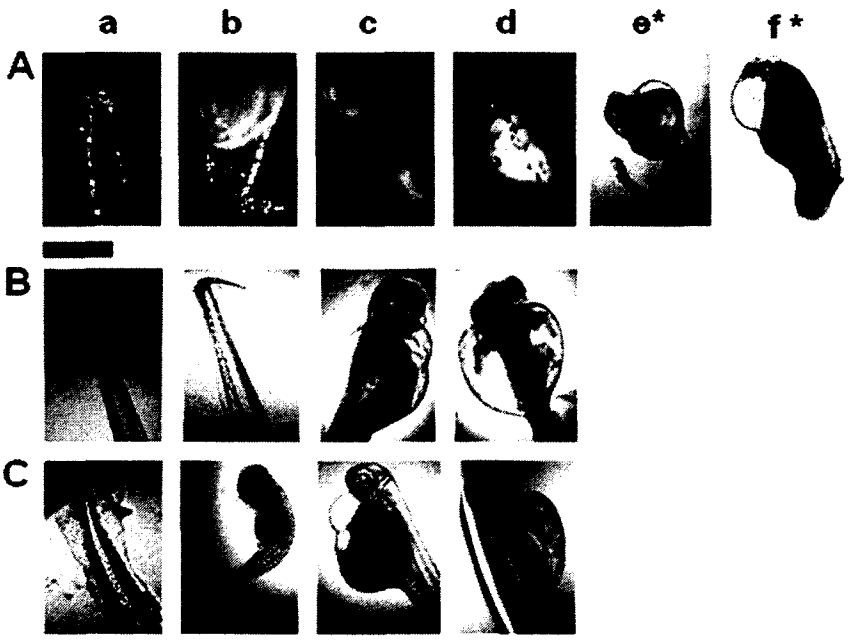

*** Most severe and rare deformities.**

Figure 21. Representative optical images of deformities observed in stages I, III, and IV after acute treatment with Ag NPs.

(A) Stage I deformed zebrafish displaying (a) finfold abnormality; (b) tail/spinal cord flexure; (c) cardiac malformation; (d) yolk sac edema and (e, f) acephaly. (B) Stage III deformed zebrafish displaying (a) finfold abnormality; (b) tail/spinal cord flexure; (c) cardiac malformation and (d) yolk sac edema. (C) Stage IV deformed zebrafish displaying (a) finfold abnormality; (b) tail/spinal cord flexure; (c) cardiac malformation and (d) yolk sac edema. Scale bar = 500 μm.

inhibiting p38 kinase activity resulted in blastomeres on one side of the embryonic mass not to divide.[57] In stage I treated embryos, the deformity type that was observed the most was found to be finfold abnormality (Fig 21A (a)). Treated embryos from stage I displayed an abnormal tail flexure phenotype, cardiac malformation, and edema, or swelling, of the yolk sac region as the second most common defect (Fig 21A (b-d)). In normally developing embryos, the yolk sac region is a bulbous area containing yolk that provides nutrients to the developing embryo and during the later developmental process, the yolk sac shrinks. In the affected treated embryos at stage I, however, the yolk sac region was swollen and enlarged. Embryos at stage I exposed to Ag NPs also displayed edema of the pericardial sac region. In contrast to normal embryos, in the stage I treated embryos; the pericardial sac region was swollen and enlarged (Fig 21A (c)). In severe cases, the pericardial sac was extremely large and the cardiac ventricle was decreased in size. Finally, a minority of treated embryos for stage I displayed the acephaly defect at high concentrations (Fig 21A (e, f)).

Embryos treated in stage III presented with no acephaly displaying that the acephaly deformity was characteristic of stage I treatment only. In treated embryos at stage III, the most common types of deformities observed were finfold abnormality, abnormal tail flexure phenotype, cardiac malformation, and edema, or swelling, of the yolk sac region (Fig. 21B (a-d)). The findings of tail deformity correlates with stage III of development because this is when embryos begin somitogenesis and notochord formation, which is important for proper development of the axial skeleton, the vertebrate spinal column, and the skeletal muscle.[55] Embryos at stage III exposed to Ag NPs also displayed edema of the pericardial sac region. In contrast to normal embryos, in the stage III treated embryos; the pericardial sac region was swollen and enlarged (Fig. 21B (c)). At the highest doses, the pericardial sac was extremely large and the cardiac ventricle was decreased in size.

Embryos treated in stage IV presented with no acephaly and the most common type of deformity was not finfold abnormality, as in stages I and III, but

was observed to be cardiac malformation (Fig. 21C (c)). This is most likely due the stage of development during treatment with the NPs, because during stage IV of development, the heart is being formed and is preparing for its first contraction.[53] A majority of embryos at stage IV exposed to Ag NPs displayed edema of the pericardial sac region. At the highest doses, the pericardial sac was extremely large and the cardiac ventricle was decreased in size (Fig. 21C (c)). Treated embryos from stage IV also displayed as the second most common defects, an abnormal finfold development, tail flexure phenotype, and edema, or swelling, of the yolk sac region similar to those findings for stages I and III treatment (Fig. 21C (a, b, d)).

Finfold abnormalities accounted for majority of recovered events at stages I and III (Fig. 22A, B). At higher doses for stages I and III, an increasing percentage of events (but still a minority) included cardiac malformation, yolk sac edema, and tail flexure deformities (Fig. 22A, B). Cardiac malformation, at 44.1%, accounted for majority of recovered events at stage IV (Fig. 22C). At higher doses for stage IV, an increasing percentage of yolk sac edema occurred and other minority events included finfold abnormality and tail flexure deformities (Fig. 22C).

Possible reasons for the high dependence of type and severity of defects on the stage of development and concentration of NPs could be due to the following: (i) The NPs enter inside the chorion space of the embryo during the specific stage of development and affect the specific proteins, signaling, and developmental pathways during that period of development. (ii) An increase in number of NPs inside the chorion space of the embryo during the specific stage of development increases the altering effects of the protein, signaling, and developmental pathways during development increasing severity of the deformity observed or death.

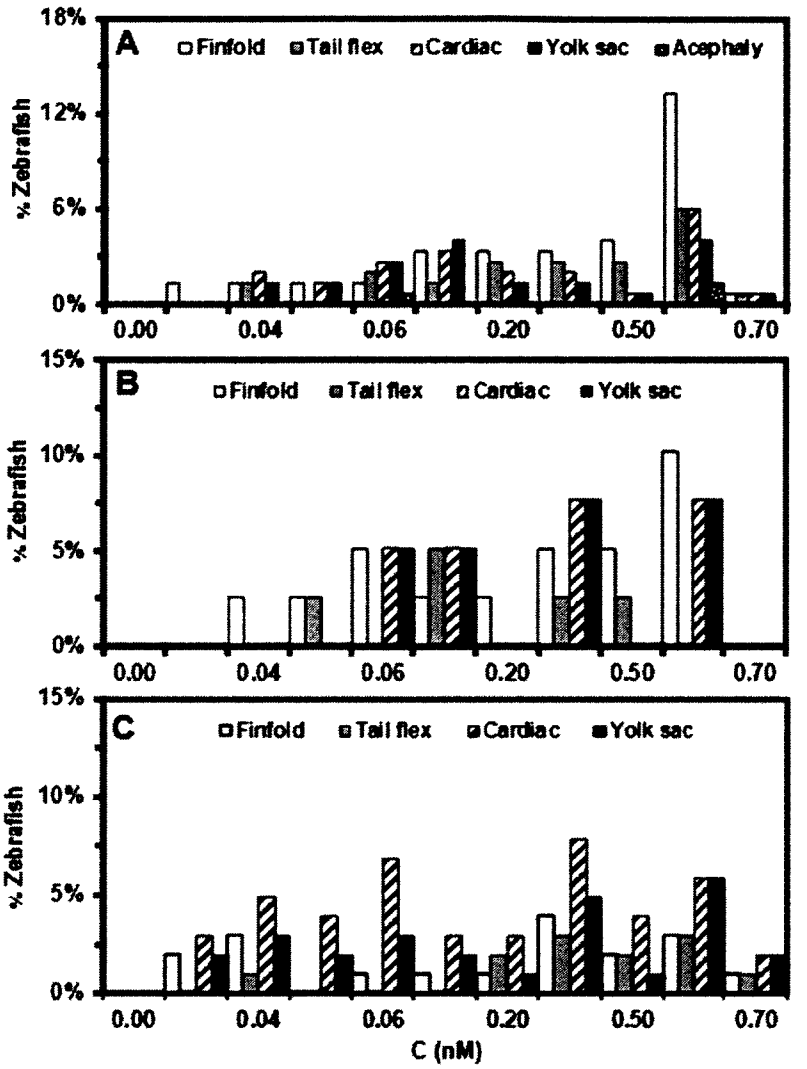

Figure 22. Histograms of the types of deformities *vs.* the percentage of zebrafish.

After acute treatment at each concentration of Ag NPs, five types of deformities in (A) stage I and four types of deformities in (B) stage III and in (C) stage IV were observed.

Our results describe a range of developmental defects and death following exposure of developing zebrafish embryos to nanomolar concentrations of Ag NPs at particular embryonic stages of development. Specific developmental pathways of embryonic development are still unknown, such as, differentiation into specialized tissues and organs, specifically how cells communicate with each other, how they become committed to a certain fate, and how they formulate a pattern to become a structure.[54, 56] Stage dependent developmental responses to Ag NPs, shown here, in a dose dependent manner, demonstrates the possibility of being able to pick specific developmental pathways to create particular phenotypes and as potential developmental therapeutic agents to treat specific disorders and generate specific developmental mutation in zebrafish, by alteration of the time of application of the NPs.

SUMMARY

In summary, we examined the transport and diffusion of single Ag NPs *in vivo* at specific stages of development and the defects associated with treatment at specific developmental stages. Ag NPs were observed inside embryos of every treated developmental stage, demonstrating that Ag NPs can transport independent of the stage of the developing embryos and can be administered without outside influence, such as microinjection. Ag NPs can be used in developmental stage treatment *in vivo* assays for study of nanomaterials and their role in developmental biology. The transport and diffusion of NPs in the chorion space demonstrated that the viscosity of the developing embryonic environment could be documented at each stage of development using single NP optics. An increase in embryonic environmental viscosity and NP concentration correlated to an increase in death, which demonstrated NP interaction with transcribed biomolecules in the chorion space during development. Many morphological defects were observed in the developing embryo, including acephaly, yolk sac edema, abnormal finfold and tail development, and cardiac

malformations at each stage of development, corresponding to the stage of treatment. In general, the number of different types of defects and the severity of each varied with the stage of treatment and increased with increasing dose of NPs demonstrating the possibility of selectively targeting specific embryonic developmental pathways by altering the stage of development and dose of NPs for developmental therapeutic studies. The investigation of transport, diffusion, and biocompatibility of nanomaterials in specific stages of development of embryos at single NP level can offer new knowledge about the developmental processes and environment, and provide new insights into the mechanics of the developing embryo as well as aid in the finding for functional nano-developmental treatments for various disorders in early development.

METHODS

Synthesis and Characterization of Ag NPs

We synthesized Ag NPs (13.1 ± 2.5 nm), as we described previously.[11, 13, 58] The design and construction of our DFOMS for imaging of single Ag NPs in solution and in single embryos has been described in detail in our previous studies.[11, 13, 15, 58-64]

Treatment and monitoring of Zebrafish Embryos

Wildtype (WT) adult zebrafish (Aquatic Ecosystems) were maintained, bred, and collected, as described previously.[11, 59] 16 embryos were tested per concentration, per stage of development for 2 hours in NPs; each experiment was repeated 3 times, totaling 48 embryos analyzed per concentration, per stage of development. Each developmental stage of embryos in the wells was directly imaged as described previously.

Study and Characterization of Transport and Biocompatibility of NPs

Stage II through V living embryos that had been incubated with 0.2 nM NPs for a given time (0-2 hours) were carefully rinsed with DI water to remove external NPs, placed in a self-made microwell containing DI water, and

immediately imaged to investigate the transport of NPs into embryos or untreated embryos were placed in a self-made microwell containing DI water to image the diffusion and transport of NPs inside the embryos in real-time using our DFOMS by adding the Ag NPs directly to the microwell.

To study the dose-dependent effects of NPs on embryonic development, a dilution series of washed Ag NP solutions (0, 0.02, 0.04, 0.05, 0.06, 0.07, 0.18, 0.35, 0.53, 0.62, and 0.66 nM) were incubated acutely with 5 stages of embryos in egg-water for 2h. Each experiment was carried out at least 3 times and total number of embryos at 48 was studied for each individual concentration to gain representative statistics. NP concentrations were calculated as described previously.[11] Embryos in egg-water in the absence of NPs and in the presence of supernatant were placed in two rows of the 24-well plates as control experiments to probe the effects of possible trace chemicals from NP synthesis. The embryos in the 24-well plates were incubated at 28.5°C, and directly observed at room temperature using an inverted Zeiss Axiovert microscope equipped with a digital color camera at 24, 48, 72, 96, and 120 hpf.

Data Analysis and Statistics

A minimum of 100 Ag NPs was imaged and characterized for each measurement of their sizes and stability in egg-water using HRTEM and DFOMS. A minimum of 300 NPs in total was studied for each sample via three repeated measurements. For real-time imaging of diffusion of single NPs into and in embryos over time, a minimum of 16 embryos was studied for each given concentration. For study of dose-dependent effects of NPs on embryonic development, a total number of 48 embryos were studied for each NP concentration and each control experiment over 120 hpf with a minimum of 12 embryos studied in each measurement.

CHAPTER IV

STUDY OF CHARGE DEPENDENT TRANSPORT, BIOCOMPATIBILITY AND TOXICITY OF 12 NM SILVER NANOPARTICLES USING ZEBRAFISH EMBRYOS

INTRODUCTION

Drug delivery using nanotechnology has become an exciting new area of interest for new innovative ways to use nanomaterials as drug delivery vehicles for both targeting and sensor of cellular changes in living systems and delivery of drugs to specific cells and tissues[30, 63, 65-69,70]. New drug delivery approaches are using nanotechnology as a type of nanomedicine to establish an earlier diagnosis and a new safer treatment option by using direct delivery methods to single cells for many diseases, including cancers[71]. With the potential for use of nanomaterials in a living system to directly target diseased ridden cells, it is important to explore the important biophysicochemical interactions the nanomaterials can have in and on living biological system. There are many different biophysicochemical factors that are important for how nanomaterials interact with a biological system. Size, shape, surface charge (zeta potential), functional groups, and ligands can all affect how a nanomaterial will behave and how it will affect the delivery or function of a drug to a target cell or diagnosis sensor system in a living *in vivo* system[72, 73, 30, 74]. To understand these interactions in more detail it is important to look at each factor and investigate how nanomaterials behave in a living *in vivo* system to anticipate potential drug delivery response. The biophysicochemical characteristics of nanoparticles can determine how biocompatible a nanoparticle will be in an *in vivo* system[72]. Surface charge has been shown to have an impact on the biocompatibility of a nanoparticle to a living system[72].

In this study we focused on how surface charge (zeta potential) influences how a single silver (Ag) nanoparticle transports and diffuses in a living zebrafish embryo system in real-time. We also examined the biocompatibility the different

surface charged Ag nanoparticles had on the zebrafish system and how it influenced the embryonic development. Interaction of surface charged nanoparticles in a biological system, especially an embryonic developing system, is an interesting area of nanotechnology research. Greater understanding of developmental biology is crucial and utilizing nanoparticle technology and understanding the biophysicochemical interactions will allow more information to explore unknown mechanisms during development.

It is not known whether Ag nanoparticles with different surface charges can enter the zebrafish embryo and what impact will they have on the developing system. Previous studies with gold nanoparticles on cells show strong correlation of surface charge and related toxicity[75, 76]. Nanoparticles have unique surface chemistry which allows them to be conjugated with biomaterial (DNA, peptide, drugs etc,) for biomedical clinical purposes so it is important to investigate surface charge transport, diffusion, and biocompatibility on a living system[77, 78].

We synthesized uniform Ag nanoparticles with three different surface charges and conducted studies for their transport and biocompatibility in developing embryos. Surface charge is important because it influences every aspect of nanoparticle function, uptake mechanisms and nanoparticle clearance. To our knowledge, there has been no significant research done to study the impact of surface charge of nanoparticles on the biocompatibility, toxicity, and the transport of these nanoparticles in an *in vivo* model system. There are however toxicity and biocompatibility studies done with other nanomaterials using cells as the model organism[79-84]. Also many studies have used nanoparticles as delivery agents in living systems[85].

RESULTS AND DISCUSSION

Synthesis and Characterization of Stability of Ag Nanoparticles

We synthesized sphere shaped Ag NPs as described previously and conjugated them with three different types of peptides, CALNNE (-), CALNNS

(~0), CALNNK (+), producing NPs with different surface charges, as demonstrated in Figure 23 enabling the study of key surface charge dependent transport, diffusion, and biocompatibility to determine their behavior *in vivo*, including morphological responses and concentration dependent morphological responses, for potential use as drug delivery systems or developmental intermediates for biomedical applications[70, 80]. We characterized the zeta-potential of our peptide Ag nanoparticles and determined the surface charge for Ag-CALNNK (+), Ag-CALNNS(~0), and Ag-CALNNE(-) to be 2.96 ± 0.19, - 5.04 ± 0.09, - 11.94 ± 0.94, respectively (Fig. 23B).

We further characterized the purified Ag NPs conjugated with CALNNK (+), CALNNS (~0), and CALNNE (-) using transmission electron microscopy (TEM) and dark field optical microscopy and spectroscopy (DFOMS) (Fig. 24 – 26). The representative TEM image and TEM distribution for Ag-CALNNK (+) NPs in Fig. 24 indicate that the majority of the NPs are spherical in shape and the average size is 11.5 ± 2.9 nm (Fig. 24A-B). The representative DFOM image shows that NPs are blue and green (Fig. 24C). The LSPR spectra of single Ag-CALNNK (+) NPs (blue and green), had peak wavelengths (λmax) at 508 nm, 554 nm and 585 nm (Fig. 24D).

For Ag-CALNNS (~0) NPs in Fig. 25 indicate that the majority of the NPs are spherical in shape and the average size is 12.3 ± 2.7 nm (Fig. 25A-B). The representative DFOM image shows that NPs are blue and green (Fig. 25C). The LSPR spectra of single Ag-CALNNS (~0) NPs (blue and green), had peak wavelengths (λmax) at 508 nm, 560 nm and 581 nm (Fig. 25D).

For Ag-CALNNE (-) NPs in Fig. 26 indicate that the majority of the NPs are spherical in shape and the average size is 11.3 ± 2.5 nm (Fig. 26A-B). The representative DFOM image shows that NPs are blue and green (Fig. 26C). The LSPR spectra of single Ag-CALNNS (~0) NPs (blue and green), had peak wavelengths (λmax) at 508 nm, 560 nm and 581 nm (Fig. 26D).

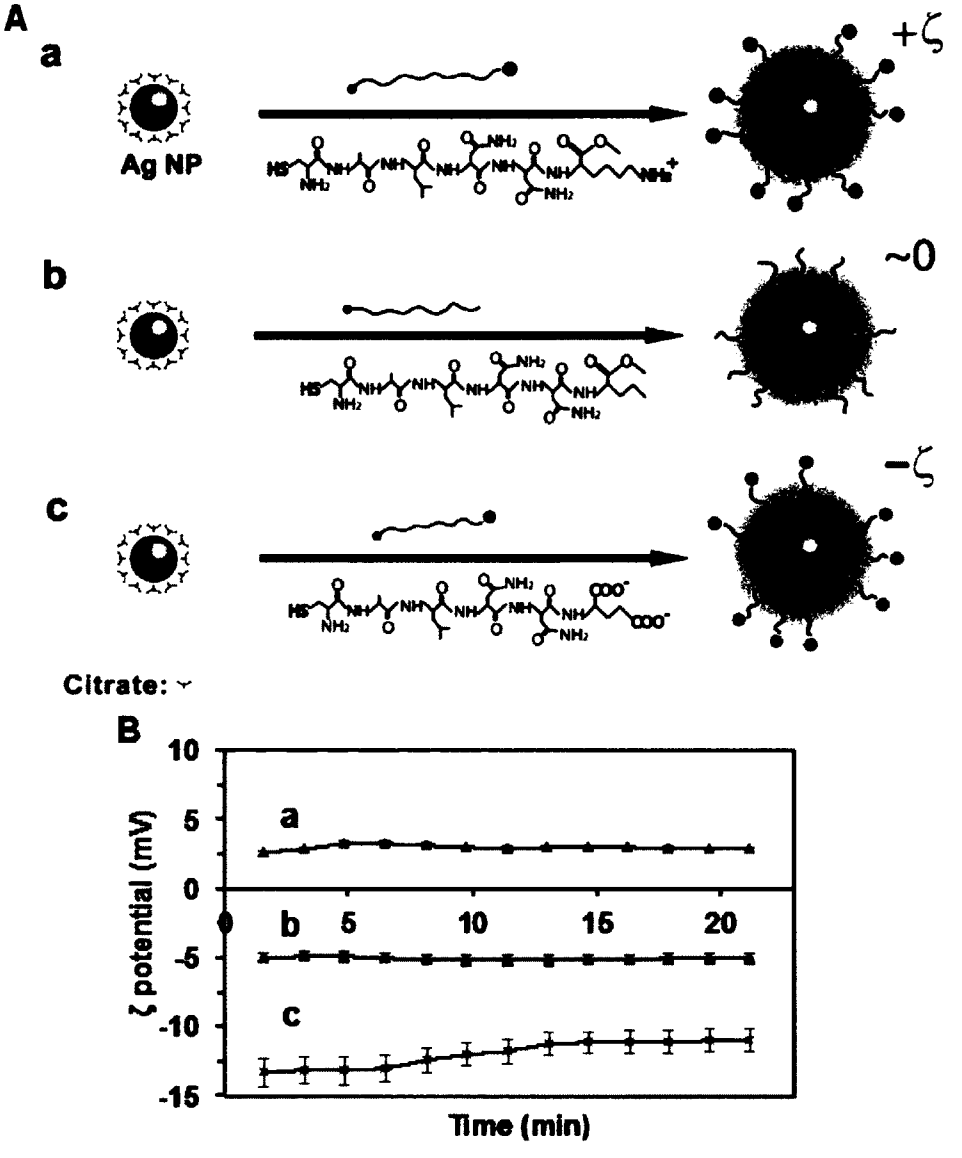

Figure 23. Illustration of synthesis and respective zeta-potentials of Ag-peptide NPs for charge dependent transport studies in developing zebrafish embryo.

(A) Illustration of (a) Ag-CALNNE (-), (b) Ag-CALNNS (~0), and (c) Ag-CALNNK (+) design. (B) Zeta-potential of (a – c) in (A) was -11.94 ± 0.94 mV, -5.04 ± 0.09 mV, and +2.96 ± 0.19 mV, respectively.

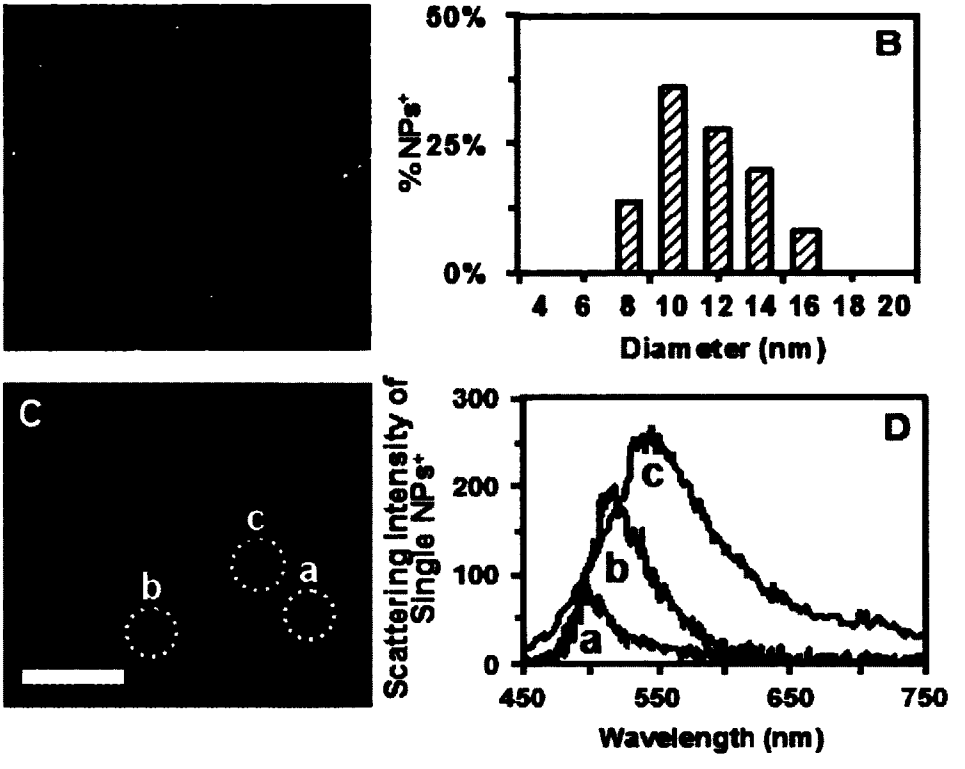

Figure 24. Characterization of size of Ag NPs and optical properties and stability of Ag-CALNNK (+) NPs.

(A) Representative HRTEM image demonstrates the size and spherical shape of single Ag NPs. Scale bar = 10 nm. (B) Histogram of size distribution of Ag NPs measured by HRTEM shows the average size to be 11.5 ± 2.9 nm. (C) Representative dark-field optical image of single Ag-CALNNK (+) NPs (a-c) shows that NPs are blue and green. Scale bar = 2 μm. (D) LSPR spectra of single Ag-CALNNK (+) NPs (blue and green), with peak wavelengths (λ_{max}) at (a) 508 nm (FWHM = 72 nm), (b) 554 nm (FWHM = 93 nm) and (c) 585nm (FWHM = 99nm).

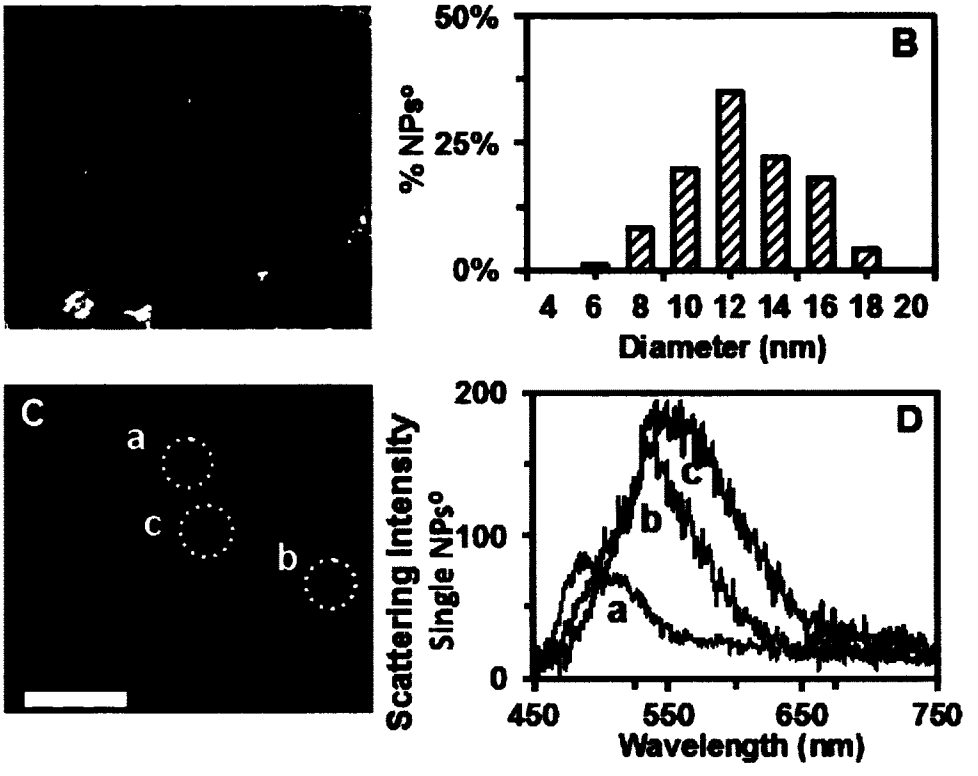

Figure 25. Characterization of size of Ag NPs and optical properties of Ag-CALNNS (~0) NPs.

(A) Representative HRTEM image demonstrates the size and spherical shape of single Ag NPs. Scale bar = 20 nm. (B) Histogram of size distribution of Ag NPs measured by HRTEM shows the average size to be 12.3 ± 2.7 nm. (C) Representative dark-field optical image of single Ag-CALNNS (~0) NPs (a-c) shows that NPs are blue and green. Scale bar = 2 μm. (D) LSPR spectra of single Ag-CALNNS (~0) NPs (blue and green), with peak wavelengths (λ_{max}) at (a) 508 nm (FWHM = 68 nm), (b) 560 nm (FWHM = 88 nm) and (c) 581 nm (FWHM = 101 nm).

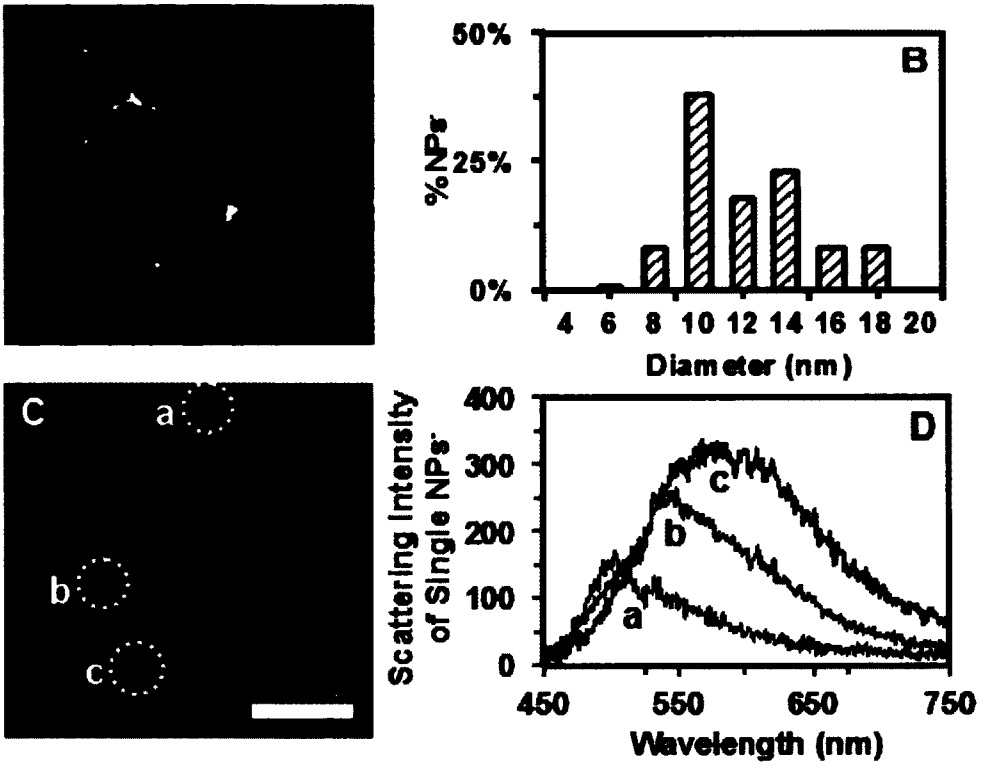

Figure 26. Characterization of size of Ag NPs and optical properties of Ag-CALNNE (-) NPs.

(A) Representative HRTEM image demonstrates the size and spherical shape of single Ag NPs. Scale bar = 20 nm. (B) Histogram of size distribution of Ag NPs measured by HRTEM shows the average size to be 11.3 ± 2.5 nm. (C) Representative dark-field optical image of single Ag-CALNNE (-) NPs (a-c) shows that NPs are blue and green. Scale bar = 2 μm. (D) LSPR spectra of single Ag-CALNNE (-) NPs (blue and green), with peak wavelengths (λ_{max}) at (a) 506 nm (FWHM = 69 nm), 555 nm (FWHM = 98 nm) and (d) 595 nm (FWHM = 111 nm).

We further characterized the stability of the purified Ag NPs conjugated with CALNNK (+), CALNNS (~0), and CALNNE (-) in egg-water embryo media (1.2 mM NaCl) for 120 hrs using DFOMS, UV-vis spectroscopy, and dynamic light scattering (DLS) (Fig. 27 – 29). The number of NPs/image (20 images) for Ag-CALNNK (+) indicate at t_0, 12h, 24h, 48h, 72h, 96h and 120h were 117 ± 3, 115 ± 3, 116 ± 2, 115 ± 3, 113 ± 4, 115 ± 4 and 112 ± 3, respectively. This indicated that the NPs remained unchanged as NPs were incubated with egg-water and were very stable over a period of 120h (Fig. 27A). The representative UV-vis absorption spectra for Ag-CALNNK (+) well-dispersed in egg-water at 28°C for (a) 0h and (b) 120h demonstrates the peak absorbance at 0.083 and peak wavelength at 406 nm and they remain unchanged for 120h (Fig. 27B). The representative size distribution of stability of Ag-CALNNK (+) NPs in egg-water media using DLS indicate at 0h the size is (a) 11.2 ± 2.5 nm and at 120h is (b) 11.3 ± 2.6 nm (Fig. 27C).

For Ag-CALNNS (~0) (Fig. 28), the number of NPs/image (20 images) indicate at t_0, 12h, 24h, 48h, 72h, 96h and 120h were 115 ± 3, 116 ± 4, 117 ± 3, 117 ± 4, 116 ± 4, 115 ± 3 and 115 ± 3, respectively. This indicated that the # of NPs remained unchanged as NPs were incubated with egg-water and were very stable over a period of 120h (Fig. 28A). The representative UV-vis absorption spectra for Ag-CALNNS (~0) well-dispersed in egg-water at 28°C for (a) 0h and (b) 120h demonstrates the peak absorbance at 0.158 and peak wavelength at 406 nm and they remain unchanged for 120h (Fig. 28B). The representative size distribution of stability of Ag-CALNNS (~0) NPs in egg-water media using DLS indicate at 0h the size is (a) 12.8 ± 2.8 nm and at 120h is (b) 13.3 ± 2.9 nm (Fig. 28C).

For Ag-CALNNE (-) (Fig. 29), the number of NPs/image (20 images) indicate at t_0, 12h, 24h, 48h, 72h, 96h and 120h were 113 ± 3, 111 ± 2, 111 ± 2, 110 ± 4, 113 ± 2, 112 ± 3 and 111 ± 3, respectively. This indicated that the # of NPs remained unchanged as NPs were incubated with egg-water and were very

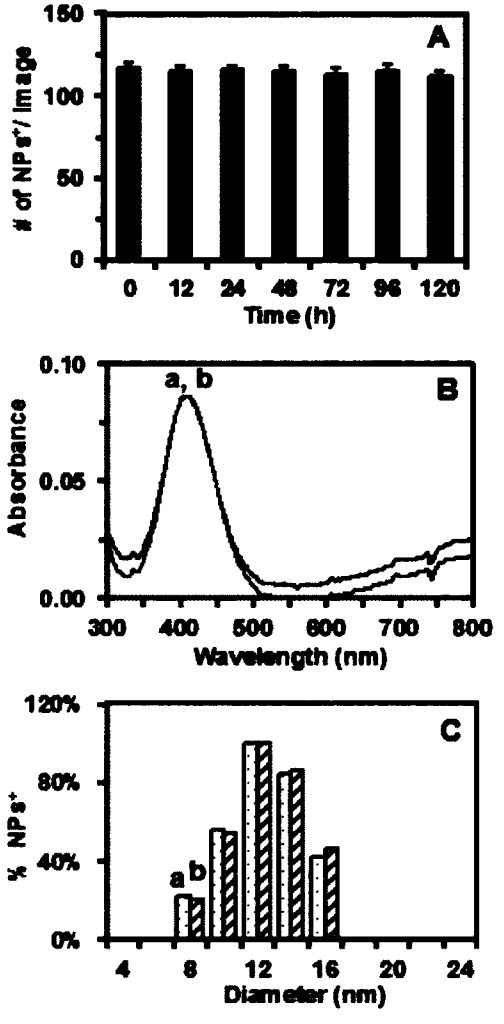

Figure 27. Characterization of stability of Ag-CALNNK (+) NPs.

(A) The number of NPs/ image (20 images) at t_0, 12 h, 24 h, 48 h, 72 h, 96 h and 120 h were 117 ± 3, 115 ± 3, 116 ± 2, 115 ± 3, 113 ± 4, 115 ± 4 and 112 ± 3. (B) Representative UV-Vis absorption spectra of Ag-CALNNK (+) NPs well-dispersed in egg-water at 28^0C for (a) 0 and (b) 120 h shows the peak absorbance at 0.083 and peak wavelength at 406 nm (FWHM = 100 nm) and they remain unchanged for 120 h.(C) Histograms of size distribution of stability of Ag-CALNNK (+) NPs in egg-water media using DLS, (a) 11.2 ± 2.5 nm at 0 h and (b) 11.3 ± 2.6 nm at 120 h.

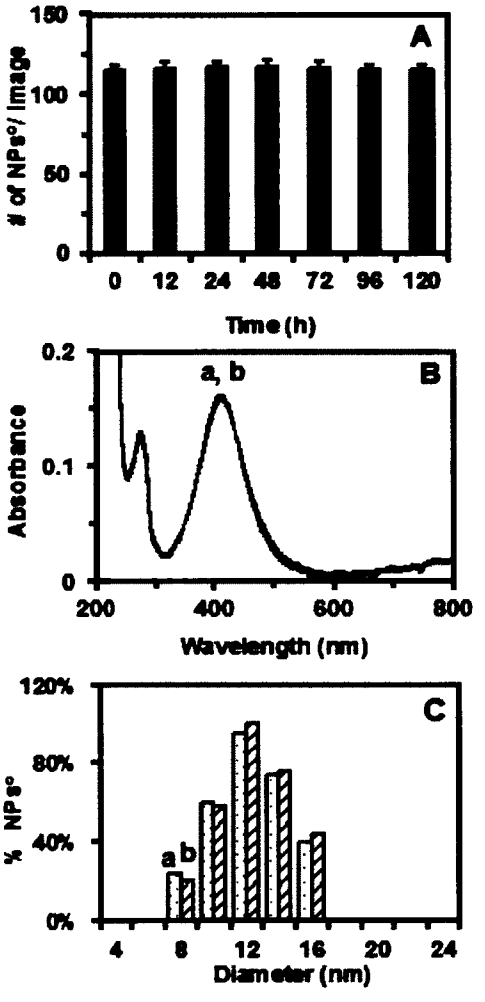

Figure 28. Characterization of stability of Ag-CALNNS (~0) NPs.

(A) The number of NPs/ image (20 images) at t_0, 12 h, 24 h, 48 h, 72 h, 96 h and 120 h were 115 ± 3, 116 ± 4, 117 ± 3, 117 ± 4, 116 ± 4, 115 ± 3 and 115 ± 3. (B) Representative UV-Vis absorption spectra of Ag-CALNNS (~0) NPs well-dispersed in egg-water at 28^0C for (a) 0 and (b) 120 h shows the peak absorbance at 0.158 and peak wavelength at 406 nm (FWHM = 101 nm) and they remain unchanged for 120 h. (C) Histograms of size distribution of stability of Ag-CALNNS (~0) NPs in egg-water media using DLS, (a) 12.8 ± 2.8 nm at 0 h and (b) 13.3 ± 2.9 nm at 120 h.

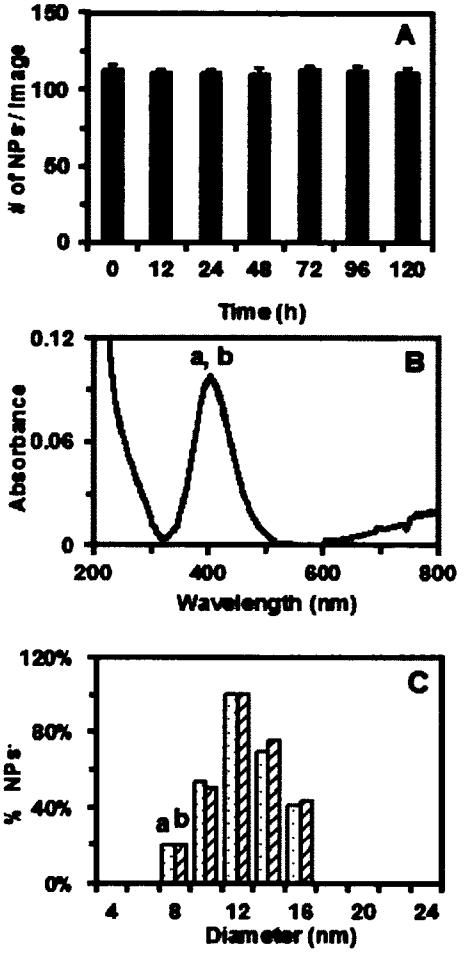

Figure 29. Characterization of stability of Ag-CALNNE (-) NPs.

(A) The number of NPs/ image (20 images) at t_0, 12 h, 24 h, 48 h, 72 h, 96 h and 120 h were 113 ± 3, 111 ± 2, 111 ± 2, 110 ± 4, 113 ± 2, 112 ± 3 and 111 ± 3. (B) Representative UV-Vis absorption spectra of Ag-CALNNE (-) NPs well-dispersed in egg-water at 28^0C for (a) 0 and (b) 120 h shows the peak absorbance at 0.091 and peak wavelength at 401 nm (FWHM = 99 nm) and they remain unchanged for 120 h. (C) Histograms of size distribution of stability of Ag-CALNNE (-) NPs in egg-water media using DLS, (a) 11.9 ± 2.8 nm at 0 h and (b) 12.3 ± 2.8 nm at 120 h.

stable over a period of 120h (Fig. 29A). The representative UV-vis absorption spectra for Ag-CALNNE (-) well-dispersed in egg-water at 28°C for (a) 0h and (b) 120h demonstrates the peak absorbance at 0.091 and peak wavelength at 401 nm and they remain unchanged for 120h (Fig. 29B). The representative size distribution of stability of Ag-CALNNE (-) NPs in egg-water media using DLS indicate at 0h the size is (a) 11.9 ± 2.8 nm and at 120h is (b) 12.3 ± 2.8 nm (Fig. 29C).

Transport, diffusion, and biocompatibility of nanoparticles *in vivo*

We treated cleavage stage (64 cell, 2.25 hours post fertilization (hpf)) zebrafish embryos without the aid of any direct intrusion and followed their development for 120 hpf. Representative optical images of normal zebrafish development at treatment and throughout treatment in the absence of nanoparticles are shown in Fig. 30.

To study the transport and diffusion of single Ag NPs in developing zebrafish embryos we incubated Ag-peptide NPs with cleavage stage embryos and were able to directly observe and characterize their transport and diffusion in real time using our DFOMS (Fig. 31). This allowed us to follow NPs and demonstrate their ability to travel through the chorion and into chorion space of the embryo and enter the inner mass of embryo regardless of the surface charge as shown in Figure 31B, a – c, respectively. Tracking NPs in the embryonic environment allowed us to probe diffusion of the different surface charged NPs, and determine the transport mechanism in an internal developing embryonic environment in real-time. For determining the transport mechanism of the nanoparticles in the embryonic environment, we used the concept of two-dimensional mean squared displacement (MSD) and different modes of diffusion such as simple, directed and random Brownian motion. These models were used to analyze diffusion trajectory of the NPs in egg-water, along the chorion interface, in the chorion space of the developing embryo and inside the developing embryonic mass. Representative diffusion trajectory and plots of single Ag-peptide NPs interacting with the pores on the chorion interface of the

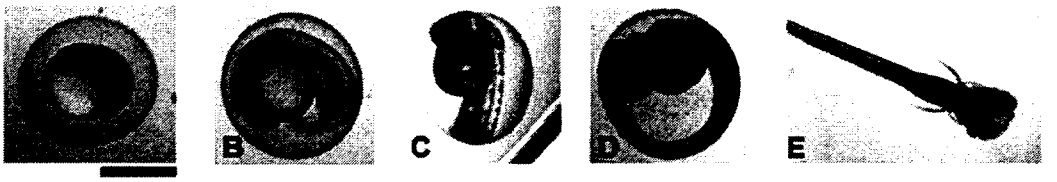

Figure 30. Representative optical images of normally developed zebrafish. (A) 0.75 – 2.25 hpf (cleavage-stage, at the time of treatment). (B) 24 hpf (late segmentation stage). (C) 48 hpf (hatching stage). (D) 72 hpf (pharyngula stage). (E) 120 hpf fully developed larvae. Scale bar = 500 μm.

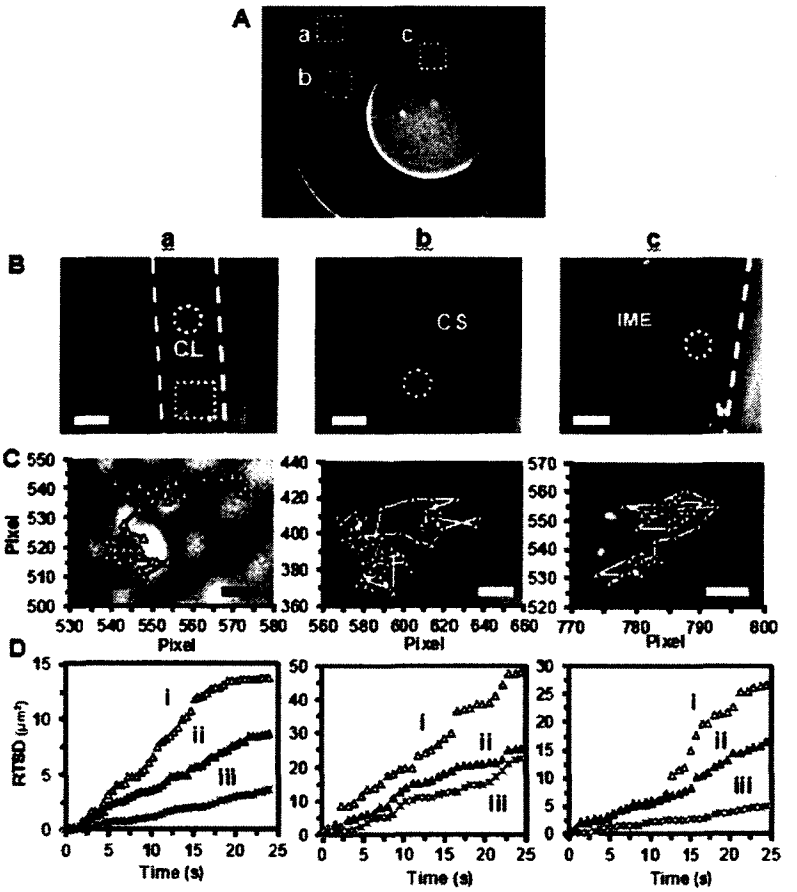

Figure 31. Characterization of transport and diffusion trajectories of single Ag-peptide NPs at the chorion layers (CL), in the chorion space (CS) and at the inner mass of the embryo (IME).

(A) Cleavage stage embryo, 2-4 hpf, demonstrating areas that were imaged (a) chorion interface, (b) chorion space, and (c) embryonic mass surface. Scale bar = 500 μm. (B) Representative optical images of Ag-CALNNK (+) NPs (circles) at the (a) CL (dashed lines), (b) inside CS and (c) at the IME. The square highlights the chorion pores in the CL. Scale bar = 10 μm. (C) Representative diffusion trajectories of Ag-CALNNK (+) NPs in the (a) CL, (b) CS and (c) IME. Scale bar = 100 nm (a), 1 μm (b) and 400 nm (c). (D) Representative plots of real-time square displacement (RTSD) as a function of time of the single green Ag-peptide NPs in the (a) CL, (b) CS and (c) IME.

developing embryo, in the chorion space and interacting with the inner embryonic mass (Fig. 31C, D) demonstrate varying diffusion coefficients (D). Due to the different embryonic environment at various locations, the diffusion coefficient can vary. Therefore we used real time square displacement (RTSD), instead of using the mean of the squared displacement allowing us to probe the diffusion of single silver in real time. The D of the single silver nanoparticles in simple Brownian motion was calculated by dividing the slope of the linear plot of the RTSD as a function of time divided by 4 (Fig. 31D).

The results of the diffusion using the previous mentioned RTSD method showed that at the chorion layers (CL), (i) Ag-CALNNK (+), (ii) Ag-CALNNS (~0) and (iii) Ag-CALNNE (-) demonstrate constrained motion with D = (6.05 ± 3.77) x 10^{-10} cm^2 s^{-1}, (2.11 ± 2.47) x 10^{-10} cm^2 s^{-1} and (1.30 ± 0.95) x 10^{-10} cm^2 s^{-1}, respectively. In the chorion space (CS), (i) Ag-CALNNK (+), (ii) Ag-CALNNS (~0) and (iii) Ag-CALNNE (-) demonstrate simple Brownian motion with D = (1.52 ± 0.92) x 10^{-9} cm^2 s^{-1}, (1.40 ± 0.26) x 10^{-9} cm^2 s^{-1} and (1.62 ± 1.53) x 10^{-9} cm^2 s^{-1}, respectively. At the inner mass of the embryo (IME), (i) Ag-CALNNK (+), (ii) Ag-CALNNS (~0) and (iii) Ag-CALNNE (-) demonstrate simple Brownian motion with D = (1.17 ± 1.48) x 10^{-9} cm^2 s^{-1}, (3.01 ± 3.81) x 10^{-9} cm^2 s^{-1} and (9.71 ± 7.18) x 10^{-10} cm^2 s^{-1}, respectively (Fig. 31D).

Resultant data of treated normal, dead, deformed and control embryos are shown in Figure 32. Treatment with Ag-CALNNE (-) resulted in an increase death. When comparing the death rate of these NPs to Ag-CALNNK (+) NPs, 80% embryos died in 0.6 nM, whereas zebrafish embryos treated at similar concentration with positive charged had higher percentage survival percentages (Fig. 32). Deformities in Ag-CALNNE (-) NP treated embryos were seen in 0.4 nM and 0.6 nM concentrations. Death and deformities in treated embryos were found to be concentration dependent as with increasing nanoparticles substantial increase in death and deformities were seen in all types of charged nanoparticles. The supernatant was used as a control to ensure that no by-

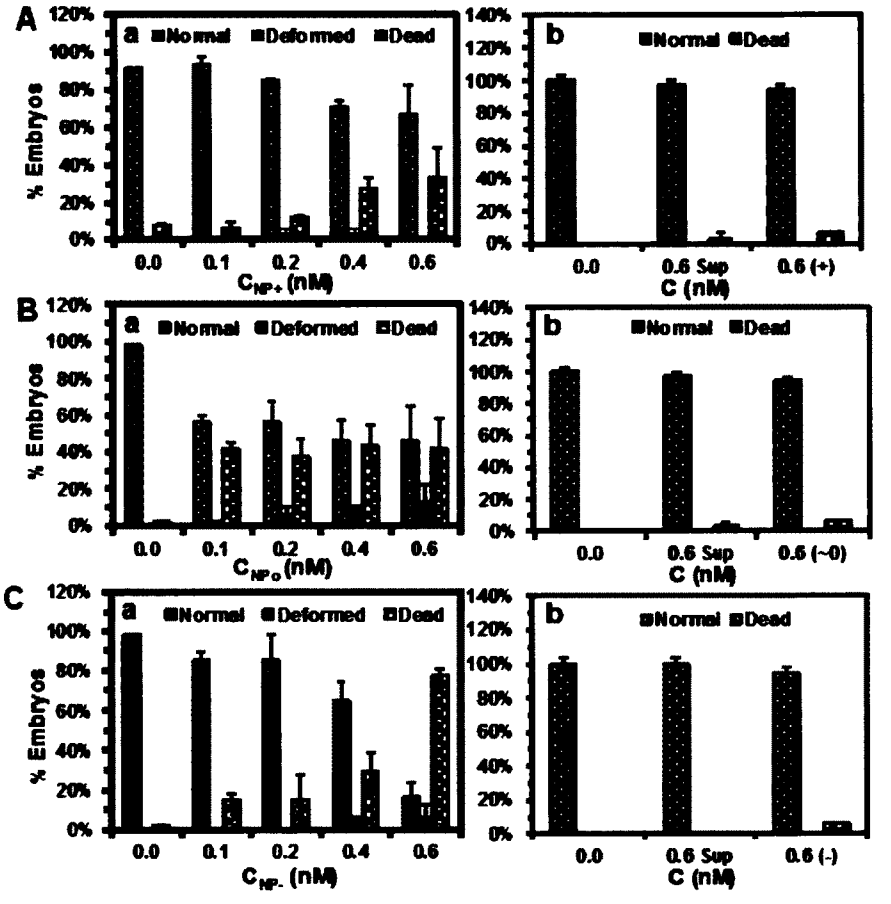

Figure 32. Histograms displaying the distribution of effects resulting from chronic treatment with Ag-peptide NPs and their supernatant on zebrafish. (A) (a) Normally developed, deformed, and dead zebrafish *vs.* concentration of Ag-CALNNK (+) NPs. (b) Normally developed and dead zebrafish *vs.* concentration of supernatant (Sup) removed from Ag-CALNNK (+) NP washing and concentration of CALNNK (+) alone. (B) (a) Normally developed, deformed, and dead zebrafish *vs.* concentration of Ag-CALNNS (~0) NPs. (b) Normally developed and dead zebrafish *vs.* concentration of supernatant (Sup) removed from Ag-CALNNS (~0) NP washing and concentration of CALNNS (~0) alone. (C) (a) Normally developed and dead zebrafish *vs.* concentration of Ag-CALNNE (-) NPs. (b) Normally developed zebrafish *vs.* concentration of supernatant (Sup) removed from Ag-CALNNE (-) NP washing and concentration of CALNNE (-) alone. Note: no deformities were observed.

products from synthesis were contained in the NP solution and that the treatment response was due to the exposure of the Ag NPs and not the chemical used in the synthesis procedure. The percentage of normal zebrafish remained high even in the highest dose of supernatant confirming that the washing procedure carried out on Ag NPs prior to treatment and the chemical by-products are not responsible for the deformities observed (Fig. 32b).

We also examined individual defects associated with charged NPs and the morphological defects observed in zebrafish embryos included yolk sac edema, abnormal finfold and tail development, cardiac malformation and eye deformities in all types of charged nanoparticle treatment (Fig. 33).

The number of defects and its severity were concentration and charge dependent. Severe defects like yolk sac edema, cardiac abnormalities and eye/ head abnormalities were higher in Ag-CALNNE (-) NPs as compared to Ag-CALNNK (+) NPs. Emergence of deformities occurred more frequently in the Ag-CALNNE (-) NP treated embryos as compared to the zebrafish embryos treated with the Ag-CALNNK (+) NPs. Fewer abnormalities were seen in zebrafish embryos treated with Ag-CALNNK (+) (Fig. 32 and 34). The most common deformity observed was a finfold abnormality and disorganization of the finfold tissue. In normally developed zebrafish embryos the fin rays are organized.[24, 53, 86]

The second most common deformity observed in Ag-peptide NPs treated zebrafish embryos was cardiac malformation. Cardiac malformation was displayed as the edema of the pericardial sac region (Fig. 33c). The pericardial sac in embryos with this deformity was extremely large and cardiac arrhythmia was also observed. Zebrafish embryos treated with 0.6 nM Ag-CALNNE (-) concentrations demonstrated cardiac abnormality. At similar concentrations, Ag-CALNNK (+), observed 0% cardiac deformities.

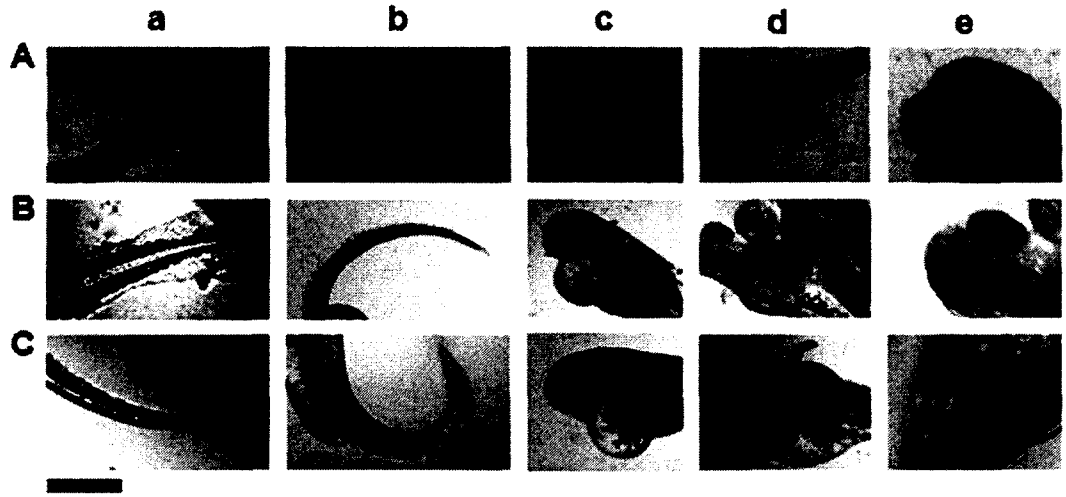

Figure 33. Representative optical images of deformities observed in zebrafish after chronic treatment with Ag-peptide NPs.

(A) Ag-CALNNK (+) NP treated zebrafish displaying (a) finfold abnormality; (b) tail/spinal cord flexure and (c) cardiac malformation, (d) yolk sac edema and (e) no eye formation. (B) Ag-CALNNS (~0) NP treated zebrafish displaying (a) finfold abnormality; (b) tail/spinal cord flexure and (c) cardiac malformation, (d) yolk sac edema and (e) small eyes. (C) Ag-CALNNE (-) NP treated zebrafish displaying (a) finfold abnormality; (b) tail/spinal cord flexure and (c) cardiac malformation, (d) yolk sac edema and (e) small eyes. Scale bar = 500 μm.

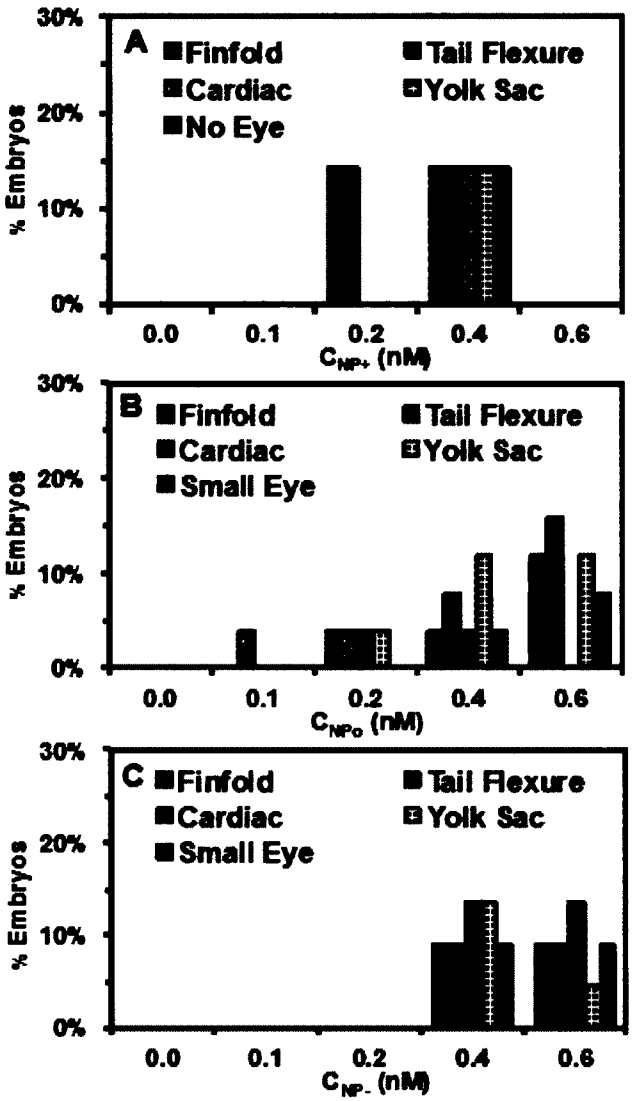

Figure 34. Histograms of the types of deformities *vs.* the percentage of zebrafish.

(A) Ag-CALNNK (+) NPs, (B) Ag-CALNNS (~0) NPs and (C) Ag-CALNNE (-) NPs.

Another prevalent deformity observed in treated zebrafish embryos was yolk sac edema. In normally developing embryos, the yolk sac region is a bulbous area containing yolk that provides nutrients to the developing embryos and during the later developmental process, the yolk sac shrinks[24, 53, 86]. In embryos with yolk sac edema, the yolk sac region was swollen and enlarged (Fig. 33d). In many embryos yolk sac edema was simultaneously observed with cardiac abnormalities. Eye abnormalities, in the form of small eyes, were also widely seen in zebrafish embryos treated with our NPs (Fig. 33e). Percentage of eye abnormalities was significantly higher with Ag-CALNNE (-) as compared to Ag-CALNNK (+). While the Ag-CALNNK (+) observed only one eye/head abnormality at 0.4nM with Ag-CALLNS (~0) and Ag-CALLNE (-) treated embryos there was a higher frequency of eye/head abnormalities for 0.4 nM and 0.6 nM treatment concentration. Most frequent eye abnormalities observed were small eyes and disorganized development. All the deformities showed concentration and charge dependent phenomenon, with increase in nanoparticle concentration there was significant increase in overall deformities in zebrafish embryos in Ag-CALNNS (~0) and Ag-CALNNE (-) NPs.

Characterization of Ag nanoparticles embedded inside fully developed zebrafish

We characterized Ag-CALNNK (+) embedded inside fully developed normal zebrafish that were chronically treated at the concentration 0.2 nM using DFOMS. From a transverse section (Figure 35A), we found that these Ag NPs were embedded in multiple areas (eye and brain) of a normally developed zebrafish (Fig. 35B, a-b, respectively). To confirm that these were NPs and not cellular debris from the zebrafish tissue, we took LSPR spectra of the NPs in the different areas (Fig. 35C). These results demonstrate that Ag-CALNNK (+) are biocompatible with developing zebrafish at given concentrations. We also performed a control experiment by imaging tissue sections of a zebrafish that developed in the absence of nanoparticles and did not observe the individual Ag nanoparticles as we did in the treated zebrafish.

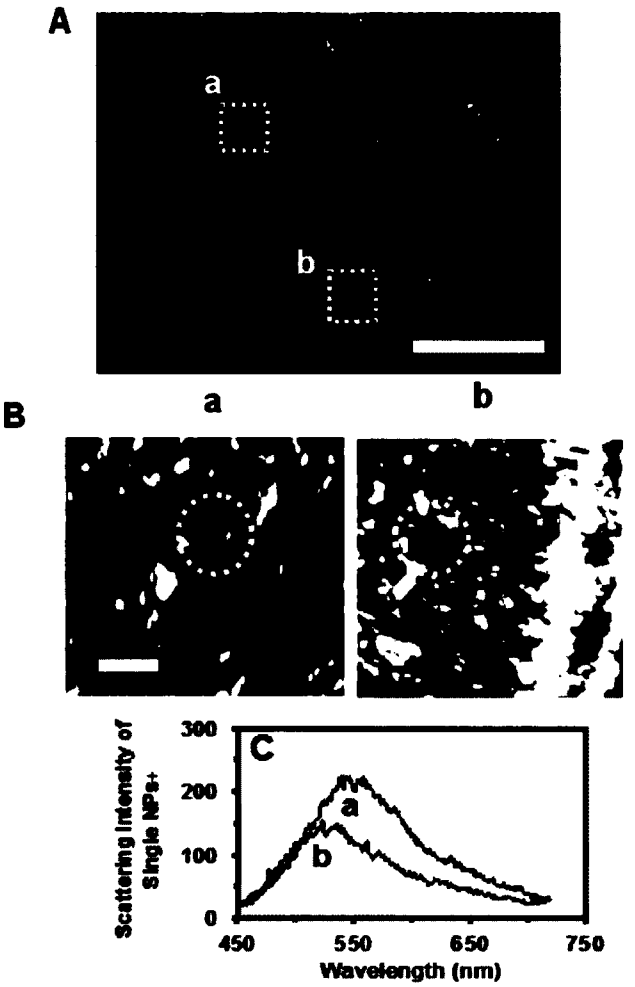

Figure 35. Characterization of individual Ag-CALNNK (+) NPs embedded inside a fully developed normal zebrafish using DFOMS.

(A) Optical image of a fixed transverse section of a normal zebrafish. The dashed rectangles highlight representative areas: (a) eye and (b) brain. Scale bar = 500 μm. (B) Zoom-in optical images of those tissue sections outlined in (A). The circles highlight representative individual NPs embedded in the tissue sections that were characterized. Scale bar = 50 μm. (C) LSPR spectra of those single Ag-CALNNK (+) NPs circled in (B), with λ_{max} at (a) 551 nm (green) (FWHM = 111 nm) and (b) 532 nm (green) (FWHM = 98 nm).

SUMMARY

In this study we were able to design and characterize different charged single Ag nanoparticle optical probes and follow their transport, diffusion, and toxicity in early development of zebrafish embryos in real-time to effectively monitor for an extended duration of time. We determined that the different charged nanoparticle optical probes could generate particular phenotypes in a dose dependent and charge dependent manner. We also demonstrated that negatively charged Ag nanoparticles exhibit more toxicity in the form of increased deformities and death at the same concentrations as the positively charged Ag nanoparticles.

The negative charge of the NPs definitely contributed to the toxicity during the development of the embryo. At the same concentrations of positively charged Ag NPs, there were less overall deformities and less increase in death. According to our findings, it appears that positively charged Ag NPs are more biocompatible at higher concentrations; though the negatively charged Ag NPs were found to be biocompatible at a low concentration (0.1 nM) it seems that positive charged Ag NPs are more biologically compatible for a developing organism. Recent studies investigating nanoparticle toxicity have demonstrated that surface charge of the nanoparticle to be very significant in how a living system responds to the nanoparticle especially related to proper distribution and clearing from the body.[72, 87-89] The results of our study indicate strong concentration and charge dependence for Ag NP biocompatibility in developing zebrafish embryos.

Previous studies have shown that surface charge determines if and how a nanoparticle will get into cells.[90] This is vital especially if looking at nanoparticles for use as delivery vehicles because if it cannot move inside the cell successfully, the drug or treatment will not be delivered.[91] Additional studies have shown a significant relationship between surface charge and the ability to generate ROS causing inflammatory effects to living cells and tissues.[92] A decrease in surface charge of Ag NPs can be considered as one central characteristic, which could

result in more toxicity.[6] We determined from this experiment that our surface charged Ag NPs were able to transport and diffuse into our *in vivo* model system effectively without using any outside aid, for example, microinjection. It was determined that the surface charged Ag NPs were able to diffuse into the chorion via simple Brownian diffusion as we have observed in our previous studies.[11]

The deformities that we observed were finfold, tail flexure, cardiac malformation, yolk sack edema, and eye malformation and these were dependent on the concentration of the surface charged Ag NPs as well as the charge. Recent studies using mice observed the similar toxicity findings and an inability for the mice to clear negatively charged NPs from their systems.[93-96] The researchers found that negatively charged NPs in mice caused malformations related to clogging of nanoparticles in organ systems[93-95]. It was also determined that an increase in apoptosis was found to occur.[96]

It is possible that the negatively charged Ag NPs are interacting with developmental pathways and interrupting dynamic events and causing several different deformities at one time. Further studies are underway to determine the cellular and molecular mechanisms involved in the toxicity.

In conclusion, we were able to determine that positive and negative surface charged Ag NPs are able to transport, diffuse, and create toxic, as well as non-toxic effects on our zebrafish embryos. We were also able to determine that positively charged NPs are more biocompatible at higher concentrations than negatively charged Ag NPs. It was also determined that zebrafish embryos served as an effective *in vivo* model system, one that can be used to examine different surface charges of nanoparticles and determine which surface charged nanoparticles would be most biocompatible in a living system.

METHODS

Synthesis and Characterization of Stability of Ag-CALNNK, Ag-CALNNS, and Ag-CALNNE NPs

For Ag-CALNNK NPs, 50 ml of Ag NPs were synthesized as described previously. After 45 minutes of stirring, PEG-20 was added to a final concentration of 0.05% w/v under stirring. After 5 minutes of further stirring the solution was filtered through a 0.22 µm filter[39, 97]. 2.5 ml of the Ag NPs with PEG-20 was pipette into a 15 ml polypropylene tube. 10 such tubes were prepared. To each tube 34 µl of 28 mM buffered CALNNK was added drop by drop along the sides of the tube while vortexing the tube. The solution was then mixed on a shaker for 12 hours at 4°C.

For Ag-CALNNS NPs, 50 ml of Ag NPs were synthesized as described previously. After 45 minutes of stirring, PEG-20 was added to a final concentration of 0.05% w/v under stirring. After 5 minutes of further stirring the solution was filtered through a 0.22 µm filter[39, 97]. 2.5 ml of the Ag NPs with PEG-20 was pipette into a 15 ml polypropylene tube. 10 such tubes were prepared. To each tube 57 µl of 17 mM buffered CALNNS was added drop by drop along the sides of the tube while vortexing the tube. The solution was then mixed on a shaker for 12 hours at 4°C. All three peptides were 0.5 mM Phosphate buffer pH 7.0 with 1.5 mM NaCl.

For Ag-CALNNE NPs, Ag NPs were synthesized as described previously. PEG-20 was added to a final concentration of 0.05% w/v under stirring. After 30 minutes of stirring the solution was filtered through a 0.22 µm filter[39, 97]. 25 ml of the Ag NPs with sodium citrate dihydrate and PEG-20 was kept stirring. To it 630 µl of 15 mM buffered CALNNE was added quickly. The solution was stirred at room temperature for 1 hour and then mixed for 12 hours at 4°C.

The NPs were washed and characterized as described previously.

Breeding and Monitoring of Zebrafish Embryos

We housed wild type adult zebrafish (Aquatic Ecosystems) in a stand-alone system (Aquatic Habitats) and maintained, bred, and observed them as described previously.[11, 45]

***In Vivo* Characterization and Analysis of Transport and Dose-Dependent Biocompatibility and Toxicity of NPs**

Cleavage-stage living embryos (8-64 cell stage; 0.75-2.25 hpf) incubated with 0.2 nM NPs were characterized for transport and diffusion as described previously.

To study the dose-dependent effects of NPs on embryonic development, a dilution series of washed peptide-conjugated Ag NP solutions (0, 0.1, 0.2, 0.4, and 0.6 nM) were incubated chronically with cleavage (8-cell) stage embryos in egg-water for 120 hpf. Each experiment was carried out at least three times and total number of embryos at 35-40 was studied for each individual concentration to gain representative statistics. Nanoparticle concentrations were calculated as described previously[11]. Embryo controls and observations were carried out as described previously.

Characterization of NPs Embedded Inside Fully Developed Zebrafish

Characterization of the embedded peptide-conjugated Ag NPs (0.2 nM) in the tissues of treated zebrafish, was done as described previously (Fig. 35).

CHAPTER V

PROBING OF TRANSPORT, BIOCOMPATIBILITY AND TOXICITY OF SINGLE 42 NM SILVER NANOPARTICLES IN EARLY DEVELOPMENT OF ZEBRAFISH EMBRYOS

INTRODUCTION

Nanoparticles have been increasingly used in consumer products, ranging from cosmetics, toothpastes, socks, home appliances, water treatment, to disinfection.[98] Thus, it is crucial to study their potential nanotoxicity and environment impacts. Potential release of nanomaterials into aquatic environments would lead to a direct impact on human health, due to human consumption of fish and their ability to bioconcentrate trace contaminants from environment. In previous chapters, we studied transport and effects of smaller Ag NPs (11.6 ± 3.5 nm) on embryonic development and determined their chemical-dependence. In this study, we investigated the transportation and effects of stable and purified medium-sized Ag NPs (41.6 ± 9.1 nm) on embryonic development, aiming to better understand size-dependent transport and toxicity of Ag NPs.

RESULTS AND DISCUSSION

Synthesis and Characterization of Stable and Purified Ag NPs

Ag NPs were synthesized, purified and characterized, as described in Methods. Notably, highly purified Ag NPs were produced by thoroughly washing Ag NPs with deionized (DI) water to remove potential residual chemicals involved in NP synthesis via centrifugation. The NPs were then suspended in egg-water (1.0 mM NaCl, embryonic medium) for study of their stability and their effects on embryonic development.

HRTEM images of single Ag NPs and histogram of their size distribution (Figure 36A and B) show nearly spherical shaped NPs with average diameters of 41.6 ± 9.1 nm, ranging from 33 to 51 nm. Dark-field optical images of single Ag

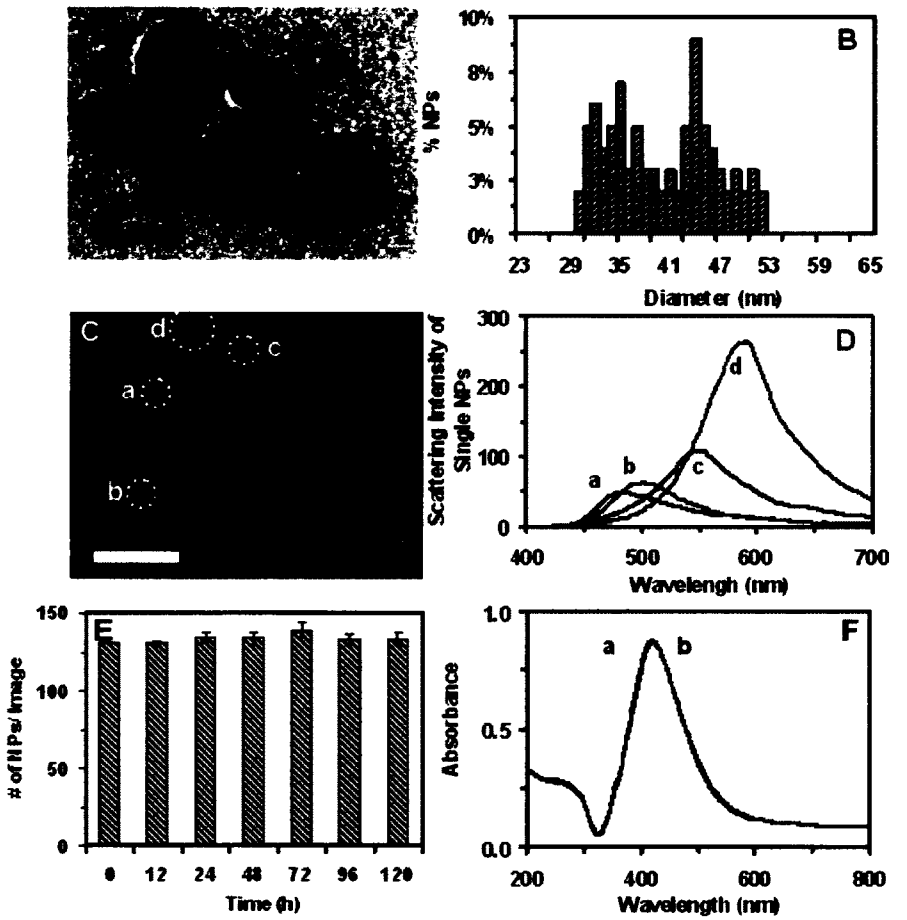

Figure 36. Characterization of stability and physicochemical properties of Ag NPs suspended in egg-water. (A) HRTEM image show spherical shape of single NPs. (B) Histogram of size distribution of single NPs determined by HRTEM show average diameters of 41.6 ± 9.1 nm. (C) Dark-field optical image of single NPs shows that majority of NPs are plasmonic green (D) LSPR spectra of single NPs show λ_{max} (FWHM) at: (a) 458 (83); (b) 471 (75); (c) 543 (84); (d) 594 (90) nm. (E) Number of individual NPs measured over time using DFOMS shows 131± 2, 131 ± 2, 134 ± 3, 134 ± 4, 139 ± 5, 133 ± 3 and 131 ± 4 per image at 0, 12, 24, 48, 72, 96, and 120 h. (F) UV-Vis absorption spectra of NPs in (E): (a) 0 and (b) 120 h show their peak absorbance at 0.87 with peak wavelength (FWHM) at 418 (100) nm remain unchanged over time, showing high stability of NPs in egg-water. Scale bars in (A) and (C) are 50 nm and 2 μm, respectively.

NPs suspended in egg-water (Figure 36C) show single plasmonic green NPs as majority with some blue and very few red NPs. Localized surface plasmon resonance (LSPR) spectra of representative single NPs (Figure 36D) show their peak wavelengths (λ_{max}) with full-width-of-half-maximum (FWHM) at 458 (83), 471 (75), 543 (84), and 594 (90) nm.

The stability (non-aggregation) of the purified NPs in egg-water were characterized over the duration of embryonic development (120 h) at single-NP resolution using DFOMS, UV-vis absorption spectroscopy and dynamic light scattering (DLS). The number of NPs dispersed in egg-water (Figure 36E) remains unchanged over 120 h, indicating that NPs are stable (non-aggregated) in egg-water. Absorbance of UV-vis spectra of NPs in egg-water (Figure 36F) show that their absorbance of 0.87 with peak wavelength (FWHM) of 420 (100) nm remain unchanged for 120 h. Size distributions of NPs measured by DLS show their average diameters remain essentially unchanged at 45.5 ± 9.8 nm for 120 h. Note that NPs are solvated in egg-water, which leads to larger diameter than those measured by HRTEM (Figure 36A, B). Taken together, these results demonstrate that NPs are stable (non-aggregated) in egg-water over the entire duration of embryonic development (120 h). Notably, contaminated unpurified chemicals would have attributed to observable toxicity and unstable NPs in the medium would lead to their size and dose changes over time, which had made the study of nanotoxicity unreliable. Therefore, purified and stable nanomaterials are essential for probing their size and dose dependent effects on living organisms.

Real-Time Imaging of Transport of Single Ag NPs into/in Embryos

We studied diffusion and transport of single NPs in cleavage-stage embryos by incubating NPs with the embryos and tracking their diffusion into and in embryos in real time using DFOMS. We first focus on probing of entry of single NPs into embryos from egg-water (outside chorion, OC) and then inside the embryos.

Optical images of the embryos (Figure 37) illustrate interface of egg-water with chorionic space (CS) (chorionic layer, CL), CS, and interface of CS with inner mass of embryos (IME), and transport of individual NPs through these interfaces into IME. We found arrays of chorionic pore canals (CPCs) with diameters of 0.5-0.7 μm and distances among nearby pores at 1.5-2.5 μm on CL of the embryos (Figure 37B) using DFOMS, which agree excellently with those characterized using scanning electron microscopy (SEM).[25] Individual NPs diffused through chorionic pores to enter CS, then diffused in CS and finally entered into IME (Figure 37B-D).

Notably, distinctive plasmonic optical properties (colors) of single Ag NPs enable them to be distinguished from debris, embryonic cells and tissues. Size-dependent plasmonic properties of single NPs enable their sizes to be determined using DFOMS via optical nano rulers, as we described previously. The results show that single NPs with diameters of 33-51 nm can passively diffuse into the embryos.

The diffusion modes of individual NPs were characterized as NPs were diffusing into/in embryos by tracking diffusion trajectories of single NPs and plotting real-time squared displacement (RTSD) versus diffusion time. Notably, embryonic environments are highly heterogeneous and change over time, as embryos develop. Thus, we used RTSD (diffusion distance at each time interval) rather than mean-squared displacement (MSD) (average distance over time) to investigate diffusion modes of single NPs.

Plots of RTSD versus time for single NPs that were diffusing through CPCs into CS, in CS into IME, and IME show stepwise linearity, which suggests highly heterogeneous embryonic environments. As described by diffusion theories,[26-28] the linear plots indicate simple random Brownian motion and steps show restricted diffusion, suggesting that passive diffusion of single NPs (but not active

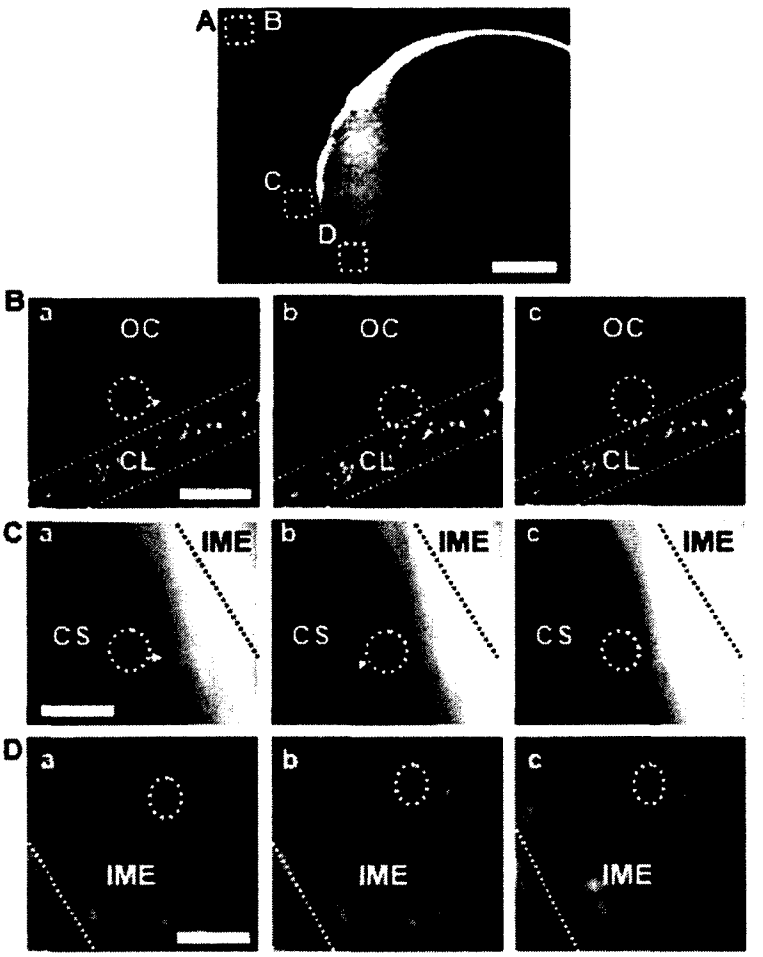

Figure 37. Real-time imaging of diffusion of single Ag NPs into single cleavage-stage embryos. (A) Optical image of cleavage-stage embryo in egg-water. Chorionic layer (CL), chorionic space (CS), and the interface of the CS with inner mass of embryo (IME) are squared as (B-D), respectively. (B-D) Sequential dark-field optical images of zoom-in squared areas in (A), show the diffusion of single NPs (circle) from egg-water (outside chorion, OC) into CL, in CS into IME, and within the IME. The time intervals between sequential images in (B-D) are 1.1 s. See real-time Videos S1-3 in SI. Scale bars are 125 μm in (A) and 20 μm in (B-D).

cellular signaling) enable them to enter embryos. Individual NPs were trapped from time to time as they diffused from egg-water into CS and from CS to IME. Interestingly, single NPs were trapped more often in IME, which was more viscous than CS.

Diffusion coefficients (D) of single NPs were determined by dividing the slopes of linear plots with four using two-dimensional (2D) Random walk theory (RTSD = $4D\Delta t$). They are (5.0±1.0) $x10^{-11}$, (4.9±3.0) $x10^{-9}$, and (5.1±8.5) $x10^{-10}$ cm^2s^{-1} for single plasmonic green NPs going through CPCs from egg-water into CS, in CS into IME, and in IME. Diffusion coefficients of the single NPs in egg-water measured using the same approaches are (5.2±1.8) $x10^{-8}$ cm^2s^{-1}.

Notably, diffusion coefficients of single NPs are inversely proportional to viscosities of medium based upon Stokes-Einstein equation, $D = kT/(6\pi\eta a)$, where k is Boltzmann constant; T is temperature; a is radii of single NPs; and η is viscosity of medium where NPs diffuse in. The results show that CL has the highest viscosity and IME has higher viscosity than CS. Embryonic environments are orders of magnitude more viscous than egg-water. The large standard deviations of diffusion coefficients of single NPs in embryos, especially in IME, show high heterogeneities (viscosity gradient) of embryonic environments. The results also demonstrate that single NPs can serve as optical probes to study embryonic nanoenvironments.

Early-Development Embryos as Ultrasensitive *In Vivo* Assays

Optical images in Figure 38A show normal developmental stages of zebrafish embryos, which includes cleavage (0.75-2.25 hours-post-fertilization, hpf), gastrula (10 hpf), segmentation (24 hpf), and hatching stages (48 hpf), and a fully developed zebrafish (120 hpf). All embryonic developmental stages of zebrafish are well defined.

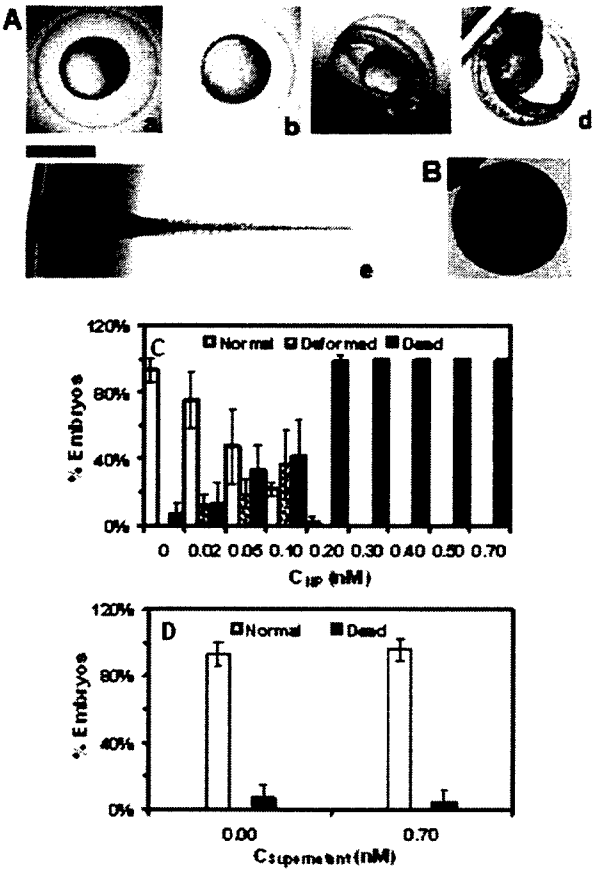

Figure 38. Study of dose-dependent effects of Ag NPs on embryonic development using embryos as ultrasensitive *in vivo* assays. (A) Optical images of normally developing embryos at (a) cleavage-stage (0.75-2.25 hpf); (b) late gastrula stage (10 hpf); (c) late segmentation stage (24 hpf); (d) hatching stage (48 hpf); (e) fully developed larvae (120 hpf). (B) Dead embryo. (C) Histograms of distributions of embryos that developed to normal and deformed zebrafish or became dead versus NP concentration. (D) Control experiments: histograms of the distributions of embryos that developed to normal zebrafish or became dead either in egg-water alone or versus concentration of supernatant, which was collected from the last washing of NPs with DI water. A total of 36 embryos were studied for each NP concentration and control in (C-D). Scale bar is 500 μm for all images in (A).

The earlier developmental stage, such as cleavage stage, is likely more prone and sensitive to the effects of external substances (e.g., drugs, NPs) than later stages. Notably, the cleavage-stage embryos undergo drastic changes to lay down foundation for developing different organs, and their related and important developmental mechanisms remains not yet fully understood.[16, 18, 51] Thus, we select cleavage-stage embryos for study of transport, biocompatibility and toxicity of NPs, aiming to develop ultrasensitive *in vivo* assays for effectively screening of NPs and to rationally design biocompatible NP probes for *in vivo* imaging.

Study of Dose and Size-Dependent Biocompatibility and Toxicity of Ag NPs

We studied dose-dependent toxic effects of NPs on embryonic development by incubating cleavage-stage embryos with various concentrations (0-0.70 nM) of colloid Ag NPs suspended in egg-waters for 120 h. Representative embryonic developmental stages were imaged and assayed over time until the embryos were fully developed. Number of embryos that developed to normal zebrafish (Figure 38e), became dead (Figure 38B), and deformed zebrafish (Figure 39A) were recorded.

The results in Figure 38C demonstrate high dependence of embryonic development upon the NP concentrations, or doses. As NP concentration increases from 0 to 0.7, the number of embryos that developed to normal zebrafish decreases, while the number of embryos that became dead increases. Interestingly, the number of embryos that developed to deformed zebrafish increases as NP concentration increases up to 0.2 nM. However, none of embryos survived beyond that, which is attributed to the decrease of deformed zebrafish and the increase of dead embryos at NP concentration higher than 0.2 nM.

Severe deformities (e.g., cardiac abnormalities, yolk sac edema, and eye/head abnormalities) were observed at very low concentrations (< 0.2 nM), as summarized in Figure 39A. For example, finfold deformities with disorganized and improperly arranged finfolds (Figure 39A, a-b); abnormal tail flexing (spinal cord) with nearly 180° bent (c-d); cardiac malformations (edema of the pericardial sac region and cardiac arrhythmia) and Yolk sac edema with swollen and enlarged yolk sac (e); and head edema and severe eye abnormalities with micropthalmia (small eyes) and dissymmetric eyes (f-g), were observed at low concentrations (< 0.2 nM). These eye abnormalities were uncommon deformations and rarely reported. Notably, one severe deformation (e.g., cardiac, eye or head) observed in any given zebrafish was typically accompanied with several other types of deformations (e.g., finfold, tail and yolk sac edema). The results suggest that embryonic developmental pathways may be highly regulated and one pathway may highly depend upon others.

Unlike our previous studies of smaller Ag NPs (11.6 ± 3.5 nm), more embryos died and developed more severe deformed zebrafish at the lower concentration, showing that the larger NPs are more toxic than smaller NPs. Two control experiments were conducted simultaneously by incubating the embryos with egg-water alone (blank control) and with the highest concentration of supernatants collected from the last washing of NPs, which had been thoroughly washed and stored in DI water for at least five days. The supernatants were used to determine potential toxic effects of trace chemicals (e.g., Ag^{+}) results from NP synthesis or degradation over time, which serves as control experiment to validate the observed toxicity in Figure 38C is attributed to NPs, but not other chemicals. The results from control experiments for embryos incubated with egg-water and the supernatants alone (Figure 38D) show that over 95% of embryos developed to normal zebrafish, and no deformed zebrafish

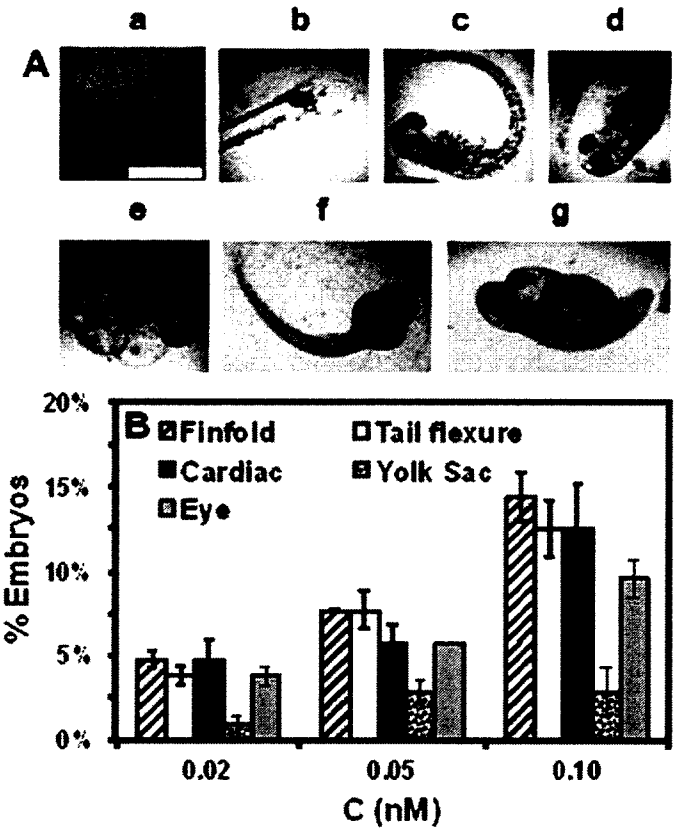

Figure 39. Dependence of types of deformed zebrafish on NP concentration. (A) Optical images of deformed zebrafish show: (a-b) finfold abnormalities; (c-d) tail/spinal cord flexure; (e) cardiac malformation and yolk sac edema; and (f-g) eye abnormality. (B) Histograms of distributions of embryos that developed to deformed zebrafish with five distinctive types of deformities at NP concentration of 0.02, 0.05 and 0.10 nM. A total of 36 embryos were studied for each NP concentration and control. Scale bar is 500 μm for all images in (A).

were observed. Thus, the deformed zebrafish and high percent of dead embryos observed in Figure 38C were attributed to NPs, but not contaminated chemicals.

Quantitative Characterization of Single Ag NPs Embedded in Zebrafish

To address why some embryos developed normally while others were deformed or dead, we characterized single Ag NPs embedded in various tissues of zebrafish, which had been incubated with NPs (< 0.2 nM) chronically for 120 h, since they were cleavage-stage embryos. Longitudinal ultrathin sections (1-2 μm thickness) of representative deformed zebrafish with all types of deformities show NPs embedded in its eye (retina), brain, heart, and tail (Figure 40), as characterized by distinctive LSPR spectra of individual NPs. Interestingly, transverse ultrathin sections of normally developed zebrafish also show NPs embedded in the tissues similar to those of deformed zebrafish. The results suggest that NPs diffused into embryos and stayed inside the embryos throughout their entire development stages (Figure 41). The red shift of LSPR spectra of individual NPs embedded in the tissues may be attributed to the changes of their surrounding environments (e.g., dielectric constant of embedded medium), which differ from egg-water.

The number of individual NPs embedded in eye (retina) and brain tissues of normal and deformed zebrafish (Figure 42) shows that more plasmonic blue and green (smaller) NPs were present in normal zebrafish, while more plasmonic red (larger) NPs were found in deformed zebrafish. Note that size-dependent plasmonic optical properties of single NPs enable us to determine their sizes *in situ* in real time using single NP optical ruler, showing that the red NPs are the largest NPs while the blue NPs are the smallest NPs. The results suggest that larger NPs are more toxic than smaller NPs, further demonstrating size-dependent nano biocompatibility and toxicity.

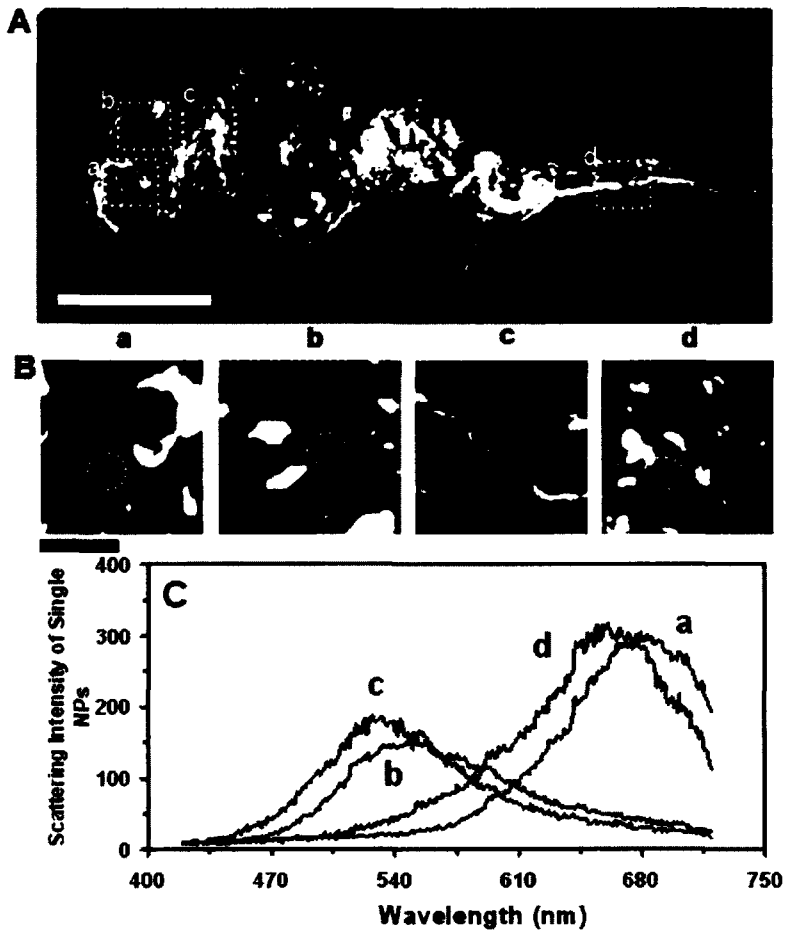

Figure 40. Characterization of individual Ag NPs embedded in deformed zebrafish using DFOMS. (A) Optical image of ultrathin longitudinal section of fixed zebrafish with five types of deformities. The rectangles highlight its (a) retina (eye), (b) brain, (c) cardiac, and (d) tail. (B) Zoom-in optical images of the tissue sections highlighted in (A) show embedded single NPs. (C) LSPR spectra of the individual NPs circled in (B) show λ_{max} (FWHM) at: (a) 682 (87), (b) 552 (111), (c) 553 (94), and (d) 660 (106) nm. Scale bars are 500 μm in (A) and 50 μm in (B).

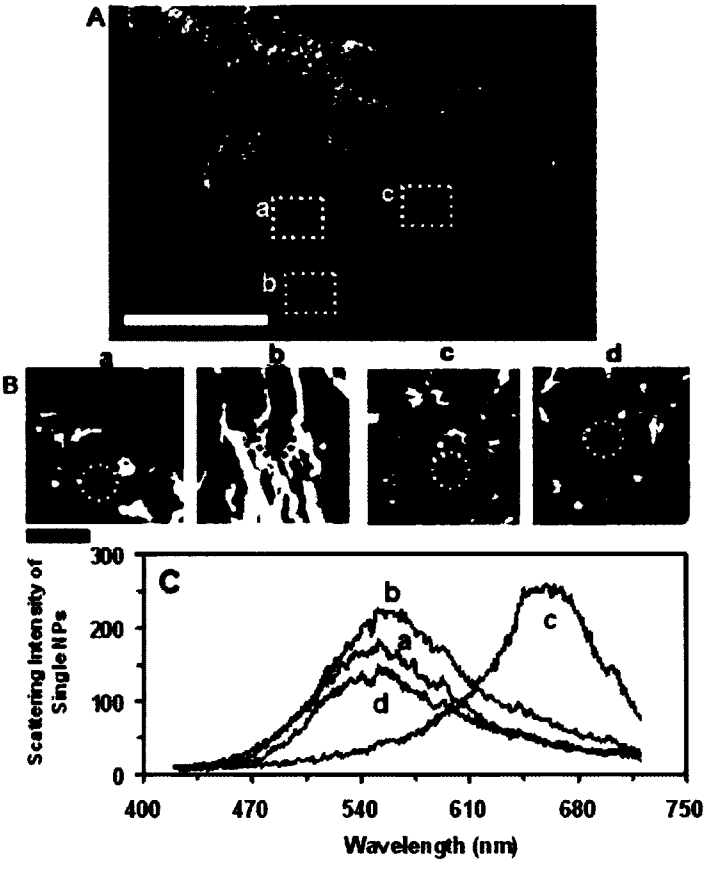

Figure 41. Characterization of individual Ag NPs embedded in normally developed zebrafish using DFOMS. (A) Optical image of ultrathin transverse section of fixed zebrafish. The dashed rectangles outline its (a) retina, (b) lens, (c) forebrain, and (d) hindbrain tissues. (B) Zoom-in optical images of the tissue sections highlighted in (A) show individual embedded NPs. (C) LSPR spectra of representative single NPs circled in (B) show its λ_{max} (FWHM) at (a) 553 (113), (b) 559 (134), (c) 675 (70), and (d) 552 (106) nm. Scale bars in (A-B) are 250 and 50 μm, respectively.

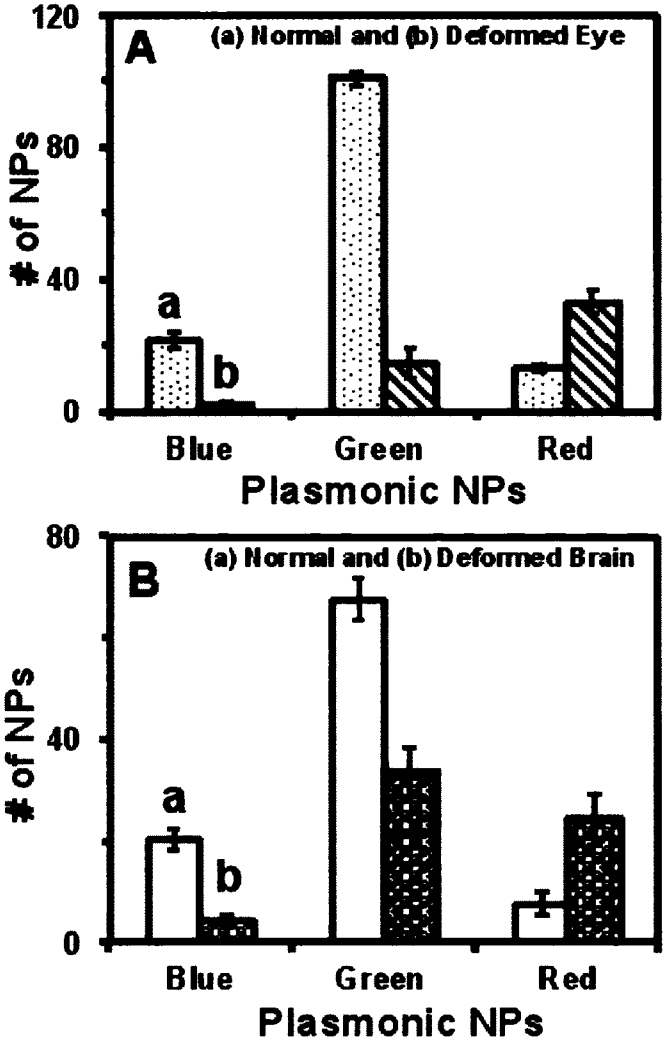

Figure 42. Study of sizes and number of individual Ag NPs embedded in both deformed and normal zebrafish. Histograms of the number and sizes (colors) of single NPs embedded in: (A) eye (retina) and (B) brain tissues of normally developed and deformed zebrafish. Tissues of 15 normal and deformed zebrafish each were analyzed.

The results also suggest that individual embryos may respond to nanotoxicity very differently. Some embryos may be more tolerant to nanotoxicity than others, underscoring the importance of study of biocompatibility and toxicity of NPs at single embryo resolution. Random diffusion of single NPs in embryos during their development may also play significant roles in creating nanotoxiciy, emphasizing the importance of study of nano biocompatibility and toxicity in real time at single NP resolution. Taken together, this study shows that early-developmental stage embryos can serve as ultrasensitive *in vivo* assays for effectively screening of biocompatibility and toxicity of NPs.

SUMMARY

In summary, we have designed, synthesized and characterized stable (non-aggregated) and purified Ag NPs with average diameters of 41.6 ± 9.1 nm, and developed DFOMS for imaging of single NPs *in vivo* in real time. We found that individual NPs passively diffused into embryos through chorionic pores of embryos, and stayed inside the embryos throughout the embryonic development. Dose-dependent toxic effects of NPs on the embryonic development were observed, showing that they were more biocompatible at lower doses and became toxic at higher doses. As NP concentrations increase, the number of embryos that developed to normal zebrafish decreases, while the number of embryos that became dead increases. In comparison with our previous studies of effects of smaller Ag NPs (11.6 ± 3.5 nm) on embryonic development, we found striking size-dependent toxic effects of NPs on embryonic development. Notably, larger NPs create higher toxic effects and more severe deformed zebrafish at the lower concentration than smaller NPs. This study offers new evidences of size-dependent nanotoxicity at single-NP resolution.

METHODS

Synthesis and Characterization of Stable and Purified Ag NPs

Ag NPs (41.6 ± 9.1 nm in diameter) were synthesized by quickly adding sodium citrate (10 mL, 34 mM) into a refluxing (100°C) $AgNO_3$ aqueous solution (500 mL, 1.1 mM) under stirring. The mixture was refluxed and stirred for 45 min, as the solution color turned from colorless to straw yellow, then opaque and finally muddy yellow. The heating was stopped and the solution was cooled gradually to room temperature under stirring. The NP solution was filtered using 0.22-μm filters. All chemicals, except those indicated, were purchased from Sigma and used as received.

The NPs were immediately washed three times as described previously. Sizes and stability of NPs were characterized as described previously.

Breeding of Zebrafish Embryos

Wild-type adult zebrafish were maintained and bred as described previously.

Real-time Tracking of Diffusion of Single Ag NPs into/in Embryos

The cleavage-stage embryos with egg-water were incubated with purified NPs (0.2 nM) and transport and diffusion was characterized as described previously.

Study of Dose-Dependent Biocompatibility and Toxicity of NPs and Control Experiments

The cleavage-stage embryos in egg-water were incubated with a dilution series of NPs (0, 0.02, 0.05, 0.1, 0.2, 0.3, 0.4, 0.5, and 0.7 nM) or (0, 5, 12, 24, 48, 95, 119, and 166 μg/mL) and supernatant control experiments were carried out as described previously. Each experiment was carried out at least three times and a total number of 36 embryos were studied for each NP concentration and each control experiment to gain representative statistics and observations were done as described previously.

Characterization of Single Ag NPs Embedded in Individual Zebrafish

We characterized individual NPs embedded in the tissues of zebrafish as described previously (Figures 40-42).

Data Analysis and Statistics

A minimum of 100 Ag NPs was imaged and characterized for each measurement of their sizes and stability in egg-water using HRTEM and DFOMS. A minimum of 300 NPs in total was studied for each sample via three repeated measurements. For real-time imaging of diffusion of single NPs into and in embryos over time, a minimum of 15 embryos were studied for each given concentration with 5 embryos for each measurement. For study of dose-dependent effects of NPs on embryonic development, a total number of 36 embryos were studied for each NP concentration and each control experiment over 120 hpf with a minimum of 12 embryos studied in each measurement.

CHAPTER VI

ASSAY OF TRANSPORT, BIOCOMPATIBILITY AND TOXCITY OF SINGLE 95 NM SILVER NANOPARTICLES USING ZEBRAFISH EMBRYOS

INTRODUCTION

Advances in nanotechnology demand rational design of biocompatible nanomaterials and development of effective means and assays for well characterization and rapid screening of biocompatibility and toxicity of nanomaterials. Engineered nanomaterials possess distinctive physiochemical properties and promise wide ranges of applications from consumer products to health care.[98-101] In this study, we synthesized and purified larger Ag NPs with average diameters of 95.4 ± 19.0 nm and used zebrafish embryos as *in vivo* assays to study the transportation and effects of the NPs on embryonic development. We compared the results from this study with those from our previous studies of transport and effects of smaller Ag (11.6 ± 3.5 nm) on embryonic development, aiming to better understand size-dependent transport and toxicity of Ag NPs.

RESULTS AND DISCUSSION

Synthesis and Characterization of 95 nm Ag NPs

We synthesized and purified Ag NPs as described in the Methods. TEM images of purified single Ag NPs and their size distribution in Figure 43A and B show oval NPs with average diameters of (95.4±19.0) nm. Representative dark-field optical image of single Ag NPs in Figure 43C show that majority of single NPs exhibit plasmonic green color with a few being blue and red. Localized surface plasmonic resonance (LSPR) spectra of representative single NPs show peak wavelengths (λ_{max}) at 478 nm with (full-width-of-half-maximum, FWHM, 78

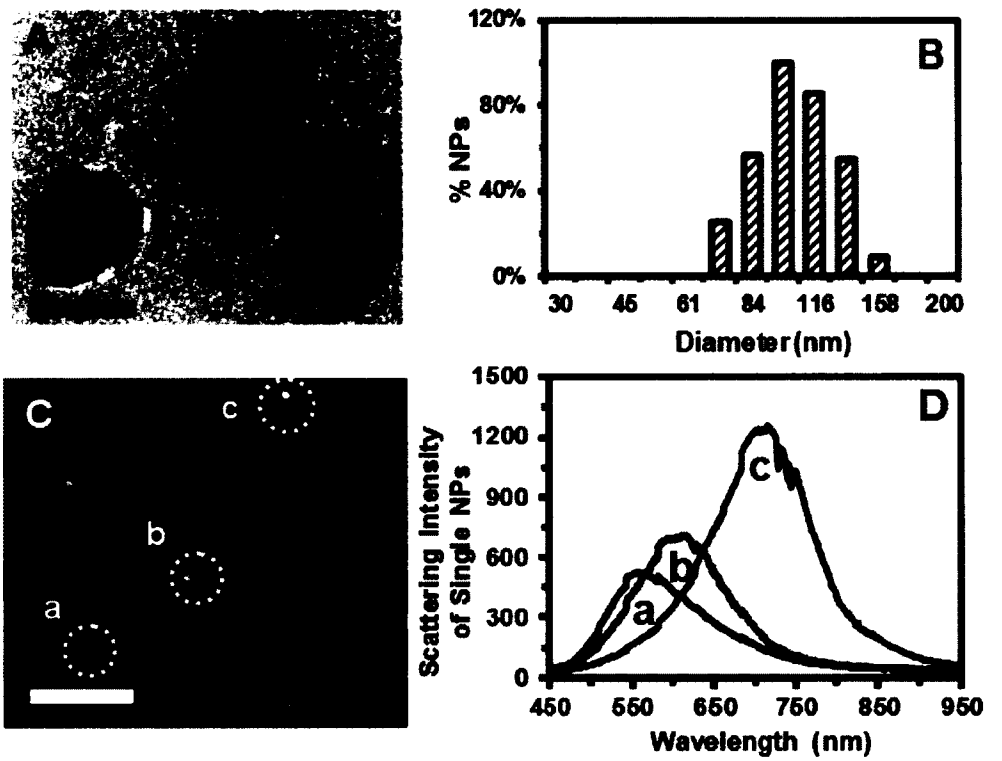

Figure 43. Characterization of sizes, shapes, and plasmonic optical properties of single Ag NPs.

(A) Representative HRTEM image show the sizes, shapes and morphologies of single Ag NPs. (B) Histogram of size distribution of single Ag NPs determined by HRTEM shows their average diameters as 95.4±19.0 nm. (C) Representative dark-field optical image of single Ag NPs shows individual plasmonic green, yellow and red NPs. (D) LSPR spectra of single Ag NPs (green, yellow, and red) show λ_{max} (FWHM) at 558 (78), 610 (89) and 704 (91) nm, respectively. Scale bars are 200 nm in (A) and 2 μm in (B).

nm), 553 nm (FWHM, 89 nm), and 604 nm (FWHM, 91 nm), respectively (Figure 43D). Size-dependent LSPR spectra of single NPs enable their sizes to be determined in situ in real time at the nanometer (nm) scale using DFOMS, as we reported previously.

We characterized the stability (non-aggregation) of the purified NPs suspended in egg-water (embryonic medium) over 120 h at single NP resolution using DFOMS. The number of single NPs in 60 images acquired by DFOMS over 120 h remains essentially unchanged with around 133 NPs per image (Figure 44A), suggesting that the NPs in egg-water are very stable. If NPs were aggregated, the number of NPs in solution would have decreased and their sizes would have increased over time, which would have made the study of dose and size dependent toxic effects of NPs unreliable and irrelevant. Thus, it is crucial to characterize the stability of NPs at single NP resolution in situ in real time. In this study, DFOMS severs as a powerful tool to characterize the number and sizes of single NPs in situ and in real time.

We further characterized the stability of NPs using ensemble measurements, UV-vis spectroscopy and DLS. UV-vis spectra of the NPs in egg-water over 120 h show their absorbance of 2.1 at 418 nm (FWHM, 100 nm) and 1.9 at a shoulder peak of 392 nm (FWHM, 100 nm) remain unchanged (Figure 44B). Size distributions of NPs incubated in egg-water over 120 h, measured by DLS (Figure 44C), show that their average diameters remain essentially unchanged, ranging from 98.2±19.5 nm to 95.3±19.6 nm. The sizes of hydrated NPs became slightly smaller after suspended in egg-water for 120 h, which is likely attributed to the exchange of surface molecules (citrate ions) with chloride ions in egg-water. Similar phenomena were observed previously. Taken together, the NPs are very stable (non- aggregation) in egg-water over 120 h (duration needed for embryos to fully develop), enabling us to investigate their size and dose dependent transport into embryos and their effects on embryonic development over time.

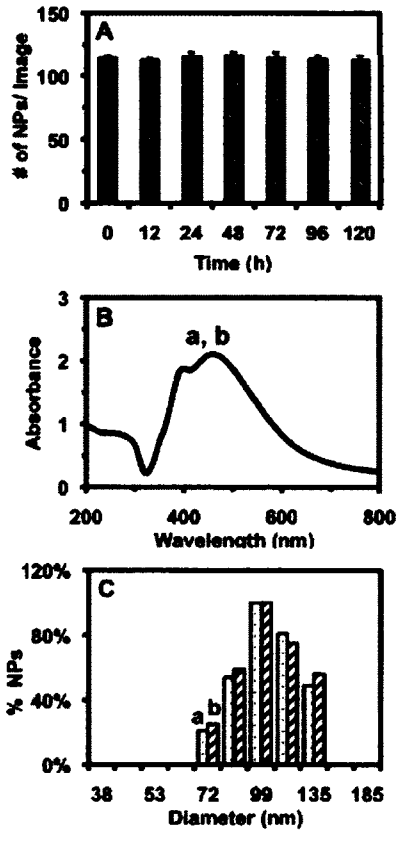

Figure 44. Characterization of stability (non-aggregation) of Ag NPs in egg-water.

(A) The average numbers of single NPs per image acquired by DFOMS, for Ag NPs (2 pM) incubated with egg-water 28^{0}C for 0, 12, 24, 48, 72, 96, and 120 h, are 133±2, 130±2, 135±3, 136±4, 135±3, 139±4 and 130±3, respectively. The number of NPs remains essentially unchanged. Totally, 60 images are acquired with 20 images per measurement at each time point, which allow single NP measurements to gain sufficient statistics and represent bulk analysis. (B) Representative UV-Vis absorption spectra of Ag NPs (2 pM) incubated with egg-water at 28^{0}C for (a) 0 and (b) 120 h shows the peak absorbances of 2.1 at 418 nm (FWHM = 100 nm) and 1.9 at 392 nm (FWHM = 76 nm). Both remain unchanged over time for 120 h.

Embryos as Ultrasensitive *In Vivo* Assays

Optical images of zebrafish embryos show their well-defined developmental stages, which include cleavage (0.75-2.25 hours-post-fertilization, hpf), gastrula (10 hpf), segmentation (24 hpf), and hatching stages (48 hpf), and a fully developed zebrafish (120 hpf).

The earlier developing embryos (cleavage-stage embryos) are highly subjective to toxic effects of external substances. Therefore, they could serve as more sensitive assays for screening of biocompatibility and toxicity of nanomaterials than later stage embryos and fully developed fish. At cleavage stage, the embryos undergo drastic changes to formulate the development of different organs and their related developmental mechanisms remain unexplored.[16, 18, 51] Thus, we chose cleavage-stage embryos as ultrasensitive *in vivo* assays to study transport and toxicity of 90s-nm Ag NPs (Figures 45-47).

Entry of Single Ag NPs into Embryos and Diffusion Mechanisms

To determine whether 90s-nm Ag NPs can enter embryos and their related transport mechanisms, we incubated NPs with cleavage stage embryos and directly tracked diffusion of single NPs into and in embryos in real time using DFOMS. The image of single live embryo in Figure 45A illustrates chorionic layer (CL), chorionic space (CS) and inner mass of embryo (IME). The snapshots of sequential optical images (Figure 45B-D) show that single NPs diffuse from egg-water into CS through chorionic pores (chorionic pore canals, CPCs) on CLs; single NPs diffuse in CS, and diffuse from CS into IME, respectively. Arrays of chorionic pores on CLs were observed and their diameters ranging from 0.5 to 0.7 μm were determined *in vivo* in real time using DFOMS (Figure 3.6B). Interestingly, NPs diffused into embryonic cells on the surface of IME were clearly visualized by DFOMS in real time (Figure 45D).

Notably, single Ag NPs exhibit distinctive plasmonic colors, which enable them to be effectively distinguished from embryonic cells, membranes and debris which appear white under dark-field illumination. Sizes of the single NPs were

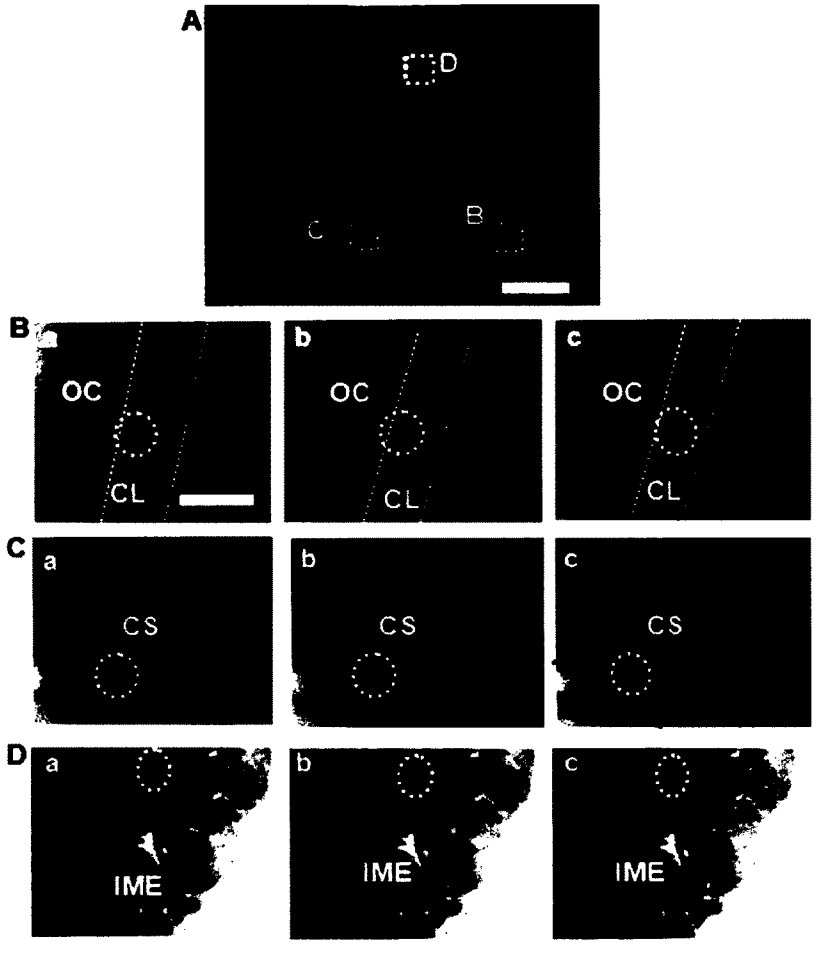

Figure 45. Real-time probing of transport and diffusion of single Ag NPs into/in embryos.

(A) Optical image of the representative cleavage-stage embryo shows the interfaces of chorionic layer (CL) with egg-water (outside chorion, OC), chorionic space (CS), and the interface of CS with inner mass of embryos (IME) as highlighted by (B), (C) and (D), where the transports of single Ag NPs are studied in real time, respectively. (B-D) Sequential dark-field optical images of: (B) the CL (as highlighted by dashed lines), (C) the interface of CS with IME (as marked by dashed lines), and (D) IME, show the diffusion of single Ag NPs (as circled) from outside the chorion (OC) in egg-water into the CL; in CS; and from CS into IME, respectively. The time interval between each sequential image is 1.1 s. Scale bars are 125 μm in (A) and 20 μm in (B-D).

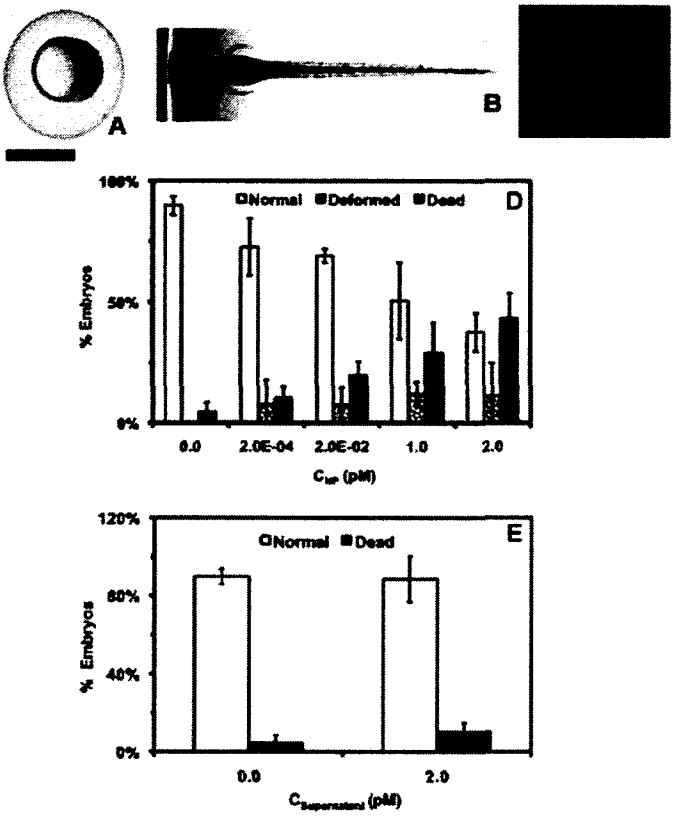

Figure 46. Study of effects of Ag NPs on embryonic development. Optical images in (A-C) show: (A) cleavage-stage embryos (0.75-2.25 hpf), which are incubated with Ag NPs in egg-water for 120 h; and developed to (B) normal zebrafish (120 hpf); or deformed zebrafish in Figure 5 or became (C) dead embryo. Scale bars in (A-C) are 500 μm. (D) Histograms of percent distribution of embryos that developed to normal or deformed zebrafish or became dead show their dependence upon NP concentrations. As NP concentration increases, number of embryos developed to normal zebrafish decreases, while the number of embryos that developed to deformed and became dead increases. (E) Control experiments show the study of embryos incubated with supernatant resulted from washing NPs (instead of NPs) in egg-water. Histograms of distributions of embryos that developed to normal zebrafish or became dead show their independence on supernatant concentration. Over 90% of embryos develop to normal zebrafish. No deformed zebrafish was observed.

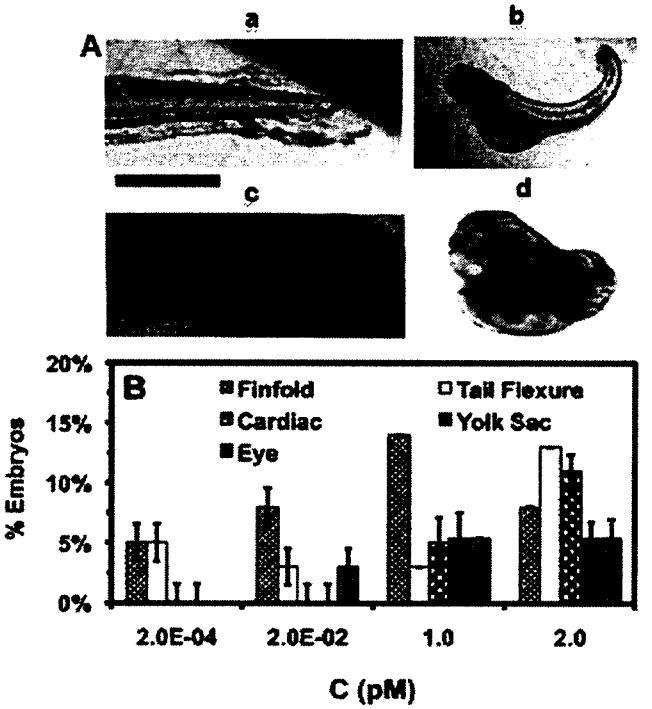

Figure 47. Study of dependence of types of zebrafish deformities upon NP concentration.

(A) Representative optical images of deformed zebrafish show: (a-c) finfold abnormalities; (b) tail/spinal cord flexure; (c, d) cardiac malformation and yolk sac edema; and (d) eye abnormality. Scale bar = 500 μm. (B) Histograms of distributions of percent of embryos that developed to multiple types of deformed zebrafish show their dependence upon NP concentration. As NP concentration increases, the percent of embryos with severe deformities and various types of deformities increase.

determined *in vivo* in real time by their size-dependent LSPR spectra using optical nano rulers as we described previously. The results in Figure 45 show that single NPs with diameters of 95.4±19.0 nm diffused into embryos via chorionic pores.

We further determined the diffusion mechanisms and modes (e.g., random Brownian motion, directed or restricted diffusion) of single Ag NPs entry into the embryos and inside the embryos using diffusion theories. Viscosities inside living embryos vary greatly upon local embryonic environments, which alter over time as embryos develop. Thus, we used real-time square displacement (RTSD, diffusion distance at each time interval) instead of mean-squared displacement (MSD, average distance over time), to determine the diffusion modes and diffusion coefficient of single NPs as they diffused into and through embryos.

Plots of RTSD of single NPs versus time show stepwise linearity, as single NPs diffuse through chorionic pores, in CS, and into IME. As described in diffusion theories, the linear plots of MSD versus time indicate simple random Brownian motion and the steps show restricted diffusion. Thus, the results indicate that passive diffusion of single NPs (but not directed diffusion) enable them to enter embryos. The plots show several steps, indicating that individual NPs were frequently trapped in chorionic pores as they diffused from egg-water into the embryos. Similar phenomena were observed as NPs diffused from CS into IME, indicating dense interface of CS with IME.

We determined diffusion coefficients (D) of single NPs by dividing the slopes of the linear plots with four using two-dimensional (2D) Random walk theory (RTSD = $4D\Delta t$).[28] They are (3.9±7.5) $x10^{-11}$, (7.5±6.0) $x10^{-9}$, and (7.8±8.2) $x10^{-10}$ cm^2s^{-1} for single NPs going through CL into CS, in CS, and into IME. Diffusion coefficients of the single NPs in egg-water measured using the same approaches are (2.8±0.5) $x10^{-8}$ cm^2s^{-1}. The results suggest highly heterogeneous embryonic environments and higher viscosity at IME and CL.

Study of Dose and Size Dependent Toxicity of Ag NPs

To determine the dose-dependent toxicity of NPs, we incubated cleavage-stage embryos with various concentrations (0-2.0 pM or 0-5.7 μg/mL) of purified and stable Ag NPs 95.4±19.0 nm in egg-waters for 120 h, and imaged the embryos as they developed *in situ* in real time. This experimental design enables NPs passively diffuse into embryos without intervention and the study of their effects on embryonic development, which mimics the potential transport and effects of NPs on aquatic and eco- living organisms should NPs release to the environments. We also conducted two types of control experiments simultaneously by incubating the embryos with egg-water alone and with the highest concentration of supernatants collected from the third washing of NPs to determine effects of any potential residential chemicals from NP synthesis.

Embryos at representative development stages were imaged and monitored over time for 120 h until the embryos were fully developed. Optical images in Figures 46A-C and 47 show cleavage-stage embryos, normal developed zebrafish, dead embryos, and deformed zebrafish, respectively. The number of embryos that developed to normal and deformed zebrafish and became dead was determined and plotted against concentrations of NPs and supernatants. The results in Figure 46 show that embryonic development highly depends upon NP concentration (dose). As NP concentration increases from 0 to 2.0 pM, the number of embryos that developed to normal zebrafish decreases, while the number of embryos that developed to deformed zebrafish and became dead increases.

In contrast, control experiments for embryos incubated with egg-water and supernatants alone (in absence of NPs) show that over 95% embryos developed to normal zebrafish and none of embryos developed to deformed zebrafish. Therefore, the deformed zebrafish and dead embryos observed in Figures 46 and 47 were attributed to the NPs, but not residual chemicals from NP synthesis.

We examined individual morphological defects (phenotypes) of deformed zebrafish and found various types of deformation, which includes abnormal finfold and tail/spinal cord, cardiac malformation, yolk sac edema, and eye deformities (Figure 47A). The number of embryos developed to deformed zebrafish with high severity and multiple deformities increases as NP concentration increases (Figure 47B), showing dose-dependent phenotypes.

Finfold deformities (e.g., disorganized and improperly arranged finfolds) and abnormal tail and spinal cord flexing (Figure 47A:ab) were observed in all studied concentrations. Note that normally developed zebrafish shows well organized finfold rays and straight tails (spinal cord) (Figure 46B).

Interestingly, severe deformations, such as cardiac malformations (e.g., edema of the pericardial sac region and cardiac arrhythmia) and yolk sac edema with swollen and enlarged yolk sac (Figure 47Ac) were observed only at higher concentrations (≥ 1 pM). Deformed zebrafish with cardiac abnormalities quite often also shows swollen and enlarged yolk sac (yolk sac edema). In normally developed zebrafish (Figure 46B), the yolk sac (a bulbous area containing yolk that provides nutrients to embryonic development) is much smaller because they should shrink during later stages of embryonic development.[24, 53, 86] Notably, severe eye abnormalities and head edema were observed, starting at relatively low concentrations (≥ 0.02 pM) and the number of deformed zebrafish with eye abnormalities increases as NP concentration increases. Such eye abnormalities were rarely observed for embryos that were exposed to smaller Ag NPs even at high concentrations or toxic heavy ions (e.g., Cd^{2+}).

Strikingly, individual zebrafish with one type of severe deformations (e.g., cardiac, eye or head) was typically accompanied with several other types of deformations (e.g., finfold, tail and yolk sac edema) (Figure 47Ad). Such interesting findings suggest that embryonic developmental pathways are highly

orchestra and one pathway likely highly depend upon others, which lead to multiple deformations in single zebrafish.

By comparing the results of this study with those of our previous study of effects of smaller Ag NPs (11.6±3.5 nm in diameter) on embryonic development,[11] we found that toxic effects of NPs highly depend upon their sizes. Larger number of embryos developed to severe deformed zebrafish and became dead as they were exposed to larger Ag NPs even at very low concentrations (95.4±19.0 nm; ≥ 0.020 pM). In contrast, the embryos developed to normal zebrafish, but not deformed zebrafish or became dead, as they were exposed to small NPs even at higher concentrations (≤ 80 pM; 11.6±3.5 nm).[11] Taken together, the results show that the large NPs cause much higher toxic effects on embryonic development than small NPs, and embryos can serve as effective *in vivo* assays to screen biocompatibility and toxicity of NPs.

Quantitative Imaging and Analysis of Single Ag NPs Embedded in Zebrafish

To address why some embryos developed normally while others became deformed or dead, we further determined distributions of NPs in developed zebrafish, which had been incubated with 90s-nm Ag NPs (≤ 2 pM) chronically for 120 h, since they were cleavage-stage embryos. Individual NPs embedded in various tissues of normal and deformed zebrafish were characterized using DFOMS. The ultrathin sections (1-2 μm thickness) of tissue samples were prepared as described in Methods. The results in Figure 48 show that NPs were embedded in both normally developed and deformed zebrafish and NPs were well distributed in eyes, hearts and brains of zebrafish, which indicates that NPs diffused into embryos and stayed inside the embryos throughout their developmental stages.

The number and sizes of individual Ag NPs embedded in tissues were characterized using their distinctive plasmonic optical properties (colors), or size-

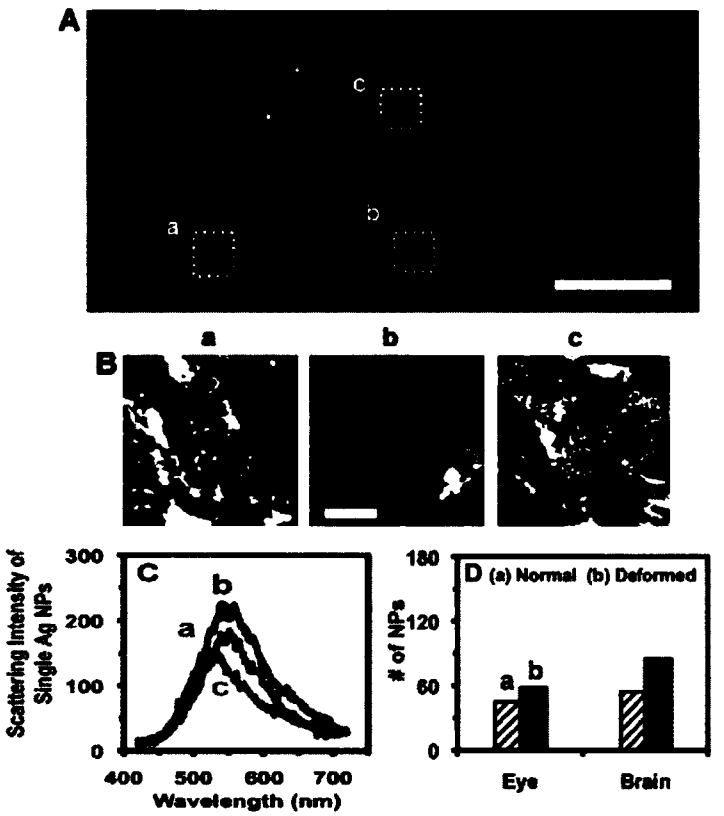

Figure 48. Quantitative imaging of individual Ag NPs embedded in deformed zebrafish using DFOMS.

(A) Optical image of longitudinal section of the fixed zebrafish with five types of deformations show areas of: (a) eye, (b) cardiac and (c) brain tissues, as squared in (a-c). (B) Zoom-in optical images of those tissue sections squared in (A). Individual Ag NPs embedded in the tissue sections are circled. (C) LSPR spectra of those single Ag NPs circled in (B) show distinctive λ_{max} (FWHM) of: (a) 556 (97), (b) 558 (101), and (c) 549 (104) nm. (D) Histograms of distributions of the number of Ag NPs embedded in retina (eye) and brain of (a) normally developed zebrafish and (b) deformed zebrafish show higher number of embedded NPs in deformed NPs. The scale bars are 500 μm in (A) and 50 μm in (B).

dependent LSPR spectras (Figures 48C). More NPs embedded in eye and brain tissues were found in deformed zebrafish than normal zebrafish (Figure 48D), suggesting dose-dependent toxic effects of NPs on embryonic development. The larger number of NPs accumulated inside the embryos throughout their development may lead to their deformation and dead. Nonetheless, individual embryos could have various degrees of tolerance to toxic effects of Ag NPs. Embryos with high degree of tolerance could survive and develop to normal zebrafish, while those with low degree of tolerance could develop to deformed zebrafish or become dead. Therefore, this study underscores the importance of study of effects of NPs on embryonic development at single NP and single embryo resolution.

SUMMARY

In summary, we have synthesized, purified and characterized Ag NPs (95.4±19.0 nm) that are stable (non-aggregated) in egg-water (medium of embryos; 1.5 mM NaCl) over the cause of entire embryonic development (120 h). The results show individual NPs passively diffused into embryos through chorionic pores, and stayed inside the embryos throughout entire embryonic development, demonstrating their ability of concentrating potential release of NPs into aquatic systems. NPs were observed in normal and deformed zebrafish that had been incubated with NPs for 120 h since they were cleavage-stage embryos. We found dose-dependent toxic effects of NPs on the embryonic development, and higher doses of NPs led to higher levels of toxic effects on embryonic development. As NP concentrations increase, the number of embryos that developed to normal zebrafish decreases, while the number of embryos that became dead and developed to deformed zebrafish increases. In comparison with our previous studies of effects of smaller Ag NPs (11.6 ± 3.5 nm in diameter) on embryonic development, we found size-dependent toxic effects of NPs on embryonic development and larger NPs are more toxic than smaller NPs. Taken together, our studies show that zebrafish embryos can serve as ultrasensitive *in vivo* assays to rapidly screen biocompatibility and toxicity of NPs and to

effectively monitor the transport and effects of potential release of nanomaterials into eco-systems.

METHODS

Synthesis and Characterization of 90s-nm Ag NPs

We synthesized Ag NPs (95.4±19.0 nm in diameter) by rapidly adding sodium citrate (20 mL, 34 mM in DI water) into $AgNO_3$ (500 mL, 1.06 mM in DI water) under stirring and refluxing. The mixture was continuously refluxed and stirred for 95 min, while the colors of the mixture turned from colorless to straw yellow, then opaque yellow, and finally muddy yellow. We then turned off the heating mantle and continued refluxing and stirring the solution until it was cooled to room temperature. The NP solution was immediately filtered using 0.22-μm filters and washed three times as described previously. The NP solution was characterized for size and stability as described in previous chapters. The concentrations of colloidal NP solutions were calculated using the approaches as we described previously.

Breeding of Zebrafish Embryos

Wild-type adult zebrafish (Aquatic Ecosystems) were maintained and bred as described previously.

Real-time Imaging of Diffusion of Single Ag NPs into/in Embryos

The cleavage-stage embryos in self-made microchambers containing egg-water with purified and stable 90 nm Ag NPs (1 pM) were imaged in real-time to track the diffusion of single NPs into embryos and inside embryos as we described previously.

Quantitative Study of Dose-Dependent Toxicity of Ag NPs

The cleavage-stage embryos were incubated with various concentrations of 90 nm NPs (0, $2x10^{-4}$, $2x10^{-3}$, 1.0, and 2.0 pM) or (0, $5.7x10^{-4}$, $5.7x10^{-3}$, 2.8, 5.7 μg/mL) and supernatants as described in previous chapters. Zebrafish observations were done as described previously.

Quantitative Imaging of Single Ag NPs Embedded in Individual Zebrafish

The number and sizes of individual NPs embedded in the tissues of interest were quantitatively determined using their size-dependent LSPR spectra acquired by DFOMS and as described in previous chapters (Figure 48).

Data Analysis and Statistics

For study of sizes, shapes, LSPR spectra, and stability of single NPs, 300 individual NPs were studied for each sample with a minimum of 100 NPs for each measurement. For real-time imaging of transport and diffusion mechanisms of single NPs into and in embryos over time, a minimum of 15 embryos were studied for each given concentration with 5 embryos per measurement. For study of dose-dependent effects of NPs on embryonic development, a total number of 36 embryos were studied for each NP concentration and each control experiment with a minimum of 12 embryos studied per measurement.

CHAPTER VII

CONCLUSION

In conclusion, as described in Chapter II, we utilized zebrafish embryos as our living *in vivo* model system to assess the transport, biocompatibility, and toxicity of our purified and biologically clean Ag NPs. By statistically comparing the distributions of normal, deformed and dead embryos, it was observed that the Ag NPs caused deformities and death in a concentration dependent manner. The NPs were stable in the egg-water media and were found to transport into the embryos by random diffusion. It was observed that the diffusion rates of the Ag NPs varied dependent upon the area of the embryo in which they were contained. These results taken together implied that the NPs caused dose specific deformity depending on the concentration of the nanoparticles and it was determined that at a low dose the nanoparticles were biocompatible within the embryonic system, causing no deformities.

In Chapter III, we utilized our *in vivo* model system used in chapter I, and the same purified NPs to probe the stage dependent transport kinetics, biocompatibility and toxicity effects of nanoparticles on embryos at different time periods of development. The NPs were determined to enter and transport into the embryos by random diffusion independent of the time of development. It was observed that the Ag NPs caused deformities dependent on the concentration of the nanoparticles, as well as the time period during development that the nanoparticles were administered. These results taken together implied that the NPs cause stage specific deformities depending on the time of development that the nanoparticles were in contact with the embryo.

Apart from bare Ag NPs, in Chapter IV, Ag NPs, which were surface conjugated with different peptides to yield different surface charges were also used to probe the nanoenvironments within our *in vivo* model system in real time. Using our state of the art DFOMS, we were able to observe Ag NPs inside the embryo regardless of the surface charge of the NP. It was observed that the

different surface charged Ag NPs caused deformities dependent not only on the concentration of the nanoparticles, but dependent on the charge of the nanoparticles. These results indicated that as the surface charge of the NP became more positive; the NPs became more biocompatible, or less toxic, causing fewer deformities.

Drug delivery vehicles will have molecules conjugated on the NP's surface and it contributes to its charge on the surface, it was of interest to study the surface charge of the NPs and how it would affect the transport and biocompatibility of NPs in a living *in vivo* model system. These are important considerations to be taken into account when designing drug delivery vehicles, because they have to be able to transport in a living system to get where they need to go to deliver a drug. This study is a significant step forward in that direction by studying the transport kinetics inside a living system.

In the chapters II, III and IV, the stability of purified NPs in egg-water media was comprehensively established before demonstrating the application of Ag NPs as optical probes in our *in vivo* model system. In Chapter V we were also able to establish the stability of our larger sized purified Ag NPs (42 nm) in egg-water media to utilize them in our *in vivo* model system to assay the transport, biocompatibility and toxicity of larger sized nanoparticles on embryonic development. We observed that the 42 nm Ag NPs were able to transport inside the embryo by random diffusion and that the larger nanoparticles caused deformities dependent on the concentration of the nanoparticles. This was similar to findings in chapter II, however it was found that the larger sized NPs were much more toxic and less biocompatible at the same concentrations of the 12 nm Ag NPs. These results taken together imply that smaller sized NPs are much more biocompatible as compared to larger sized 42 nm Ag NPs.

Apart from using the 42 nm Ag NPs, we also wanted to use a larger sized Ag NP (95 nm) and explore their possible toxicity in our *in vivo* assay. In Chapter VI we established the stability of our 95 nm purified Ag NPs in egg-water media

and then used them to assay the transport, biocompatibility and toxicity on embryonic development. We observed 95 nm Ag NPs inside the embryo and were able to follow their transport into the embryonic mass despite their large size and from this it was determined that the Ag NPs were able to transport inside the embryo by random diffusion independent of the size. Deformities in embryonic development were observed in a concentration dependent manner, similar to findings in chapter II and V, however it was found that the 95 nm Ag NPs were much more toxic and less biocompatible at even very low concentrations in the pM range. These results taken together implied that the smaller sized NPs, 12 nm – 42 nm, were much more biocompatible as compared to the largest sized 95 nm Ag NPs.

The results of the research mentioned in this dissertation have demonstrated that zebrafish embryos are a powerful *in vivo* model system to use to assay the transport, biocompatibility, and toxicity of different types of nanomaterials. This opens up the possibility of using this system as a standard assay to screen many different types of multi-functional NPs, including target-specific nanomaterials. There is the possibility of using NPs as effective drug delivery vehicles by attaching desired drug molecules to the surface of NPs, so it is very important to collect preliminary data on how a NP will transport in a living system and if it will be toxic to living cells. To conclude, the chapters included in this dissertation have shown conclusively the versatile nature of using zebrafish embryos as an *in vivo* assay to screen different types of NPs by demonstrating their use as a living embryonic model system to screen different types of Ag NPs.

REFERENCES

1. Tiwari, S. B.; Amiji, M. M., A review of nanocarrier-based CNS delivery systems. *Curr. Drug Deliv.* **2006,** *3*, 219-232.

2. Xu, X. H. N.; Patel, R. P., Nanoparticles for live cell dynamics. In *Encyclopedia of Nanoscience and Nanotechnology*, Nalwa, H. S., Ed. American Scientific Publishers: 2004; Vol. 7, pp 189-192.

3. Xu, X. H. N.; Patel, R. P., Imaging and Assembly of Nanoparticles in Biological Systems. In *Handbook of Nanostructured Biomaterials and Their Applications in Nanobiotechnology*, Nalwa, H. S., Ed. American Scientific Publishers: 2005; Vol. 1, pp 435-456.

4. Xu, X. H. N.; Song, Y.; Nallathamby, P. D., Probing membrane transport of single live cells using single molecule detection and single nanoparticle assay. In *New Frontiers in Ultrasensitive Bioanalysis: Advanced Analytical Chemistry Applications in Nanobiotechnology, Single Molecule Detection, and Single Cell Analysis*, Xu, X. H. N., Ed. Wiley: New Jersey, 2007; pp 41-65.

5. Yamada, T.; Iwasaki, Y.; Tada, H.; Iwabuki, H.; Chuak, M. K. I.; VandenDriessche, T.; Fukuda, H.; Kondo, A.; Ueda, M.; Seno, M.; Tanizawa, K.; Kuroda, S., Nanoparticles for the delivery of genes and drugs to human hepatocytes. *Nature Biotechnology* **2003,** *21*, 885-890.

6. Nel, A.; Xia, T.; Madler, L.; Li, N., Toxic potential of materials at the nanolevel. *Science* **2006,** *311*, 622-627.

7. West, J. L.; Halas, N. J., Engineered nanomaterials for biophotonics applications: improving sensing, imaging, and therapeutics. *Annu Rev Biomed Eng* **2003,** *5*, 285-292.

8. Willets, K. A.; Van Duyne, R. P., Localized surface plasmon resonance spectroscopy and sensing. *Annu Rev Phys Chem* **2007,** *58*, 267-297.

9. Xu, X.-H. N.; Patel, R. P., Nanoparticles For Live Cell Dynamics. In *Encyclopedia of Nanoscience and Nanotechnology*, Nalwa, H. S., Ed. American Scientific Publishers: 2004; Vol. 7, pp 189-192.

10. Lippincott-Schwartz, J.; Snapp, E.; Kenworthy, A., Studying protein dynamics in living cells. *Nat Rev Mol Cell Biol* **2001,** *2*, 444-456.

11. Lee, K. J.; Nallathamby, P. D.; Browning, L. M.; Osgood, C. J.; Xu, X.-H. N., *In Vivo* Imaging of Transport and Biocompatibility of Single Silver Nanoparticles in Early Development of Zebrafish Embryos. *ACS Nano* **2007,** *1*, 133-143.

12. Lee, K. J.; Browning, L. M.; Huang, T.; Ding, F.; Nallathamby, P. D.; Xu, X. H., Probing of multidrug ABC membrane transporters of single living cells using single plasmonic nanoparticle optical probes. *Anal Bioanal Chem* **2010,** *397*, 3317-3328.

13. Nallathamby, P. D.; Lee, K. J.; Xu, X.-H. N., Design Of Stable And Uniform Single Nanoparticle Photonics For In Vivo Dynamics Imaging Of Nanoenvironments Of Zebrafish Embryonic Fluids. *ACS Nano* **2008,** *2*, 1371-1380.

14. Nallathamby, P. D.; Lee, K. J.; Desai, T.; Xu, X. H., Study of the multidrug membrane transporter of single living Pseudomonas aeruginosa cells using size-dependent plasmonic nanoparticle optical probes. *Biochemistry* **2010,** *49*, 5942-5953.

15. Huang, T.; Nallathamby, P. D.; Xu, X.-H. N., Photostable Single-Molecule Nanoparticle Optical Biosensors For Real-Time Sensing Of Single Cytokine Molecules And Their Binding Reactions. *J. Am. Chem. Soc.* **2008,** *130*, 17095-17105.

16. den Hertog, J., Chemical Genetics: Drug Screens In Zebrafish. *Biosci. Rep.* **2005,** *25*, 289-297.

17. Hill, A. J.; Teraoka, H.; Heideman, W.; Peterson, R. E., Zebrafish as a model vertebrate for investigating chemical toxicity. *Toxicol. Sci.* **2005,** *86*, 6-19.

18. Kahn, P., Zebrafish Hit The Big Time. *Science* **1994,** *264*, 904-905.

19. Teraoka, H.; Dong, W.; Hiraga, T., Zebrafish As A Novel Experimental Model For Developmental Toxicology. *Congenit. Anom. (Kyoto)* **2003,** *43*, 123-132.

20. Zon, L. I.; Peterson, R. T., In vivo drug discovery in the zebrafish. *Nat. Rev. Drug Discov.* **2005,** *4*, 35-44.

21. Rieger, S.; Kulkarni, R. P.; Darcy, D.; Fraser, S. E.; Koster, R. W., Quantum dots are powerful multipurpose vital labeling agents in zebrafish embryos. *Dev. Dyn.* **2005,** *234*, 670-681.

22. Luckenbill-edds, L., Introduction: Research News in Developmental Biology in 1895 and 1995. *Amer. Zool.* **1997,** *37*, 213-219.

23. Strehlow, D.; Heinrich, G.; Gilbert, W., The fates of the blastomeres of the 16-cell zebrafish embryo. *Development 120, 1791-1798* **1994,** *120*, 1791-1798

24. Hoar, W. S.; Randall, D. J., *Fish Physiology: The Physiology of Developing Fish, Part A, Eggs and Larvae*. Academic Press: New York, 1988; p 1-48.

25. Rawson, D. M.; Zhang, T.; Kalicharan, D.; Jongebloed, W. L., Field Emission Scanning Electron Microscopy And Transmission Electron Microscopy Studies Of The Chorion, Plasma Membrane And Syncytial

Layers Of The Gastrula Stage Embryo Of The Zebrafish Brachydanio Rerio: A Consideration Of The Structural And Functional Relationships With Respect To Cryoprotectant Penetration. *Aquaculture Research* **2000,** *31*, 325-336.

26. Kusumi, A.; Sako, Y., Compartmental Structure Of The Plasma Membrane For Receptor Movements As Revealed By A Nanometer-Level Motion Analysis. *J. Cell Biology* **1994,** *125*, 1251-1264.

27. Kusumi, A.; Sako, Y.; Yamamoto, M., Confined Lateral Diffusion Of Membrane Receptors As Studied By Single Particle Tracking (Nanovid Microscopy). Effects Of Calcium-Induced Differentiation In Cultured Epithelial Cells. *Biophys. J.* **1993,** *65*, 2021-2040.

28. Tinoco, I.; Sauer, K.; Wang, J.; Puglisi, J. D., Molecular Motion and Transport Properties. In *Physical Chemistry-Principles and Applications in Biological Sciences*, Prentice Hall: 2002; pp 274-290.

29. Xu, X.-H. N.; Jeffers, R. B.; Gao, J.; Logan, B., Novel Solution-Phase Immunoassays For Molecular Analysis Of Tumor Markers. *Analyst* **2001,** *126*, 1285-1292.

30. Bohren, C. F.; Huffman, D. R., *Absorption and Scattering of Light by Small Particles.* Wiley: New York, 1983; p 287-380.

31. Kreibig, U.; Vollme, M., *Optical Properties of Metal Clusters.* Springer: Berlin, 1995; p 14-123.

32. Mie, G., Beiträg Zur Optik Trüber Medien, Speziell Kolloidaler Metrallősungen. *Ann. Phys.* **1908,** *25*, 377-445.

33. Mulvaney, P., Surface Plasmon Spectroscopy Of Nanosized Metal Particles. *Langmuir* **1996,** *12*, 788-800.

34. Hallare, A. V.; Schirlinga, M.; Luckenbacha, T.; Ko¨ hler, H.-R.; Triebskorn, R., Combined effects of temperature and cadmium on developmental parameters and biomarker responses in zebrafish (Danio rerio) embryos. *J. Thermal Biology* **2005,** *30*, 7-17.

35. Williams, F. E.; Sickelbaugh, T. J.; Hassoun, E., Modulation by ellagic acid of DCA-induced developmental toxicity in the zebrafish (Danio rerio). *J. Biochem. Mol. Toxicol.* **2006,** *20*, 183-190.

36. Antkiewicz, D. S.; Burns, C. G.; Carney, S. A.; Peterson, R. E.; Heideman, W., Heart Malformation is an Early Response to TCDD In Embryonic Zebrafish. *Toxicol. Sci.* **2005,** *84*, 368-377.

37. Arenzana, F. J.; Carvan, M. J., 3rd; Aijon, J.; Sanchez-Gonzalez, R.; Arevalo, R.; Porteros, A., Teratogenic Effects of Ethanol Exposure on Zebrafish Visual System Development. *Neurotoxicol. Teratol.* **2006,** *28*, 342-348.

38. Jean, D.; Ewan, K.; Gruss, P., Molecular regulators involved in vertebrate eye development. *Mech Dev* **1998,** *76*, 3-18.

39. Lee, P. C.; Meisel, D., Adsorption and surface-enhanced Raman of dyes on silver and gold sols. *J. Phys. Chem.* **1982,** *86*, 3391-3395.

40. Xu, X. H. N.; Brownlow, W. J.; Kyriacou, S. V.; Wan, Q.; Viola, J. J., Real-time probing of membrane transport in living microbial cells using single nanoparticle optics and living cell imaging. *Biochemistry* **2004,** *43*, 10400-10413.

41. Kyriacou, S.; Brownlow, W.; Xu, X.-H. N., Nanoparticle optics for direct observation of functions of antimicrobial agents in single live bacterial cells. *Biochemistry* **2004,** *43*, 140-147.

42. Xu, X. H. N.; Chen, J.; Jeffers, R. B.; Kyriacou, S. V., Direct measurement of sizes and dynamics of single living membrane transporters using nano-optics. *Nano Lett.* **2002,** *2*, 175-182.

43. Kyriacou, S. V.; Nowak, M. E.; Brownlow, W. J.; Xu, X. H. N., Single live cell imaging for real-time monitoring of resistance mechanism in *Pseudomonas aeruginosa*. *J. Biomed. Opt.* **2002,** *7*, 576-586.

44. Xu, X. H. N.; Brownlow, W. J.; Huang, S.; Chen, J., Real-time measurements of single membrane pump efficiency of single living Pseudomonas aeruginosa cells using fluorescence microscopy and spectroscopy. *Biochem. Biophys. Res. Commun.* **2003,** *305*, 79-86.

45. Westerfield, M., *The zebrafish book: A Guide for the Laboratory Use of Zebrafish (Danio Rerio*)* University of Oregon Press Eugene, OR, Chapters 1-4, 1993; (http://zfin.org/zf_info/zfbook/zfbk.html).

46. Xu, X.-H. N.; Huang, S.; Brownlow, W.; Salatia, K.; Jeffers, R., Size and temperature dependence of surface plasmon absorption of gold nanoparticles induced by Tris(2,2'-bipyridine)ruthenium(II). *J. Phys. Chem. B.* **2004,** *108*, 15543-15551

47. Mohideen, M.-A. P. K.; Beckwith, L. G.; Tsao-Wu, G. S.; Moore, J. L.; Wong, A. C. C.; Chinoy, M. R.; Cheng, K. C., Histology-Based Screen for Zebrafish Mutants with Abnormal Cell Differentiation. *Developmental Dynamics* **2003,** *228*, 414–423.

48. Tiwari, S. B.; Amiji, M. M., A review of nanocarrier-based CNS delivery systems. *Curr. Drug Delivery* **2006,** *3*, 219-32.

49. Xu, X.-H. N.; Song, Y.; Nallathamby, P. D., Probing Membrane Transport Of Single Live Cells Using Single Molecule Detection And Single Nanoparticle Assay. In *New Frontiers in Ultrasensitive Bioanalysis: Advanced Analytical Chemistry Applications in Nanobiotechnology, Single*

Molecule Detection, and Single Cell Analysis, Xu, X.-H. N., Ed. Wiley: New Jersey, 2007; pp 41-65.

50. Yamada, T.; Iwasaki, Y.; Tada, H.; Iwabuki, H.; Chuah, M. K.; VandenDriessche, T.; Fukuda, H.; Kondo, A.; Ueda, M.; Seno, M.; Tanizawa, K.; Kuroda, S., Nanoparticles for the delivery of genes and drugs to human hepatocytes. *Nature biotechnology* **2003,** *21*, 885-890.

51. Hill, A. J.; Teraoka, H.; Heideman, W.; Peterson, R. E., Zebrafish As A Model Vertebrate For Investigating Chemical Toxicity. *Toxicol. Sci.* **2005,** *86*, 6-19.

52. Pichler, F. B.; Laurenson, S.; Williams, L. C.; Dodd, A.; Copp, B. R.; Love, D. R., Chemical discovery and global gene expression analysis in zebrafish. *Nat Biotechnol* **2003,** *21*, 879-883.

53. Kunz, Y. W., *Developmental Biology of Teleost Fishes*. Springer: Netherlands, 2004; p 267-428.

54. Helde, K. A.; Wilson, E. T.; Cretekos, C. J.; Grunwald, D. J., Contribution of early cells to the fate map of the zebrafish gastrula. *Science* **1994,** *265*, 517-520.

55. Stickney, H. L.; Barresi, M. J. F.; Devoto, S. H., Somite development in zebrafish. *Developmental Dynamics* **2000,** *219*, 287–303.

56. Mathavan, S.; Lee, S. G.; Mak, A.; Miller, L. D.; Murthy, K. R.; Govindarajan, K. R.; Tong, Y.; Wu, Y. L.; Lam, S. H.; Yang, H.; Ruan, Y.; Korzh, V.; Gong, Z.; Liu, E. T.; Lufkin, T., Transcriptome analysis of zebrafish embryogenesis using microarrays. *PLoS Genet* **2005,** *1*, 260-76.

57. Choe, S.; Bennett, M. J.; Fujii, G.; Curmi, P. M.; Kantardjieff, K. A.; Collier, R. J.; Eisenberg, D., The Crystal Structure of Diphtheria Toxin. *Nature* **1992,** *357*, 216-222.

58. Huang, T.; Nallathamby, P. D.; Gillet, D.; Xu, X.-H. N., Design and Synthesis of Single-Nanoparticle Optical Biosensors for Imaging and Characterization of Single Receptor Molecules on Single Living Cells. *Anal. Chem.* **2007,** *79*, 7708-7718.

59. Browning, L. M.; Lee, K. J.; Huang, T.; Nallathamby, P. D.; Lowman, J. E.; Xu, X. H., Random walk of single gold nanoparticles in zebrafish embryos leading to stochastic toxic effects on embryonic developments. *Nanoscale* **2009,** *1*, 138-52.

60. Xu, X. H. N.; Wan, Q.; Kyriacou, S. V.; Brownlow, W. J.; Nowak, M. E., Direct Observation Of Substrate Induction Of Resistance Mechanism In *Pseudomonas Aeruginosa* Using Single Live Cell Imaging. *Biochemical and biophysical research communications* **2003,** *305*, 941-949.

61. Kyriacou, S.; Nowak, M.; Brownlow, W.; Xu, X., Single Live Cell Imaging for Real-Time Monitoring of Resistance Mechanism in Pseudomonas aeruginosa. *J. Biomedical Optics* **2002,** *7*, 576-586.

62. Xu, X.-H. N.; Brownlow, W.; Huang, S.; Chen, J., Real-time Measurements of Single Membrane Pump Efficiency of Single Living Pseudomonas aeruginosa Cells Using Fluorescence Microscopy and Spectroscopy. *Biochem. Biophys. Res. Commun.* **2003,** *305*, 79-86.

63. Xu, X.-H. N.; Brownlow, W. J.; Kyriacou, S. V.; Wan, Q.; Viola, J. J., Real-Time Probing of Membrane Transport in Living Microbial Cells Using Single Nanoparticle Optics and Living Cell Imaging. *Biochemistry* **2004,** *43*, 10400-10413.

64. Xu, X.-H. N.; Chen, J.; Jeffers, R. B.; Kyriacou, S., Direct Measurement of Sizes and Dynamics of Single Living Membrane Transporters Using Nanooptics. *Nano Lett.* **2002,** *2*, 175-182.

65. Nie, A. A. C. Z. T. B. R. A. T. S., Counting Single Native Biomolecules and Intact Viruses with Color-Coded Nanoparticles. *Analytical Chemistry* **2006,** *78*, 1061-1070.

66. Bruchez, M., Jr.; Moronne, M.; Gin, P.; Weiss, S.; Alivisatos, A. P., Semiconductor Nanocrystals as Fluorescent Biological Labels. *Science* **1998,** *281*, 2013-2016.

67. Chan, W. C.; Nie, S., Quantum Dot Bioconjugates for Ultrasensitive Nonisotopic Detection. *Science* **1998,** *281*, 2016-2018.

68. Xu, S. V. K. M. E. N. W. J. B. X.-H. N., Single live cell imaging for real-time monitoring of resistance mechanism in *Pseudomonas aeruginosa*. *Journal of Biomedical Optics* **2002,** *7*, 576-586.

69. Yeung, X.-H. X. E. S., and Photodecomposition in Free Solution Direct Measurement of Single-Molecule Diffusion. *Science* **1997,** *275*, 1106-1109.

70. LaVan, D. A.; McGuire, T.; Langer, R., Small-scale systems for in vivo drug delivery. *Nat. Biotechnol.* **2003,** *21*, 1184-91.

71. Ferrari, M., Cancer nanotechnology: opportunities and challenges. *Nat. Rev. Cancer* **2005,** *5*, 161-71.

72. Nel, A. E.; Madler, L.; Velegol, D.; Xia, T.; Hoek, E. M.; Somasundaran, P.; Klaessig, F.; Castranova, V.; Thompson, M., Understanding biophysicochemical interactions at the nano-bio interface. *Nat. Mater.* **2009,** *8*, 543-57.

73. Sandip B. Tiwari, M. M. A., A review of nanocarrier based CNS Delivery systems. *Current Drug Delivery* **2006,** *3*, 219-232.

74. Yugang Sun, Y. X., Gold and silver nanoparticles: A class of chromophores with colors tunable in the range from 400 to 750 nm. *Analyst* **2003,** *128*, 686–691.

75. Yu Pan, S. N., Annika Leifert, Monika Fischler, Fei Wen,Ulrich Simon,Gunter Schmid, Wolfgang Brandau, Willi Jahnen-Dechent, Size-Dependent Cytotoxicity of Gold Nanoparticles. *Small* **2007,** *11*, 1941 – 1949.

76. Lajos Balogh, S. S. N., Bindu M. Nair,Wojciech Lesniak, Chunxin Zhang, Lok Yun Sung, Muhammed S.T. Kariapper, Areej El-Jawahri, Mikel Llanes,Brian Bolton, Fatema Mamou, Wei Tan, MA,Alan Hutson, Leah Minc, Mohamed K. Khan, Significant effect of size on the in vivo biodistribution of gold composite nanodevices in mouse tumor models. *Nanomedicine: Nanotechnology, Biology, and Medicine* **2007,** *3*, 281–296.

77. Kohane, D. S., Microparticles and Nanoparticles for Drug Delivery. *Biotechnology and Bioengineering* **2007,** *96* (203-209).

78. Andre Nel, T. X., Lutz Ma¨dler, Ning Li, Toxic Potential of Materials at the Nanolevel. *Science* **2006,** *311*, 622-627.

79. Jinping Cheng, E. F., Shuk Han Cheng, Effect of Carbon nanotube on Developing Zebrafish(Danio Rerio) Embryo. *Environ. Toxicol. Chem.* **2007,** *26*, 708-716.

80. Lee, K. J., et. al., In Vivo Imaging of Transport and Biocompatibility of Single Silver Nanoparticles in Early Development of Zebrafish Embryos. *ACS Nano* **2007,** *1*, 133-143.

81. Adrian J. Hill, H. T., Warren Heideman,Richard E. Peterson, Zebrafish as a Model Vertebrate for Investigating Chemical Toxicity. *Toxicological Sciences* **2005,** *86* (1), 6–19.

82. Elwood Linney, L. U., Susan Donerly, Zebrafish as a neurotoxicological model. *Neurotoxicology and Teratology* **2004,** *26*, 709–718.

83. Langheinrich, U., Zebrafish: a new model on the pharmaceutical catwalk. *BioEssays* **2003,** *25*, 904–912.

84. Ellen E. Connor, J. M., Anand Gole, Catherine J. Murphy, Michael D. Wyatt, Gold Nanoparticles Are Taken Up by Human Cells but Do Not Cause Acute Cytotoxicity. *Small* **2005,** *1*, 325 –327.

85. Katsuyuki Tanizawa.; Shunichi Kuroda, S., Nanoparticle for the delivery of genes and drugs to human hepatocytes. *Nature Biotechnology* **2003,** *21*, 885-890.

86. Gong, Z.; Korzh, V., *Fish Development and Genetics: The Zebrafish and Medaka Models*. World Scientific Publishing Co.: Singapore, 2004; Vol. 2, p 87-424.

87. Panyam, J.; Dali, M. M.; Sahoo, S. K.; Ma, W.; Chakravarthi, S. S.; Amidon, G. L.; Levy, R. J.; Labhasetwar, V., Polymer degradation and in vitro release of a model protein from poly(D,L-lactide-co-glycolide) nano- and microparticles. *J. Control Release* **2003,** *92*, 173-187.

88. Dunne, M.; Corrigan, I.; Ramtoola, Z., Influence of particle size and dissolution conditions on the degradation properties of polylactide-co-glycolide particles. *Biomaterials* **2000,** *21*, 1659-1668.

89. Lamprecht, A.; Schafer, U.; Lehr, C. M., Size-dependent bioadhesion of micro- and nanoparticulate carriers to the inflamed colonic mucosa. *Pharm. Res.* **2001,** *18*, 788-793.

90. Rejman, J.; Oberle, V.; Zuhorn, I. S.; Hoekstra, D., Size-dependent internalization of particles via the pathways of clathrin- and caveolae-mediated endocytosis. *Biochem. J.* **2004,** *377*, 159-169.

91. Kohane, D. S.; Tse, J. Y.; Yeo, Y.; Padera, R.; Shubina, M.; Langer, R., Biodegradable polymeric microspheres and nanospheres for drug delivery in the peritoneum. *J. Biomed. Mater. Res. A.* **2006,** *77*, 351-361.

92. Kagan, V. E.; Bayir, H.; Shvedova, A. A., Nanomedicine and nanotoxicology: two sides of the same coin. *Nanomedicine* **2005,** *1*, 313-316.

93. Tilgner, K.; Wojciechowicz, K.; Jahoda, C.; Hutchison, C.; Markiewicz, E., Dynamic complexes of A-type lamins and emerin influence adipogenic capacity of the cell via nucleocytoplasmic distribution of beta-catenin. *J. Cell. Sci.* **2009,** *122*, 401-413.

94. Chow, E. S.; Hui, M. N.; Lin, C. C.; Cheng, S. H., Cadmium inhibits neurogenesis in zebrafish embryonic brain development. *Aquat. Toxicol.* **2008,** *87*, 157-169.

95. Hen Chow, E. S.; Cheng, S. H., Cadmium affects muscle type development and axon growth in zebrafish embryonic somitogenesis. *Toxicol. Sci.* **2003,** *73*, 149-159.

96. Chan, P. K.; Cheng, S. H., Cadmium-induced ectopic apoptosis in zebrafish embryos. *Arch. Toxicol.* **2003,** *77*, 69-79.

97. Viola, J., et. al., Real-Time Probing of Membrane Transport in Living Microbial Cells Using Single Nanoparticle Optics and Living Cell Imaging. *Biochemistry* **2004,** *43*, 10400-10413.

98. Ahamed, M.; Alsalhi, M. S.; Siddiqui, M. K., Silver nanoparticle applications and human health. *Clin. Chim. Acta.* **2010,** *411*, 1841-1848.

99. Misra, R.; Acharya, S.; Sahoo, S. K., Cancer nanotechnology: application of nanotechnology in cancer therapy. *Drug Discov. Today* **2010,** *15*, 842-850.

100. Teli, M. K.; Mutalik, S.; Rajanikant, G. K., Nanotechnology and nanomedicine: going small means aiming big. *Curr. Pharm. Des.* **2010,** *16*, 1882-1892.

101. Xu, X.-H. N.; Patel, R. P., Imaging and Assembly of Nanoparticles in Biological Systems. In *Handbook of Nanostructured Biomaterials and Their Applications in Nanobiotechnology*, Nalwa, H. S., Ed. American Scientific Publishers: Los Angeles, CA, 2005; Vol. 1, pp 435-456.

APPENDIX A

GUIDELINES FOR HANDLING NANOMATERIALS

Zebrafish Experiments

All experiments involving live zebrafish and/or zebrafish embryos and nanoparticles were carried out in compliance with the guidelines set in IACUC protocol #: 11-030 entitled "NIRT: Design of Biocompatible Nanoparticles for Probing Living Cellular Functions and Their Potential Environmental Impacts" and was approved April of 2012.

Handling Nanoparticles

According to NIOSH, the following workplace tasks may increase the risk of exposure to nanoparticles:

1. Working with nanoparticles in liquid media without the necessary protection (e.g., gloves, safety goggles) will increase the risk of skin or eye exposure.
2. Working with nanoparticles in liquid media during pouring or mixing procedures, or where high risk of agitation is involved, will lead to an increased likelihood of inhalation of droplets, which may be formed.
3. Generating nanoparticles in the gas phase in non-enclosed systems will increase the chances of aerosol release to the workplace.
4. Handling nano-structured powders will lead to the possiblility of aerosolization.

The following guidelines from the University of Oklahoma Health Sciences Center were always followed when working with nanomaterials in the lab (http://www.ouhsc.edu/ibc/documents/NanoparticleGuidelines.doc), although all of these guidelines may not be applicable to the research work associated with this dissertation.

1. Lab coats were worn at all times.
2. Gloves were worn when handling nanoparticles. Because skin exposure was a concern, gloves covered the hand and the wrist.
3. Long arm sleeves were required where high levels of exposure due to splashes of solutions containing nanoparticles were anticipated.
4. Standard lab safety goggles were worn.
5. Whenever possible, work was performed in a chemical hood or biological safety hood.
    a. Aerosol producing activities (such as sonication, vortexing, or centrifuging) were never conducted on an open lab bench.
    b. Activities that were likely to release nanoparticles (such as opening and emptying of tubes) were not performed on an open lab bench.
    c. Solutions containing nanoparticles were handled over disposable lab bench covers.
6. Hand washing facilities were provided in all labs. Hand washing was performed after handling nanoparticles.
7. Lab bench tops and other surfaces had to be cleaned after each lab experiment using a cleaning solution (methanol) suitable for the type of nanoparticles being used.

VITA

Kerry Jean Lee

Dept. of Chemistry and Biochemistry
Alfriend Chemistry Building
Old Dominion University
Norfolk, VA 23529

Education

May, 2012: Ph.D. Biomedical Sciences, Old Dominion University, Norfolk, VA 23529

May, 2005: M.S. Biological Sciences, Old Dominion University, Norfolk, VA 23529

May, 2002: B.S. Biology, Norfolk State University, Norfolk, VA, 23529

Publications

1. F. Ding,* **K. J. Lee**,* Ardeschir Vahedi-Faridi, T. Huang, X. Xu, "Study of Efflux Functions of EGFP Fused ABC Membrane Transporters in *Bacillus Subtilis*", *Anal Bioanal Chem*, **400**, 223-235 (2011). ***Equal first author**
2. **K. J. Lee**, L. M. Browning, T. Huang, F. Ding, P. D. Nallathamby, X. Xu, "Probing of Multidrug ABC Membrane Transporters of Single Living Cells Using Single Plasmonic Nanoparticle Optical Probes ", *Anal Bioanal Chem*, **397**, 3317-3328 (2010).
3. P. D. Nallathamby, **K. J. Lee**, T. Desai, X. Xu, "Real Time Observation of Substrate Size Dependent Efflux Rates in *Pseudomonas aeruginosa* Using Buffer Stable Ag NPs Plasmonic Probes", Biochemistry, **49**, 5942-5953 (2010).
4. L. M. Browning,* **K. J. Lee**,* T. Huang, P. D. Nallathamby, J. E. Lowman, X. Xu, "Random Walk of Single Gold Nanoparticles in Zebrafish Embryos Leading to Uncertain Toxic Effects on Embryonic Developments", *Nanoscale*, **1**, 138-152 (2009). ***Equal first author**
5. P. D. Nallathamby, **K. J. Lee**, X. Xu, "Design of Stable and Uniform Single Nanoparticle Photonics for In Vivo Dynamics Imaging of Nanoenvironments of Zebra fish Embryonic Fluids", *ACS Nano,* **2**, 1371-1380 (2008).